© Copyright 2019

Justin Davis

Characterization of combustion generated particulates produced in an inverted gravity flame reactor

Justin Davis

A dissertation

submitted in partial fulfillment of the

requirements for the degree of

Doctor of Philosophy

University of Washington

2019

Reading Committee:

Igor Novosselov, Chair

John Kramlich

Edmund Seto

Program Authorized to Offer Degree:

Molecular Engineering

University of Washington

Abstract

Characterization of combustion generated particulate matter produced in an inverted gravity flame reactor

Justin Davis

Igor Novosselov:
Research Associate Professor
Mechanical Engineering

Many unknowns remain in the pursuit to describe the formation of combustion generated particles from first principles. Of most importance in the following thesis is the transition from young to mature soot that is evident by the formation of a graphitic shell on the periphery of particles. An inverted gravity flame reactor (IGFR) allows for flexibility in studying the effects of residence time, temperature, and flow properties. Combustion generated particles are characterized to probe the underlying mechanisms involved in the evolution of these particles. Soot particles are characterized using experimental and computational techniques that reveal particle nanostructure and its evolution. The structure is quantified using transmission electron microscopy (TEM) followed by image processing to obtain information on the crystal properties and molecular compounds.

In the third chapter, the repeated exposure of soot in the fuel-rich and the fuel-lean region is explored to find how exposure to complex flow field influences final soot properties. The recirculating flame produces soot with primary particles 2-3 times the size of a non-recirculating flame. Due to the maturity of recirculated particles, computational results, and fringe profiles, we propose a recurring surface growth by the condensation of aromatics on the surface of the particles as the reason for the increased primary particle diameter.

The fourth chapter explores the role temperature and dilution play on particle nanostructure. The prevalence of a shell on the periphery of mature soot particles is confirmed for high-temperature combustion (>1700 K); at low temperatures, the isotropic nature of young soot particles is observed. The young particles contain both shorter fringes and more curved fringes, pointing to the role of curved aromatics in the formation of soot particles.

Finally, several other analysis methods to characterize soot produced in the diluted flames are presented in the fifth chapter. The particles are characterized using UV-Vis absorption, Raman spectroscopy, and ROS activity. These techniques require more analysis, but all show distinct differences between soot produced in the high dilution and low dilution flames.

TABLE OF CONTENTS

List of Figures v

List of Tables xi

Chapter 1. Introduction 1

1.1 Background 1

1.2 Soot formation fundamentals 2

1.3 Health implications 4

1.4 Environmental implications 4

Chapter 2. Experimental methods 6

2.1 Inverted gravity flame reactor 6

2.2 Flame characterization 6

2.3 Transmission electron microscopy 7

2.4 HRTEM image analysis 8

Chapter 3. Soot Morphology and Nanostructure in Complex Flame Flow Patterns via Secondary Particle Surface Growth. 10

3.1 Introduction 11

3.2 Experimental methods 12

3.2.1 Operating conditions to produce recirculating flames 12

3.2.2 HRTEM ROI selection 13

3.2.3 Chemical reactor network development 14

3.3 Results 17
3.3.1 Modeling results 17
3.3.2 TEM analysis 21
3.4 Discussion 25
3.5 Conclusions 30
Chapter 4. Nanostructure Transition of Young Soot Aggregates to Mature Soot Aggregates in Diluted Diffusion Flames 31
4.1 Introduction 32
4.2 Experimental methods 34
4.2.1 Operating conditions to produce diluted flames 34
4.2.2 Maximum soot luminosity region analysis - temperature estimation 37
4.2.3 Measuring the percent of stacked fringes 37
4.2.4 Elemental and organic carbon analysis 40
4.3 Results 40
4.3.1 Flame temperature and soot composition 40
4.3.2 HRTEM- dilution influence on nanostructure 43
4.3.3 Electron beam interactions 51
4.3.4 Optical gap analysis 52
4.4 Soot maturity and shell formation discussion 52
4.5 Conclusions 55
Chapter 5. Alternative analysis of soot generated in diluted flames 58
5.1 Overview 58

5.2 UV-VIS spectroscopy 59
5.2.1 UV-Vis background 59
5.2.2 MeOH extract absorption and total EC/OC 59
5.2.3 UV-Vis spectroscopy 60
5.3 Raman spectroscopy analysis 61
5.3.1 Raman background 61
5.3.2 Experimental techniques 62
5.3.3 Raman deconvolution 62
5.3.4 Raman conclusions 67
5.4 ROS generation of soot produced in Ar diluted ethane and ethylene flames 68
5.4.1 ROS background 68
5.4.2 Experimental methods and reactive oxygen species 68
5.4.3 ROS results 69
5.4.4 ROS conclusions 71
5.5 Soot shell formation 71
Chapter 6. Supplemental information 73
6.1 Methane SEM analysis and recirculation video 73
6.2 Numerical simulations of the recirculating methane flame 73
6.3 Chemical reactor network 79
6.4 Ethylene flame experiments to measure primary particle diameter 79
6.5 Experimental diluted flame pictures 83
6.6 Inconel probe soot collection 83
6.7 HRTEM- threshold parameter 84

6.8 HRTEM images for nanostructure analysis 85

6.9 Electron beam induced structural changes 87

6.10 Image analysis for temperature measurements 89

6.11 Matlab script for image processing 90

Bibliography 101

LIST OF FIGURES

Figure 1.1 Simple soot formation model. Flow moves from top to bottom. 3

Figure 2.1 IGFR schematic used in experimental work to generate soot particles..... 6

Figure 2.2. Soot sample from the zero-dilution methane flame a) before and b) after processing. The processed image is used to obtain quantitative information from HRTEM images. 9

Figure 3.1. Before and after HRTEM images are processed using an in-house Matlab script to extract nanostructure information. a) and b) shows soot from the recirculating flame while c) and d) show soot from the non-recirculating flame. Processed pictures are inverted for publication..... 14

Figure 3.2 Conceptual CRNS for both flames. PSR 1 models a fuel rich region with a high concentration of important growth species for both CRNs. a) IGFR recirculating flame. PSR2R models the flame front. b) IGFR non-recirculating flame. Flow from the wing (PSR2NR) can either diffuse to PSR1NR or travel downstream to the flame tip (PSR3NR). 16

Figure 3.3. CFD pathlines colored by temperature compared to the photographs of the flame: a) recirculating IGFR, b) non-recirculating IGFR. CFD peak temperatures reach 1808 K and 1852 K, respectively. The solid line shows the near stoichiometric condition (X_{O2}=0.01). For location 2, the thermocouple perturbs upward flow leading to a significant error in the temperature measurement. For location 4, the discrepancy in temperature is in part due to the over-prediction in the CFD flame length. Disagreement is also influenced by the probe insertion into the flame. Location 4 relates better with the maximum flame temperature on the wing of 1852 K. 19

Figure 3.4. Results of CFD simulations for IGFR flame. The solid black line represents the calculated stoichiometric condition: X_{O2}=0.01 (a) X_{O2}, (b) X_{OH} (c) X_{C2H2}. 19

Figure 3.5. TEM images at 70 kx magnification of soot produced from the a) IGFR recirculating flame b) IGFR non-recirculating flame. c) Shows the d_p distribution for the two cases. The

recirculating flame produces soot with primary particles up to a factor of three times larger than non-recirculating flames with minimal overlap. 21
Figure 3.6. HRTEM images from the recirculating flame showing a soot aggregate with primary particles that contain (a) a single-core and (c) multiple cores from a single aggregate (b). Images (d) and (e) show close-ups of the multi-core particles. The distance between the cores is ~20 nm. 23
Figure 3.7. Nanostructure properties using the user-defined method for ROI selection a) fringe length and b) tortuosity analysis from the two defined regions on a given primary particle: 1) Shell and 2) the core. The shell and the core are visually different from HRTEM images. The shell for recirculating and non-recirculating flames is composed of longer fringes, lower tortuosity, and a higher percentage of stacked fringes..... 24
Figure 3.8. Mean nanostructure properties using the radial method for ROI selection as a function of increasing ROI size: a) fringe length, b) tortuosity, and c) percent of stacked fringes. All three plots show good correlation and a higher degree of orientation in the shell compared to the core for recirculating and non-recirculating flames. Error bars represent the standard deviation of the mean values. Eight primary particles are analyzed for both flames. 25
Figure 3.9. Repeated condensation carbonization growth mechanism and supporting HRTEM images of soot produced from the recirculating flame a) primary particle with the internal core similar to previously reported images, with stacked fringes forming from the core to the edge of the particle, giving an onion like appearance, b) a primary particle with multiple cores, and c) the necking between adjacent primary particles appears to be smooth graphitic layers suggesting film deposition after initial aggregation. 29
Figure 4.1. Ethane flames images with (a) Ar-0% vol, (b) Ar-50% vol, and (c) Ar-85% vol (captured with longer exposure). Dilution increases flame length and decreases luminosity due to a decrease in soot concentration. Higher dilution transitions the highest red luminosity point from the flame wing to the flame tip. 36
Figure 4.2. Parameter study to determine the effect of parallel threshold length on the PSF. Increasing the threshold from one pixel (0.02 nm) to 0.20 nm decreases the absolute PSF value linearly. Results are from 13 images of C_2H_4 soot from Figure 6.11. 39

Figure 4.3. Fringe spacing distribution for the zero dilution ethane flame. A secondary peak indicated multiple stacked layers. When the stacking distance threshold is > 0.60 nm, a second peak appears within the set fringe separation measurements. The height of the second peak is 10% to 30% of the primary peak. 40
Figure 4.4. Highest soot luminosity flame temperature for a) methane, b) ethylene, and c) ethane for different fuel dilution ratios. The points correspond to the highest luminosity and the ranges correspond to the range of the axial location with the high flame radiation below the fuel nozzle. In the highest dilution methane flame, the T* requires a radial temperature correction due to the blue flame front. 42
Figure 4.5. OC mass fraction in collected soot particles measured offsite shows an increase with dilution. The presence of OC indicates soot in the high dilution flames has not undergone carbonization. 43
Figure 4.6. HRTEM images for no fuel dilution flames a) methane, b) ethylene, and c) ethane. All three fuels yield mature core-shell particle nanostructure. White arrows point to the shell on the periphery of the particles; colored arrows point to the unstructured core..... 44
Figure 4.7. HRTEM images for intermediate dilution, a) methane – 50%, b) ethylene – 67%, and c) ethane – 50%. Particles have a structured graphitic shell. White arrows point to the shell on the periphery of the particles; colored arrows point to the unstructured core..... 45
Figure 4.8. Highest dilution flames, a) methane – 67%, b) ethylene – 90%, and c) ethane flames – 85%, do not create a graphitic shell. Flame temperatures range from 1495 K to 1568 K. For ethane and ethylene, these flames also produce multi-core particles (core diameter ~5 nm) without shell structure for d) ethylene and e) ethane flames. Orange arrows point to the unstructured portions of the particles, the yellow arrows point to ~5 nm domains.. 47
Figure 4.9. Ethane soot at 85% Ar dilution with 498 K inlet temperature. The preheat increases flame temperature, resulting in core-shell formation. White arrows point to the shell on the periphery of the particles; colored arrows point to the unstructured core. 48
Figure 4.10. Organic carbon content as a function of the PSF in young and mature particles. Soot nanostructure is a good indicator of OC independent of fuel. 50
Figure 4.11. Fringe length and tortuosity for diluted methane, ethylene, and ethane flames. Red boxes represent stacked fringes and black boxes represent non-stacked fringes. Regardless

of fuel, stacked fringes are longer and have a lower tortuosity in comparison to non-stacked fringes. 51
Figure 4.12. Evidence for the soot carbonization mechanism based on internal nucleation. The high dilution and lower temperature flames produce soot particles without a well-defined core-shell structure, shown at 50 kx magnification, similar to PAH-containing particles described by Reilly et al[76]. The soot particle exposed to high temperatures (right column) exhibits a mature soot aggregate structure. HRTEM images at 490kx magnification (middle row center) show the presence of 5 nm crystal nuclei inside of these low-temperature particles. 54
Figure 5.1. Mass production of soot for ethane and ethylene at different dilutions. 60
Figure 5.2. UV-Vis absorbance of methanol soluble extracts from the soot samples. Lower temperature flames absorb more in the UV region. 61
Figure 5.3. Raman spectra of soot produced from the zero dilution ethane flame a) The five-band deconvolution fits raw data from 1000:1800 cm^{-1} with a $\chi 2 = 0.879$ b) The four-band deconvolution fits raw data from 1000:1800 cm^{-1} with a $\chi 2 = 1.595$..... 64
Figure 5.4. Standard five-band deconvolution of Raman spectra from ethane (a,b) and ethylene (c,d) flames. Shown in (a) and (c), dilution does not influence the D3 peak area. Shown in (b) and (d) the D3 band location is the major indicator of D3 band area. 66
Figure 5.5. Four-band deconvolution of Raman spectra from ethane (a,b) and ethylene (c,d) flames. Combining the D2 and G band increases the reproducibility of the spectral analysis (a) and (c) The highest dilution decreases D3 area relative to the graphitic peak. (b) and (d) show the D3 band intensity is not strictly dependent on D3 band location. 67
Figure 5.6. Decreasing maximum flame temperature increases ROS. The lower temperature flames produce particles with lower EC content. 70
Figure 5.7. Comparison between organic carbon composition and a particle's propensity to generate ROS. 70
Figure 5.8. Comparison between TEF and ROS generation. Increasing ROS appears to have a slight impact on TEF measurements. 71
Figure 6.1. SEM images of soot produced in methane/air a) recirculating IGFR diffusion flames b) non-recirculating IGFR flames. The non-recirculating IGFR produces significantly

smaller primary particles compared to the recirculating flame. The scale bar is 500 nm. 73
Figure 6.2. Video of IGFR with recirculation. Particles are observed oscillating in the fuel rich region for an extended period of time. 73
Figure 6.3. Geometry and boundary conditions. The 2D axis-symmetric domain is shown in blue. 76
Figure 6.4. The computational mesh used in CFD. The mesh is reflected upon the axis. 77
Figure 6.5. Contours and pathlines for IGFR simulations. A) H_2O mole fraction b) CO mole fraction c) CO_2 mole fraction d) soot density e) axial velocity (m/s) 78
Figure 6.6. SEM images of soot produced in ethylene/air a) upright and b) recirculating IGFR diffusion flames. The scale bar is 500 nm. 80
Figure 6.7. Primary particle size distribution for C_2H_4/air diffusion flames. The dashed line represents the upright flame; the solid line represents the recirculating IGFR. The recirculating flame has a larger diameter than the upright flame, following the same trend as CH_4/air diffusion flames. The presence of two peaks in the recirculating size distribution is likely to come from particles outside of the recirculating pattern due to the high sooting propensity of ethylene. 81
Figure 6.8. Engineering drawings of the IGFR 82
Figure 6.9. LEFT: Images taken from the flames at oversaturated camera conditions. RIGHT: Low exposure experimental flame pictures used to find the highest soot volume fraction location. The laser seen in the 85% dilution ethane flame is used to set pixel resolution. 83
Figure 6.10. Ethane soot collected with the Inconel probe at 75% dilution. All locations viewed displayed the core shell structure. 84
Figure 6.11. Changing the parallel threshold set at a) 0.12 nm b) 0.16 nm, and c) 0.20 nm. Red fringes are considered stacked. 84
Figure 6.12. All HRTEM images used for nanostructure analysis 87
Figure 6.13. Time dependence for a young soot particle. There seems to be negligible changes over a 22 minute time frame. All HRTEM images were captured within 10 minutes of exposure, so the images are a good representation of the young soot particles 88

LIST OF TABLES

Table 3.1**:** Experimental conditions in the IGFR to produce a recirculating methane flame13
Table 3.2. Growth region flame characteristics and species concentrations from CFD and the simplified CRN network. 20
Table 4.1: Experimental flow rates for the IGFR for flames operated on fuels diluted with Ar. 36
Table 4.2. Average nanostructure measurements for nine flames from HRTEM image analysis. 49
Table 5.1. Raman spectra parameters for the five-band deconvolution method. The four-band deconvolution method combines the D2 and the G peak into one 'G' peak at 1600 cm^{-1}. 63
Table 5.2. Common signal interpretations from Raman spectra using the deconvolution methods. Three or more spectra are measured for each condition..... 65
Table 6.1 CFD boundary condition summary..... 75
Table 6.2: Numerical methods. 75
Table 6.3: Computational results for CFD and CRN models for IGFR flames. Also, resulting soot growth species given by two chemical mechanisms. 79
Table 6.4. Experimental setup and flow rates for ethylene diffusion flames. 80

ACKNOWLEDGMENTS

First and foremost, I want to say thank you to my advisor Igor Novosselov for providing an environment where I was able to grow as a researcher and as a person. You have given me freedom and allowed me to pursue my own interests over the last four years. At the same time, I sincerely appreciate that at any moment during my graduate studies, you were willing to sit down and discuss my research, where the research was going, and provide an outline for the future.

I value the time I spent working with fellow grad students Kartik Tiwari, Eric Molnar, Gaurav Mahamuni, and Chaman Gupta. Collaborating with some of the smartest people I have met has improved my understanding of this fundamental research

Thank you to all my fellow lab mates in the NRG lab. I have had tremendous support whenever I reached out for help and I am very appreciative of the help.

And last but not least, thank you to my family and friends who have supported me through my time at UW.

Chapter 1. INTRODUCTION

1.1 BACKGROUND

Combustion generated particulates have been the subject of extensive research over the last 40 years because they reduce combustion efficiency, increase negative health outcomes, have adverse effects on the environment, and are valuable material for several industrial applications. While there is a wide range of natural and anthropogenic sources, similarities in final particle properties, such as a fractal shape and a graphitic like structure, suggests a universal formation mechanism. This understanding has led to significant advancements in describing the particle formation process, entailing the pyrolysis of fuels that forms small hydrocarbons, the production of stable aromatics, a transition from gas-phase kinetics to solid particles, and further growth, aggregation, and oxidation. These general steps are ubiquitous in soot formation models and have been very successful in predicting emissions and particle properties. While there are great achievements in describing soot formation from first principles, multiple uncertainties persist. It is common to use proxy kinetics in soot formation models because and understanding from first principles remains elusive.

Because of discrepancies between different models, this thesis aims at understanding a number of crucial steps in soot formation, and how they influence soot properties. The second chapter describes different techniques used for experimental work, including the experimental apparatus and characterization techniques. The third chapter explores the role of recirculation on nanoscale properties and provides evidence of a recurring surface growth mechanism. The fourth chapter explores how properties of soot change based on flame temperature for three fuels. The fifth

chapter further characterizes the properties of the particles produced in chapter 4. The sixth chapter provides additional information for the first five chapters.

1.2 SOOT FORMATION FUNDAMENTALS

Due to the high-temperature environment and nanosecond timescales for particle kinetics, it is challenging to create a simple soot formation model that generalizes to a wide range of combustion systems. Still, the soot formation process can be broken into several key steps. Direct observation, such as probing flames with a laser or thermophoretic sampling, changes species concentrations and flow properties. Yet, there have been some significant advances in characterizing different stages of the soot formation process, as shown in Figure 1.1.

Acetylene is one of the most abundant precursors in sooting combustion; thus, it has been proposed that acetylene plays a key role in soot formation. Furthermore, aromatic compounds have been observed in all combustion sources. Aromatics are known to be a critical precursor for soot particles. Their inherent stability allows them to persist in flame environments. Aromatics ultimately cluster to form a condensed phase which appears as a transparent particle. The particles grow through further surface growth and coalescence, based on chemical and physical kinetics. Finally, particles aggregate as the particles grow too large for surface growth to fill any voids, giving the appearance of final spherical particles. Observations of soot aggregates show a structured shell forms on the periphery of the soot particles and an unstructured core. These final particles are opaque in the visible spectrum and have a fractal geometry of 1.7. The particles are then oxidized as they exit the flame.

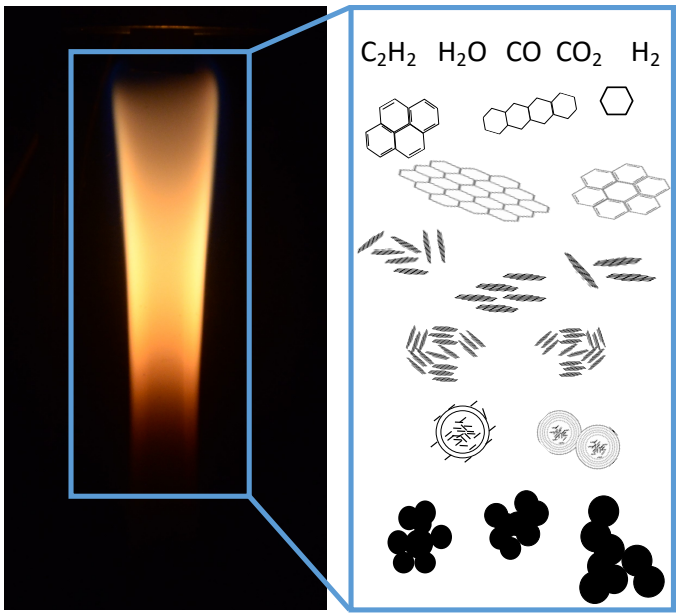

Figure 1.1 Simple soot formation model. Flow moves from top to bottom.

Two of the main unknowns in the soot evolution process include (i) the transition from gas phase to liquid-like particles and (ii) soot maturity. The transition to a condensed phase is commonly modeled by the dimerization of aromatics, yet molecular dynamic studies have shown the associative Van der Walls forces at flame temperature are not strong enough to allow for this dimerization. Another pathway includes radical-induced chemical growth where aromatics grow through continued chemical reactions. However, this pathway is not fast enough to produce final particles. Therefore, a new mechanism is needed. Secondly, the transition from a transparent to an opaque particle is not well understood. Studies have shown internal structural differences between young and soot particles, where an isotropic particle evolves into an onion-like final particle. Yet, the underlying mechanism is not well understood. Hurt explored the formation of a liquid crystal as the soot maturity step, but until recently this transition has not been disregarded [1, 2].

This thesis examines how the internal structure of soot particles evolve based on different combustion conditions and explores possible growth mechanisms based on observed experimental differences between young and mature soot particles.

1.3 HEALTH IMPLICATIONS

According to the World Health Organization, ambient aerosols and indoor pollution from sources such as cookstoves caused 8 million premature deaths in 2016. Combustion generated particulates comprise a large fraction of both fine particulate matter (<2.5 μm) and ultrafine particulate matter (<100 nm). Their size allows them to navigate the branching geometry of the lungs and deposit throughout the pulmonary tract. Meta studies show PM2.5 increases common pulmonary diseases, such as asthma and COPD [3]. Furthermore, the size of the particulates deposit allows them to reach the alveolar region and eventually translocate into the bloodstream. Metadata studies have shown that increased PM concentrations also lead to increased cardiovascular diseases and neurological disorders [4].

1.4 ENVIRONMENTAL IMPLICATIONS

Brown carbon (BrC) and black carbon (BC) have different physicochemical properties despite both being emitted from combustion sources. BC is generated from high-temperature combustion and appears black with an emissivity > 0.9. The highly graphitic particles are typically attributed to sources including tailpipe emissions, industry, and natural gas. BC constitutes a high fraction of ultrafine PM. BC also serves as cloud nuclei and can change local atmospheric properties.

BrC is commonly attributed to lower temperature combustion sources and other organic aerosols (OA) in the atmosphere. However, clustering of gaseous OA in the atmosphere can also produce particulates. These particles have lower absorption in the visible spectrum compare to BC but have an increased absorption in the UV range. While OAs are transparent, BrC particles absorb in the UV range.

The vertical profile of BC and BrC in the atmosphere has direct influences on radiative forcing [5]. BrC can increase radiative forcing by up to 0.11 Wm^{-2} that is a major uncertainty in current climate models [6]. Understanding the totality of PM2.5 in the atmosphere and the implications on radiative forcing is a very intricate problem and outside the scope of this thesis.

Chapter 2. EXPERIMENTAL METHODS

2.1 INVERTED GRAVITY FLAME REACTOR

An inverted gravity flame reactor (IGFR) is used in the experimental work. The co-flow IGFR consists of a quartz tube, 150 mm long with an inner diameter of 32.0 mm. Fuel and air are introduced into the reactor in a downward direction via concentric inlets of 9.5 mm and 32.0 mm diameters, respectively. A flow straightener at the inlet prevents the propagation of instabilities from the air manifold. Figure 2.1 shows the IGFR schematic. The engineering drawings are provided in Figure 6.8.

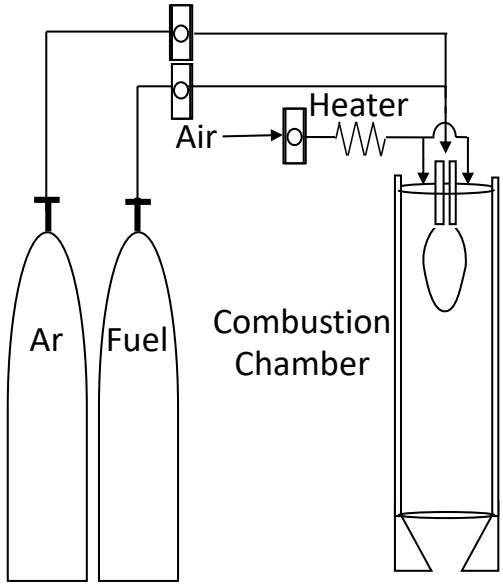

Figure 2.1 IGFR schematic used in experimental work to generate soot particles

2.2 FLAME CHARACTERIZATION

The flame structure and temperature play a critical role in the availability of gas-phase hydrocarbon species required for soot growth, condensation, coalescence, transport, carbonization, and aggregation rates [7, 8]. The flame temperatures are measured using an uncoated R-type

thermocouple (bead diameter ~ 170 μm, wire diameter ~75 μm, measured with an optical microscope). A rapid thermocouple insertion technique is used to reduce soot deposition and temperature correction error [9]. An Arduino/bipolar motor system with a 1/400 revolution resolution positioned below the reactor controls the position of the thermocouple. Thermocouple exposure time in the flame is set at 2.5 seconds when the thermocouple is moved back into the sheath airflow. The process is repeated ten times to find the maximum temperatures for a given location in a given flame.

A radiation temperature correction is calculated using previously reported methods [10, 11]. Heat loss by conduction via the thermocouple wire is neglected. The Nusselt number (Nu) is approximated as that of a sphere, thermal conductivity (k) is approximated using the linear relationship of k and T for air [11], and emissivity ($\varepsilon_{\mathrm{TC}}$) is the average of the two thermocouple wires [10]. Using these assumptions, flame temperature ($\mathrm{T_{flame}}$) is approximated as:

$$T_{flame} = T_{meas} + \frac{\sigma \varepsilon_{\mathrm{TC}} (T^4 - T_{amb}^4) d}{Nuk} \tag{2.1}$$

where σ is the Stefan-Boltzman constant. Catalytic effects are neglected as the temperature measurements are recorded in fuel-lean regions.

2.3 TRANSMISSION ELECTRON MICROSCOPY

TEM allows for the direct observation and characterization of soot particles. Soot is collected on a fiberglass filter (SterliTech 934-AH) downstream of the quartz tube to ensure that the sampling procedure does not disturb the flame environment [12]. A vacuum pump aspirates flow through the filter to improve collection; the collection flow rate is ~5 slpm. After collection, soot is suspended in ethanol, sonicated for 15 minutes, pipetted onto a copper grid, and dried in a desiccator for at least 24 hours. Images are captured using a Tecnai G2 F20 Supertwin TEM

operating at a 200 kV accelerating voltage and a 3 to 5 spot size. TEM images at 70 kx magnification are used to measure d_p. Images from over seven random locations for each condition are captured and the circle equivalent area of over ten primary particles per image (A_{eq}, $d_p = 2\sqrt{A_{eq}/\pi}$) [11, 13] are measured using ImageJ software [14].

High-resolution transmission electron microscopy (HRTEM) analysis provides the direct observation of soot structure. The TEM is operated at a 200 kV accelerating voltage, 5 spot size, and 50k x or 490k x magnification. The 'high-resolution' designation signifies the ability to resolve the soot nanostructure.

2.4 HRTEM IMAGE ANALYSIS

Sample interference with the electron beam reduces the number of transmitted electrons when operated in bright-field mode. Therefore, dark regions in the TEM image reveal the structural properties of a sample. To extract quantitative information related to soot structure from each image, an in-house MATLAB script is developed to process 8-bit grayscale images based on previous reports[15, 16].

1) Choosing a region of interest (ROI) with the 'imfreehand' command
2) Increasing contrast with an adaptive equalization histogram
3) Applying a low pass Gaussian filter to smooth the image
4) A bottom hat transformation with a disk size of 4 pixels to elicit dark regions of the image
5) Binarization using Otsu's method [17]
6) Skeletonizing the image and removing any loops in the skeletonized image
7) Removing pixels with greater than 2 connections and cleaning the image of isolated pixels

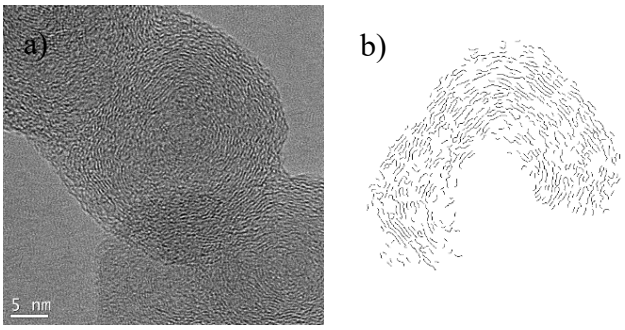

Figure 2.2. Soot sample from the zero-dilution methane flame a) before and b) after processing. The processed image is used to obtain quantitative information from HRTEM images.

After the processing, one-pixel-thick fringes remain. Each processed image is overlaid on the original image to ensure processing accuracy. Figure 2.2 shows examples of raw and processed images. An automated algorithm is used to measure the fringe length (FL), tortuosity, percent of stacked fringes (PSF), and the average separation distance between stacked fringes. The fringe length is computed based on the number of pixels in a given fringe. If the pixels are connected diagonally, the connection length is set to $\sqrt{2}$. The total number of pixels in a given fringe is multiplied by the pixel resolution to determine the fringe length. To reduce noise, all fringes shorter than two aromatic rings in length (0.483 nm) are removed. Tortuosity, a measure of fringe curvature, is computed as the fringe length divided by the Euclidean distance between the endpoints.

Chapter 3. SOOT MORPHOLOGY AND NANOSTRUCTURE IN COMPLEX FLAME FLOW PATTERNS VIA SECONDARY PARTICLE SURFACE GROWTH.

ABSTRACT

While the majority of studies explore soot formation in relatively simple, one-dimensional flames, most real-world flames consist of complex flows defined by large-scale turbulent eddies, recirculating flow patterns, and buoyancy effects. The effects of complex flow on soot physicochemical properties are poorly understood. This work employs an inverted gravity flame reactor (IGFR) to compare differences in soot growth between a one-dimensional laminar diffusion flame and a recirculating flame. Computational fluid dynamics (CFD) and experimental observations show particle oscillations between (i) a rich region with a high concentration of surface growth species, and (ii) a high-temperature oxidation region. Transmission electron microscopy (TEM) shows a significant difference in final primary particle diameter, where the one-dimensional flame produces primary particles 10 to 25 nm in diameter and the recirculating flame produces primary particles 25 to 75 nm in diameter. Additionally, larger primary particles from the recirculating flame contain both single and multiple cores. We propose that due to the spheroidal shape of the large primary particles, the secondary surface growth is primarily a result of polyaromatic hydrocarbon (PAH) condensation during re-entrainment of mature soot into the fuel-rich region followed by subsequent liquid layer carbonization in the high-temperature environment of the flame front. The recirculating flow patterns in the IGFR and repeated particle growth/oxidation cycle can serve as a model for soot formation in the large-scale flames with complex flow patterns, such as forest fires, coal fire plants, and other sources.

The contents of this chapter have been resubmitted to Carbon after an initial request for some revisions in November 2019.

3.1 INTRODUCTION

Primary particle diameter (d_p) is a critical variable in the modeling of soot formation. Final d_p not only provides information about the surface growth rates [18] and structural changes during carbonization [2], but it can also test theories underlying the transition from nascent to mature soot. Most traffic-related emissions, laboratory flames, and soot models produce d_p in the 10-40 nm range [19-22], where d_p is dependent on surface growth rates, the coalescence of liquid like particles, and oxidation. Maximum d_p is reached when the reduction of active sites on the particle surface inhibits further growth [23].

Many real-world combustion scenarios that exhibit complex flow patterns produce soot aggregates with larger primary particles and non-uniform particle size distributions, as seen in soot aggregates from forest fires [22, 24], coal fire plants [25], and buoyant turbulent diffusion flames for liquid and gaseous fuels [26]. The mechanism of soot formation and growth in these scenarios is complex and has not been fully investigated, in part because of the complexity of the models describing primary particle inception and growth combined with a detailed description of fluid dynamics, combustion chemistry, and heat transfer. In recent years, gas-phase chemical mechanisms composed of over one hundred species and one thousand reactions have sought a ground-up approach to particulate formation [23, 27, 28]; these mechanisms include detailed steps of pyrolysis, polyaromatic hydrocarbon (PAH) formation, nucleation, growth, and oxidation [29]. These mechanisms have been implemented with the method of moments [30] and sectional models [31, 32]. The model outputs are validated for specific experiments, typically laminar diffusion flames, but a universal description of particle formation from first principles is a subject of active debate in the literature.

In an inverted gravity flame rector (IGFR), first reported by Stipe et al. [33], the user can vary flow patterns and flame residence time (τ_{res}) by orders of magnitude. The downward flow allows for changing of flow patterns; e.g., the creation of a recirculation region is achieved by altering the balance of the convective and buoyant terms [34]. The increased τ_{res} in the IGFR has been used to synthesize materials such as carbon and TiO_2 aerosol gels [35, 36]. The flexibility in the flame properties also allows for the testing of several hypotheses related to soot formation and growth.

This work investigates the effect a recirculating flow pattern (i.e., fluid dynamics) has on soot nanostructure and morphology. Transmission electron microscopy (TEM) analysis shows that a recirculating flame creates soot aggregates with primary particles ~3x greater than in one-dimensional, non-recirculating flames. We present evidence that the recirculating flow patterns lead to particle growth by recurring surface growth and the subsequent carbonization of the liquid layer in the flame front. High-resolution TEM (HRTEM) supports these conclusions, showing the soot nanostructure from both flames contains ordered fringes surrounding an unstructured core, while the recirculating flame nanostructure contains additional graphitic layers on the perimeter and primary particles with single or multiple cores. Computational modeling provides insight on the flame structure, indicating the availability of precursors for the secondary growth mechanism.

3.2 EXPERIMENTAL METHODS

3.2.1 *Operating conditions to produce recirculating flames*

The recirculating pattern is achieved by reducing the fuel flow until the local buoyancy matches the fuel convective transport term, creating a stagnation plane and forming a buoyancy-driven recirculation cell. Particles trapped in the recirculation cell are in a state of dynamic arrest, with τ_{res} up to several seconds. Particle motion is readily observed due to their emission in the red region

of the spectrum and can be seen in Figure 6.2. The onset of recirculation is less sensitive to airflow rate; therefore, only the fuel flow is varied to induce the desired flow pattern. Flow rates are given in Table 3.1. Preliminary experiments explored recirculating ethylene, propane, and ethane as well. However, these fuels with their higher sooting propensities produced particles in the recirculation cell and in the wing of the flame that bypassed the recirculation cell. To investigate the secondary growth mechanism related to multiple exposures to growth/oxidation

Table 3.1**:** Experimental conditions in the IGFR to produce a recirculating methane flame

	Recirculating	Non-Recirculating
CH4 flow rate (slpm)	0.12	0.19
Air flow rate (slpm)	3.0	3.0
Flame length on-axis (mm)	17	36
Global Equivalence Ratio	0.38	0.60

3.2.2 *HRTEM ROI selection*

Two methods to select the region of interest (ROI) are used to provide structural information of primary particles. First, the “user-defined method” for ROI selection takes into account that the core and shell of a given primary particle are readily distinguishable by eye. Using the “imfreehand” Matlab command, the script allows the user to define an ROI by drawing an ROI border around the desired section. Then, nanostructure information is measured for the core and the shell separately. The second method, referred to as the “radial method” for ROI selection, is used for characterizing the nanostructure properties as a function of radial position. The algorithm defines the ROI as a polygon (kite or hexagon) extending from the center of a given primary particle. To define the primary particle center, a pixel is chosen by drawing multiple lines normal to a primary particle’s perimeter and defining the center at the intersection point. Then, by gradually increasing the ROI area outwards, one can track the evolution of fringe length, tortuosity,

and the percent of stacked fringes. For each ROI size, the entire script is executed, which changes image processing parameters such as the binarization threshold. Larger ROI radius increases the shell/core ratio inside the ROI. For the recirculating case, only images with a single core are analyzed using the radial method.

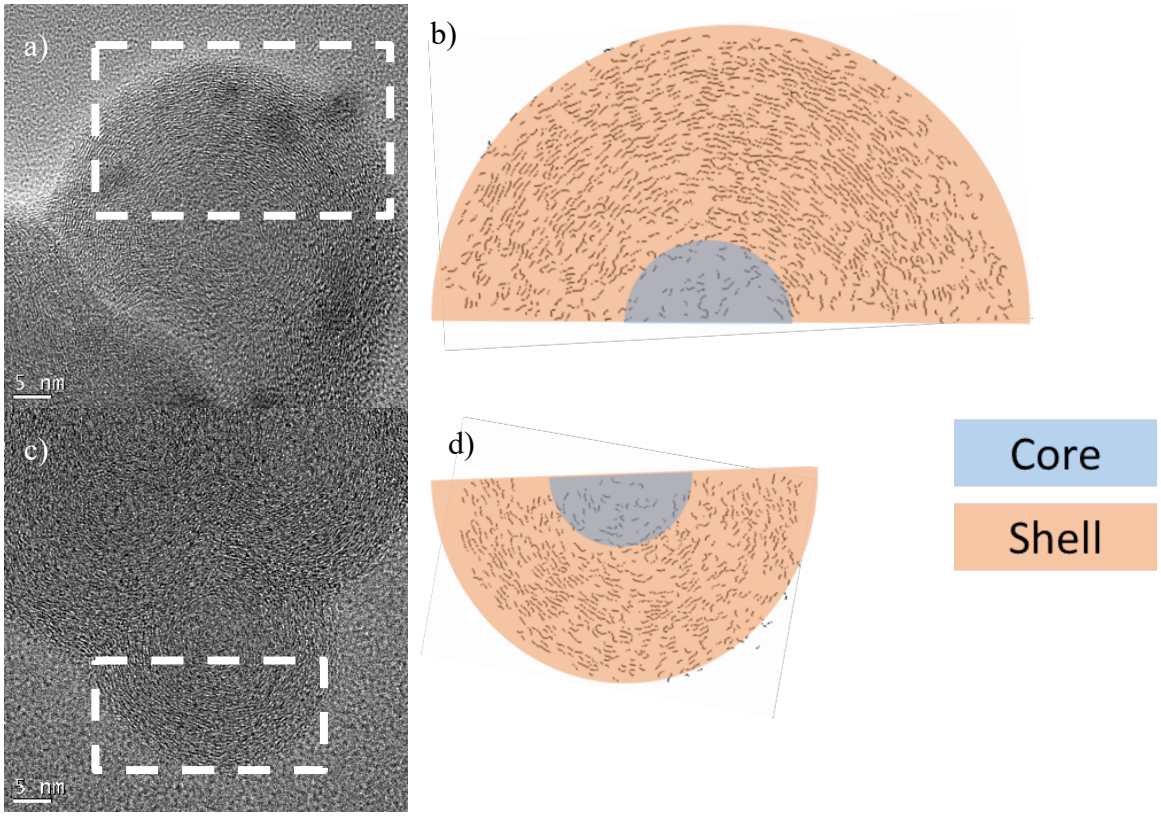

Figure 3.1. Before and after HRTEM images are processed using an in-house Matlab script to extract nanostructure information. a) and b) shows soot from the recirculating flame while c) and d) show soot from the non-recirculating flame. Processed pictures are inverted for publication.

3.2.3 *Chemical reactor network development*

Though the CFD simulations can predict the shape of the flame and the flame temperature, the main drawback is the lack of detailed chemistry including PAH formation, growth, and oxidation, which is critical for the evaluation of soot growth by condensation. CFD simulations were done

by Kartik Tiwari, for information see the publication[37]. Availability of surface growth species for the recirculating and non-recirculating flames are examined using phenomenological CRNs. The overall goal of a CRN is to model local flame conditions while minimizing the number of elements. The available species can then be examined to approximate the contribution of growth due to chemical addition, condensation, and coalescence. The concept of combustion modeling using a CRN was introduced by Bragg [38] to compare the relative importance of kinetic and transport rates. His model used two elements: a perfectly stirred reactor (PSR), an element that assumes homogenous mixing, for the primary combustion zone and a plug flow reactor (PFR), an element that assumes radial homogeneity for the secondary (post-flame) zone. A CFD-CRN approach is useful for performing parametric studies and mechanism comparisons as it shortens the computational time when using large chemical kinetic mechanisms. Various CRN models have been used in studying pollutant formation in laboratory reactors [39-42], industrial systems [43, 44], A reactor network model for predicting NOx emissions in gas turbines[45]. Turbulent flow-field effects in a hybrid CFD-CRN model for the prediction of NOx and CO emissions in aero-engine combustors [46, 47], and flame stability analysis and control [48, 49].

Figure 3.2 shows two CRN arrangements designed from experimental observations of flow patterns, temperature measurements, and the CFD results. The inputs required for the CRN model include the number of elements, fluid flow rates, flow pathways, heat loss, and τ_{res}. The domain is broken into regions representing the fuel rich region conducive to particle growth and the flame front. CFD results used to construct the CRN models include the fluid transport, temperature profiles, τ_{res}, and species concentrations, discussed in section 0. A threshold of $X_{C2H2} > 0.001$ in the CFD defines the soot growth region (PSR1) for both CRNs.

Three different chemical kinetic mechanisms are used in the CRN modeling [50], [27], [28]. All mechanisms include surface growth molecules C_2H_2 and benzene (A1); the Appel et al. and Chernov et al. mechanisms extend the chemistry to include pyrene (A4). The purpose of this work is not to compare the mechanisms but rather to evaluate the trends in species concentration within the domain. Other mechanisms can be evaluated; however, the modeling results with these mechanisms show similar trends. The CRN calculations are performed using Chemkin software [51].

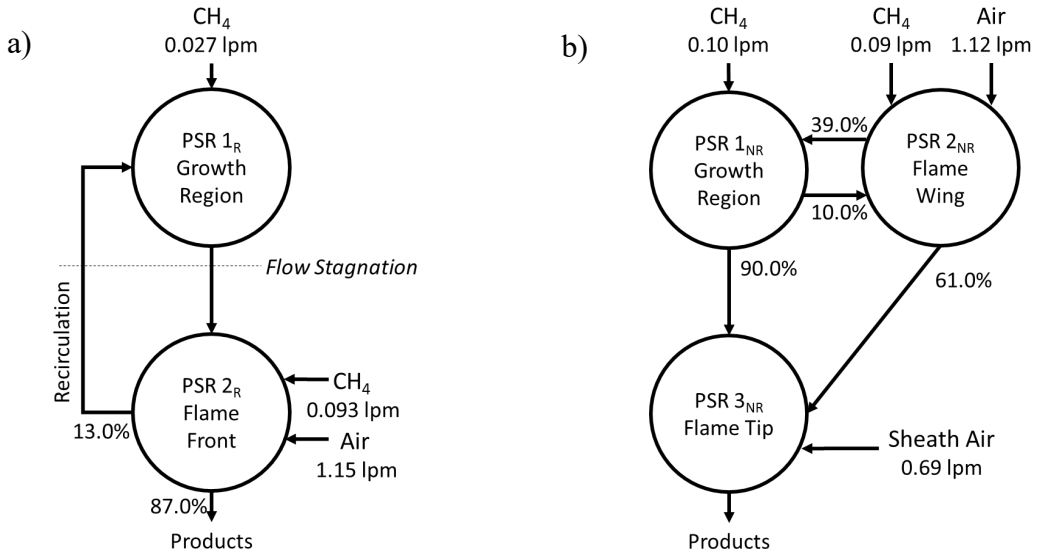

Figure 3.2 Conceptual CRNS for both flames. PSR 1 models a fuel rich region with a high concentration of important growth species for both CRNs. a) IGFR recirculating flame. PSR2R models the flame front. b) IGFR non-recirculating flame. Flow from the wing (PSR2NR) can either diffuse to PSR1NR or travel downstream to the flame tip (PSR3NR).

In the recirculating flow CRN, the flame is split into two PSRs. The flame front - $PSR2_R$ (subscript R denotes recirculating flame) is defined by the region with a high concentration of OH ($X_{OH} > 0.001$) radicals associated with exothermic reactions, i.e., $CO+OH \rightarrow CO_2+H$ resulting in high heat release and the dehydrogenation of soot. The mole fraction of nitrogen (X_{N2}) and zone volume are used to determine the fraction of fuel and air (flow splits) entering $PSR2_R$. A constant

heat loss of 36.6% is assigned to $PSR2_R$ to match the average CFD temperature in the same region. See Table 6.3 for a comparison of temperature and major species in the flame front. By volume, 13% of $PSR2_R$ is recycled into $PSR1_R$ to match CFD region properties of temperature, element volume, and X_{N2}. Nitrogen serves as a tracer gas to calculate the flow split between the elements (NOx chemistry is excluded in both models). Convection from the flame front is the only source of heat into $PSR1_R$, radiation and diffusion are not included.

For the non-recirculating flame, the CRN consists of three PSRs. The flame front on the wing- $PSR2_{NR}$ is defined by the region where $X_{OH} > 0.001$ (subscript NR denotes non-recirculating flame). Air and fuel are both introduced to $PSR2_{NR}$ to match CFD volume and X_{N2}. CFD temperature is matched in $PSR2_{NR}$ by constant heat radiation of 24.0%. Diffusion of 39.0% from $PSR2_{NR}$ injected into $PSR1_{NR}$ is measured by finding the total flow crossing the boundary from $PSR2_{NR}$ to $PSR1_{NR}$ in CFD. With these flow splits, the CRN agrees with the CFD results for temperature and X_{N2} in each element. Convection is the only source of heat entering $PSR1_{NR}$. The flame front at the tip, $PSR3_{NR}$, is also defined by $X_{OH} > 0.001$.

3.3 RESULTS

3.3.1 *Modeling results*

Figure 3.3 compares the CFD temperature with experimental flame temperature and structure. The maximum CFD temperatures for recirculating and non-recirculating flames are 1808 K and 1852 K, respectively. Experimentally, the flame front temperatures were measured at 1791 and 1929 K, respectively. The locations are estimated with 2 mm spatial accuracy that may contribute to the difference in the measurement and the CFD. The lower temperature in the recirculating flame is associated with a lower global equivalence ratio and the long τ_{res}, resulting in larger radiative heat loss. The maximum temperature is found at the stoichiometric plane, shown as a

solid iso-line where $X_{O2} = 0.01$, since $X_{O2} = 0$ does not uniquely define the flame front in the diffusion flames. The zone upstream of the stoichiometric line represents the fuel-rich region. CFD flame shape in the non-recirculating case is slightly longer, which leads to deviations in exact location temperatures. The greatest uncertainty in the CFD results is in the rich part of the flame; there are several significant challenges in predicting the temperature in this region: (i) a complex chemical process resulting in formation of PAH compounds that are not modeled by CFD, (ii) formation and oxidation of combustion aerosols, and (iii) ambiguity in the soot and gas species radiation model. While attempts are made to address the latter two points, the combination of uncertainties in the models and the experimental measurements are likely to produce differences in these complex flame scenarios. Overall, there is a good agreement which supports the use of CFD in constructing the CRNs.

Figure 3.4 shows CFD contour plots of O_2, OH, and C_2H_2. The relatively compact, oxygen-depleted regions in the IGFR recirculating flow is significantly smaller than the flame without recirculation. The X_{OH} contour plot aligns with the stoichiometric iso-line and is used in defining the flame front while X_{C2H2} gives a good representation of the rich region. In the rich region, acetylene is formed by fuel pyrolysis (OH is not present) and disappears rapidly once it reaches the flame front. These X_{OH} and X_{C2H2} thresholds do not intersect or leave large gaps in the CFD domain. Overall, these trends define growth and flame regions in the CRN. The comparison of the CFD and CRN results is shown in Table 3.2.

.

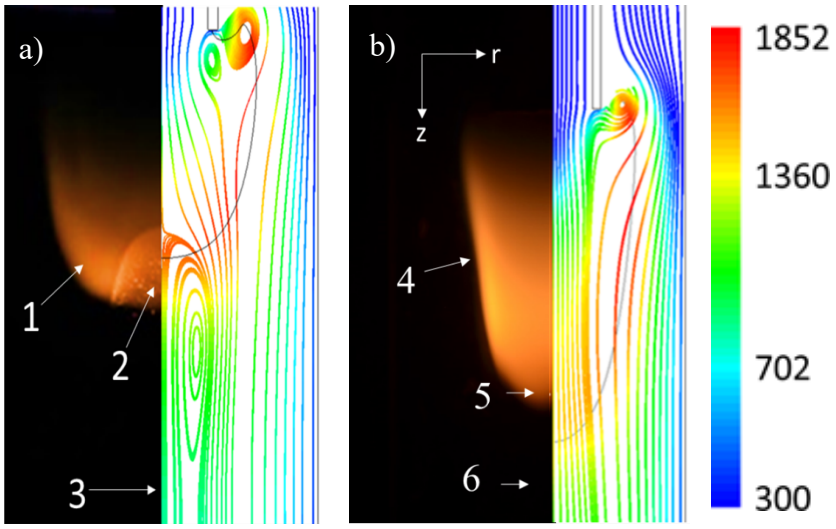

Pos.	(z,r) (mm)	T_{exp} (K)	T_{CFD} (K)
1	(10.0, 9.0)	1789	1791
2	(0.0, 10.0)	1359	1105
3	(0.0, 35.0)	942	949
4	(9.0, 15.0)	1929	1714
5	(0.0, 35.0)	1551	1392
6	(0.0, 45.0)	1227	1259

Figure 3.3. CFD pathlines colored by temperature compared to the photographs of the flame: a) recirculating IGFR, b) non-recirculating IGFR. CFD peak temperatures reach 1808 K and 1852 K, respectively. The solid line shows the near stoichiometric condition (X_{O2}=0.01). For location 2, the thermocouple perturbs upward flow leading to a significant error in the temperature measurement. For location 4, the discrepancy in temperature is in part due to the over-prediction in the CFD flame length. Disagreement is also influenced by the probe insertion into the flame. Location 4 relates better with the maximum flame temperature on the wing of 1852 K.

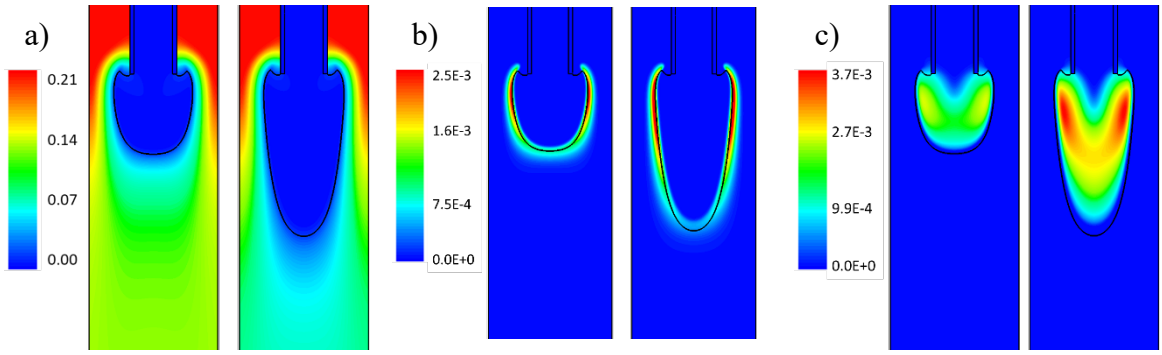

Figure 3.4. Results of CFD simulations for IGFR flame. The solid black line represents the calculated stoichiometric condition: X_{O2}=0.01 (a) X_{O2}, (b) X_{OH} (c) X_{C2H2}.

Table 3.2. Growth region flame characteristics and species concentrations from CFD and the simplified CRN network.

GROWTH REGION (PSR1)	IGFR Recirculating Solution				IGFR Non- Recirculating Solution			
	CFD	CRN, mech [50]	CRN, mech [27]	CRN, mech [28]	CFD	CRN, mech [50]	CRN, mech [27]	CRN, mech [28]
Volume (cm^3)	7.2	7.1	7.0	7.1	13.3	13.3	13.3	13.3
Temperature (K)	1335	1359	1314	1358	1342	1361	1332	1345
τ_{res}(sec)	0.28	0.43	0.43	0.43	0.20	0.27	0.27	0.27
X_{N2}	0.63	0.62	0.61	0.62	0.63	0.60	0.59	0.60
X_{H}	7.6E-6	1.0E-7	2.3E-7	1.4E-7	9.2E-6	7.2E-7	8.1E-7	5.4E-7
X_{H2}	8.0E-3	8.8E-3	3.3E-2	1.2E-2	9.0E-3	3.1E-2	6.0E-2	2.7E-2
X_{CH4}	0.12	0.12	0.10	0.12	0.12	0.12	0.11	0.12
X_{OH}	5.2E-6	3.0E-8	1.7E-8	3.6E-8	6.6E-6	7.7E-8	4.8E-8	7.0E-8
X_{CO}	1.6E-2	5.3E-3	7.3E-3	5.8E-3	1.8E-2	1.8E-2	2.7E-2	1.8E-2
X_{C2H2}	1.8E-3	1.2E-3	4.8E-3	6.8E-4	2.5E-3	3.0E-3	4.7E-3	1.4E-3
X_{C3H3}	-	7.4E-7	-	4.4E-6	-	1.1E-6	-	4.8E-6
X_{A1}	-	9.3E-6	1.6E-4	2.4E-4	-	1.0E-5	7.2E-5	6.7E-5
X_{A2}	-	7.1E-9	4.6E-6	-	-	2.4E-8	5.3E-7	-
X_{A3}	-	1.9E-10	1.1E-5	-	-	2.8E-10	8.3E-7	-
X_{A4}	-	4.3E-12	2.1E-5	-	-	1.6E-11	2.0E-6	-

The CFD model estimates the particle size based on the C_2H_2 and C_2H_4 precursors computed by the GRI 3.0 mechanism. The d_p from the CFD simulations are ~20 nm for recirculating flame and ~40 nm for the non-recirculation flame. The discrepancy with the experimental measurement is likely due to the fact that the simulations do not account for the PAH condensation route and particle surface chemistry, which are required to describe soot growth. The concentrations of PAHs are evaluated by the CRN modeling.

Table 3.2 shows the availability of the surface growth species in the fuel-rich region. For the Chernov et al. mechanism, X_{A4} is an order of magnitude greater for the recirculating flame compared to the non-recirculating flame (2.1E-5 vs. 2.0E-6). The Appel mechanism predicts negligible X_{A4} (4.3e-12 vs. 1.6E-11). The increase in PAHs for the Chernov et al. mechanisms is despite the fact that the fuel rich region contains an equivalent X_{C2H2} for both flow patterns. The higher concentration of X_{A4} strongly suggests higher concentrations of larger PAHs as well and points to the increased role of condensation in the recirculating flame.

3.3.2 *TEM analysis*

Figure 3.5 shows representative TEM images and the distribution curves for d_p. Both samples consist of fractal aggregates of spherical primary particles. The d_p average and standard deviation is measured at 53.0 nm ± 8.0 nm (n=135) for the recirculating flame and 17.1 nm ± 2.4 nm (n=100) for the non-recirculating flame. Samples appear uniform, and particle size distribution is independent of the measurement location. SEM images with lower resolution support TEM finding for a larger statistical sample (n~300), given in Figure 6.7.

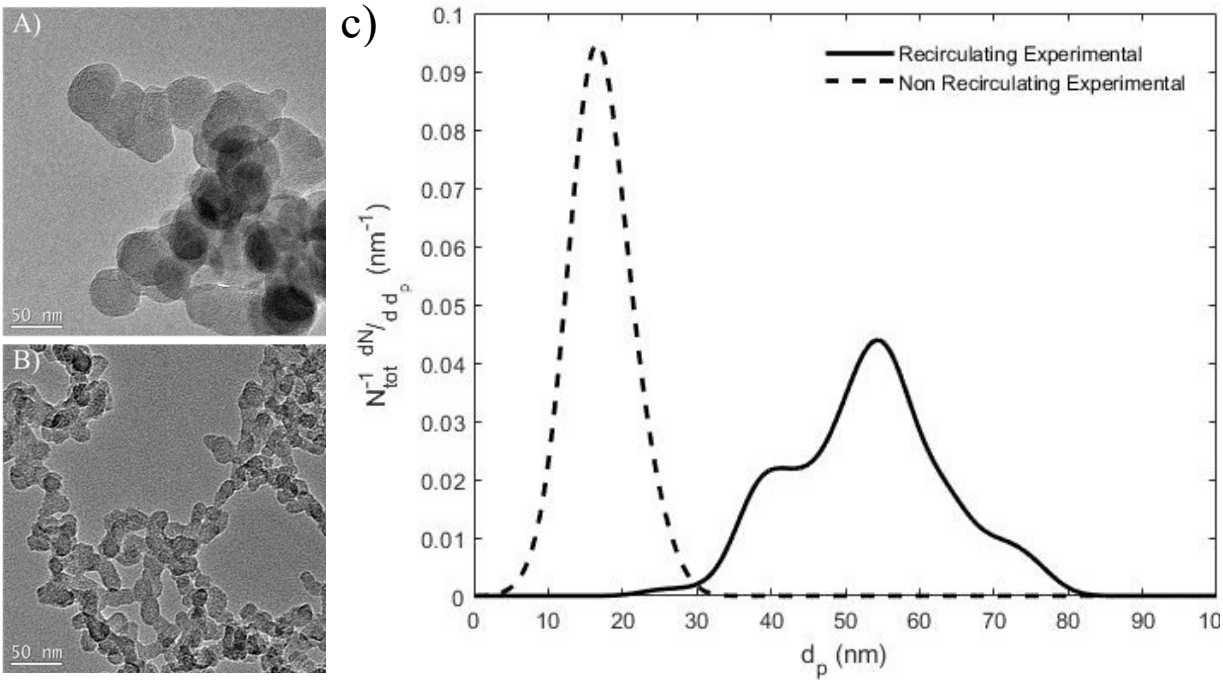

Figure 3.5. TEM images at 70 kx magnification of soot produced from the a) IGFR recirculating flame b) IGFR non-recirculating flame. c) Shows the d_p distribution for the two cases. The recirculating flame produces soot with primary particles up to a factor of three times larger than non-recirculating flames with minimal overlap.

HRTEM images show the core and shell structure for both methane flow patterns. The measured d_p distribution for the recirculating flame in Figure 3.5 appears to have two peaks, diverging from the typical d_p log-normal distribution. Figure 3.6 provides insight into the cause for larger primary particles. Images from the recirculating methane flame reveal primary particles with both a single

core and multiple cores. The presence of multiple cores in soot particles has been noted in the past for biomass [52] and diesel smoke [53]. For the given image, the single core particle has a d_p ~42 nm. For the images given with multiple cores, $d_p > 60$ nm. The multiple cores are a distance of 20 nm apart. This distance corresponds to the average d_p for the non-recirculating case. Because TEM requires a thin sample for electrons to transmit, two primary particles stacked upon each other do not allow for the visualization of the shell structure; yet, for these particles, distinct shells are in focus simultaneously so they must be in the same z plane.

The SEM results for ethylene flames show a larger d_p for the recirculating flow (Figure 6.6 and Figure 6.7). The size distribution appears to have three modes, possibly due to the contributions of soot formed outside the recirculation zone (d_p=20 to 35 nm) as well as the presence of a bimodal distribution associated with single-core and multi-core particles (analogous to the methane case for the particles formed in the recirculation zone). The results for ethylene and other fuels need to be further evaluated using HRTEM.

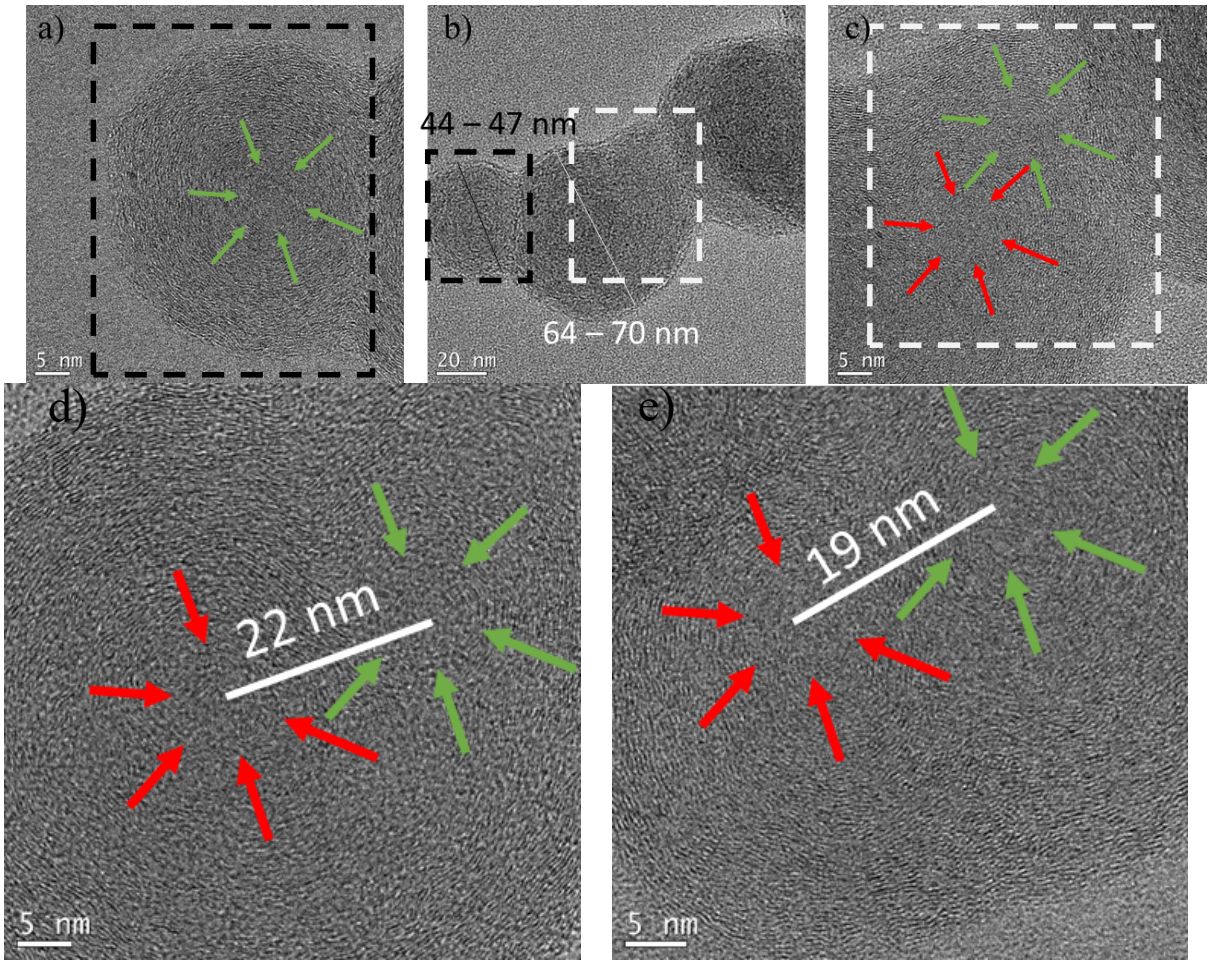

Figure 3.6. HRTEM images from the recirculating flame showing a soot aggregate with primary particles that contain (a) a single-core and (c) multiple cores from a single aggregate (b). Images (d) and (e) show close-ups of the multi-core particles. The distance between the cores is ~20 nm.

For the recirculating methane flame, the structured shell contains additional graphitic layers compared to a non-recirculating flame. The quantitative analysis of the fringe length, tortuosity, and stacked layers are presented in Figure 3.7 using the user-defined method for ROI selection. In the core, the average fringe lengths are 0.67 and 0.71 nm for non-recirculating and recirculating soot, respectively. Assuming D_{2h} symmetry [54], the cores are mostly composed of PAHs between pyrene and ovalene ($C_{32}H_{14}$); these PAHs are anticipated to be involved in particle nucleation [7]. The shell contains larger average fringe length of 0.77 and 0.86 nm for non-recirculating and

recirculating soot, respectively. Again, assuming D_{2h} symmetry, the shell is likely to be mostly composed of a graphitic structure formed from compound equivalent in size to ovalene and circumpyrene ($C_{42}H_{16}$). Spatial distribution of soot nanostructure is also evaluated using the radial method for ROI selection. Figure 3.8 shows that increasing ROI coverage from the center of a primary particle increases average fringe length, decreases average tortuosity, and increases the percentage of stacked fringes. The particle nanostructure is similar up to d_p~20 nm for both cases, even though the overall particle size is significantly different. This similarity suggests that the recirculating primary particles are initially formed in the same manner as the non-recirculating primary particles. Secondary surface growth in the recirculating flow produces stacked fringes with longer dimensions.

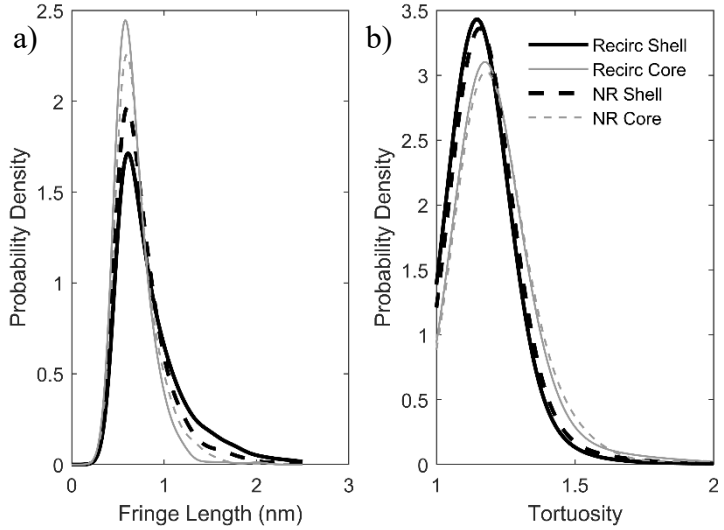

Region	Average Fringe Length (nm)	Average Tortuosity	% Stacked Fringes
Recirculating Core	0.71 ± 0.24	1.21 ± 0.13	60.0 ± 16.1
Recirculating Shell	0.86 ± 0.41	1.17 ± 0.14	82.2 ± 6.3
Non-Recirculating Core	0.67 ± 0.19	1.23 ± 0.11	49.1 ± 12.2
Non-Recirculating Shell	0.77 ± 0.29	1.18 ± 0.22	72.8 ± 3.7

Figure 3.7. Nanostructure properties using the user-defined method for ROI selection a) fringe length and b) tortuosity analysis from the two defined regions on a given primary particle: 1) Shell and 2) the core. The shell and the core are visually different from HRTEM images. The shell for recirculating and non-recirculating flames is composed of longer fringes, lower tortuosity, and a higher percentage of stacked fringes.

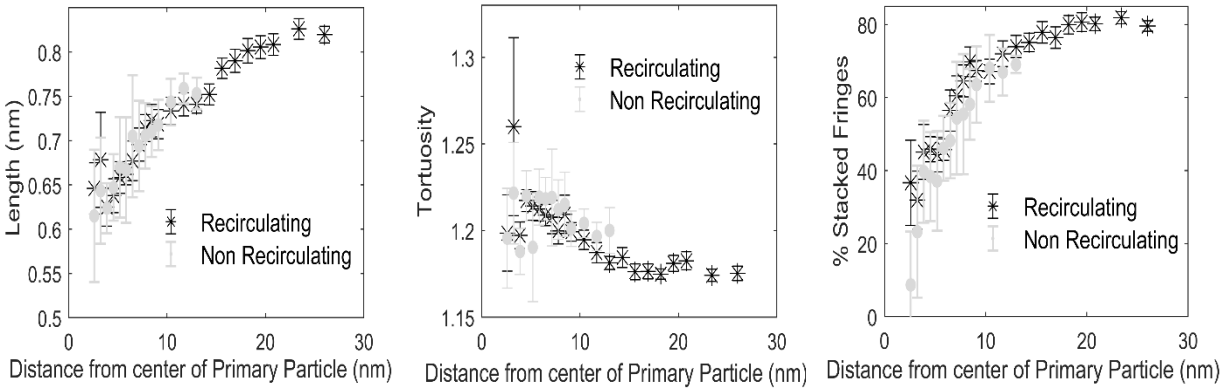

Figure 3.8. Mean nanostructure properties using the radial method for ROI selection as a function of increasing ROI size: a) fringe length, b) tortuosity, and c) percent of stacked fringes. All three plots show good correlation and a higher degree of orientation in the shell compared to the core for recirculating and non-recirculating flames. Error bars represent the standard deviation of the mean values. Eight primary particles are analyzed for both flames.

3.4 DISCUSSION

We observe that the recirculating flow creates primary particles and aggregates with more complex nanostructures that are not explained by current models. Due to results from this study and previous studies on soot evolution, the increased d_p in the recirculating flame is likely a result of secondary surface growth on mature soot particles due to recurring exposure to the growth and high temperature regions in the recirculating flow.

Unlike one-dimensional flow scenarios typically studied using laboratory burners, recirculating flow patterns in the IFGR result in complex interactions of several processes, i.e., particle inception, coagulation, surface growth, carbonization, agglomeration, and oxidation. Due to the final spheroidal shape shown with HRTEM images, the secondary growth mechanism in the recirculating flame is likely to be the condensation of liquid PAH species on the mature particles or their aggregate. The high concentrations of these PAHs in the growth region is corroborated by CRN modeling. Supporting evidence for secondary particle growth are discussed below.

First, can the increase in τ_{res} by itself be responsible for the 3x increase in d_p? Previous reports [35] show that upright coaxial flame configuration with τ_{res} ~ 10 to 20 ms as well as our own experiments produce primary particles 10 to 20 nm in diameter, similar to the non-recirculating IGFR flame with τ_{res}~200 ms. While high temperature τ_{res} possibly influences particle size, it does not explain the presence of spheroidal particles with multiple cores, which suggests that the three-fold increase in d_p cannot entirely be due to the increase of the τ_{res} in the flame.

Second, can the recirculating flame increase coalescence that leads to an increase in d_p? In both the recirculating and one-dimensional inverted flame, the streamline reaches the flame front in 0.20 to 0.28 seconds. Once exposed to the flame front temperatures, we assume the particle shell is formed, and the structure is 'locked-in' [55]. Previous studies suggest a temperature of greater than 1500 K is necessary [2, 55]; our flame temperature is greater than ~1800 K. Thus we conclude that increase in d_p seen is not due to the coalescence of liquid droplets as the multi-core particles in Figure 3.6 supports the initial 'locked in' structure.

A third possibility for larger d_p can be the increase in X_{PAHs} in the recirculating flame. PAH condensation has been shown to influence d_p in simple flames [56-58]. The CRN modeling shows that the recirculating case has a higher concentration of PAHs pointing to the increased contribution of the condensation route in the recirculating case. However, it has been reported that during surface growth, PAH condensation is reversible, where PAHs boil off from the surface leaving only a thin condensed layer [59]. Desorption kinetics are required for accurate condensation kinetics [57]. It is possible that in some scenarios the PAHs significantly contribute to the particle growth, especially in the lower temperature flames with the lower soot yield.

The proposed secondary particle growth process is initiated when a mature particle is re-entrained into the fuel rich region. The particles trapped in the recirculating flow experiences multiple

growth/oxidation cycles resulting in the structures reported in the current study. Three examples for secondary particle growth are considered: (i) a single core large mature particle, (ii) a large primary particle with multiple cores, and (iii) increased bridging between large primary particles in the aggregate. These pathways have some similarity with surface growth and coagulation proposed in [60]. However, the main difference is that the proposed mechanism takes into account the interaction with the mature particle surface, which is important during the secondary surface growth [61, 62].

(i) A single mature particle (d_p < 25 nm) recirculates into the fuel-rich region. A liquid layer deposits on the periphery of the particle by PAH condensation. Because the particle is mature, there will be a reduced number of aryl sites on the surface and the initial growth by condensation is more likely. The condensed PAHs can then allow for further growth through HACA as well. Subsequent graphitization in the flame front then results in the formation of a larger, single core particle. The size of the particle depends on a number of cycles and species concentration of the growth region. Figure 3.6(a, b) shows a single-core particle as a part of the soot aggregate; the single core particle is 40 to 50 nm in diameter -- smaller than other particles in the aggregate. This route is shown in Figure 3.9a.

(ii) An initial aggregate, composed of primary particles 10 to 25 nm in diameter, recirculates into the fuel-rich region where further surface growth occurs. Liquid PAHs fill the crevices in the aggregate in the growth region, then while re-exposed to the high-temperature flame front, the new layer undergoes carbonization - the result is a spherical particle with multiple cores. This route is shown in Figure 3.9b. Additional multiple core TEM images are shown in Figure 3.6 (b-e). The typical size range of the multi-core particle is 60 to 80 nm, which is greater than single-core particles (40 to 50 nm), resulting in a bi-modal size distribution as seen in Figure 3.5 (c). Note that

the distance between the cores (~20 nm) corresponds to the size of the primary particle in the non-recirculating flame. This serves as a confirmation that the multi-core particles are formed by aggregation of the two or more mature particles (d_p~20 nm) followed by the additional growth/oxidation cycles.

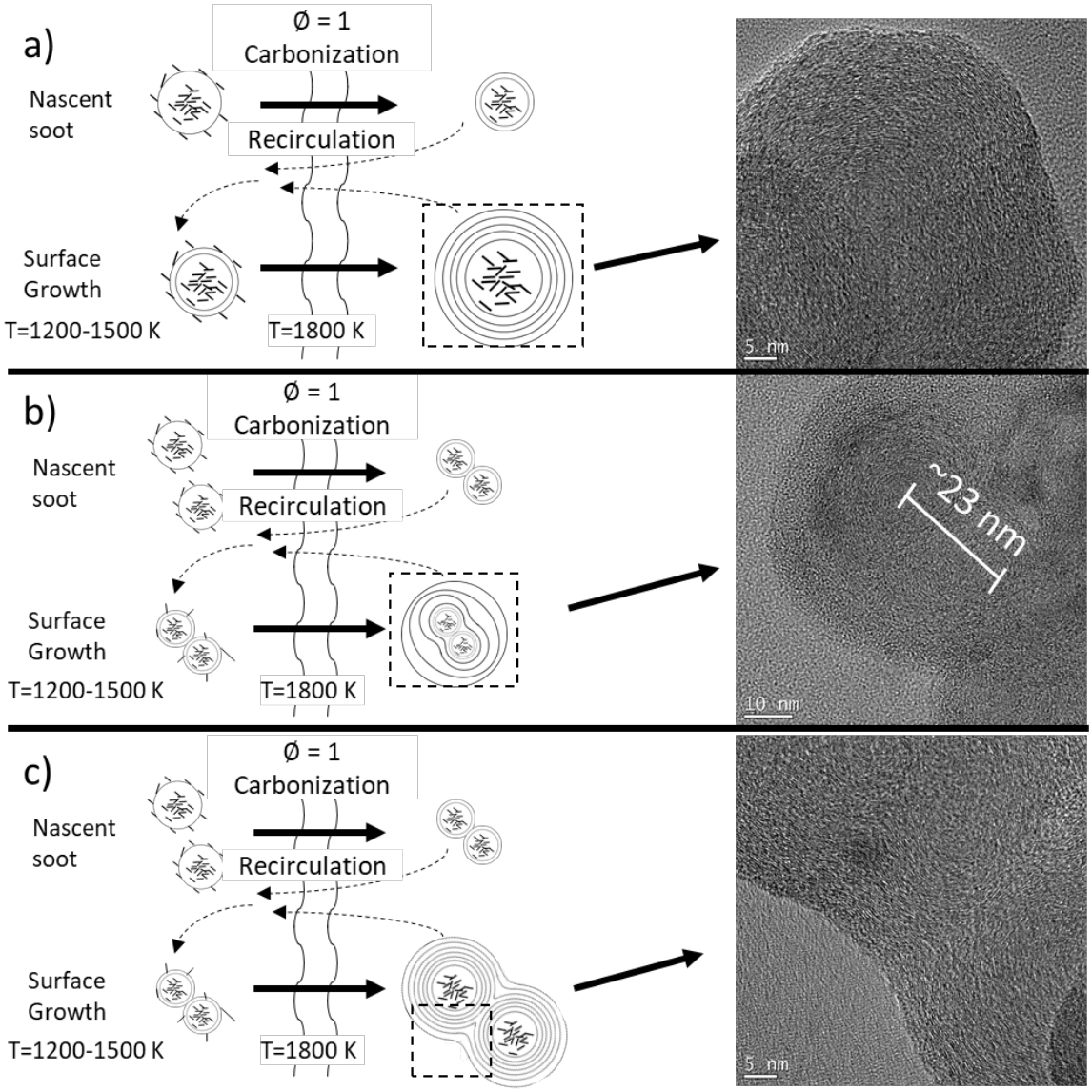

Figure 3.9. Repeated condensation carbonization growth mechanism and supporting HRTEM images of soot produced from the recirculating flame a) primary particle with the internal core similar to previously reported images, with stacked fringes forming from the core to the edge of the particle, giving an onion like appearance, b) a primary particle with multiple cores, and c) the necking between adjacent primary particles appears to be smooth graphitic layers suggesting film deposition after initial aggregation.

(iii) Increased bridging between primary particles in the aggregate. An aggregate consisting of larger spherical particles recirculates to the growth region, where surface growth forms additional

graphitic layers bridging the spaces between the particles in the aggregate. Subsequent carbonization when exposed to the flame front results in smoothened soot aggregates. This route is shown in Figure 3.9c.

The nanostructure analysis supports secondary surface growth mechanism that is initialized by PAH condensation on the particles and aggregates with graphitic shells. The fringe length and percent of stacked fringes from the recirculating and non-recirculating flames are similar up to 10 nm from the center (Figure 3.8) corresponding to the d_p of the non-recirculating primary particles. This suggests that the particles in the recirculating flame are initially formed in the same manner as the non-recirculating case. The nanostructure of the recirculating particles up to $d_p = 20$ nm has been 'locked-in' by the initial particle exposure to the high-temperature flame front. The larger d_p is due to the recirculating flows and re-exposure to the region with a high concentration of surface growth species (X_{C2H2} ~1.3E-02, X_{A4} as high as 1.2E-06). Additionally, longer average fringe length is observed for the recirculating particles (0.77 to 0.86 nm). It is possible that the increased fringe length is associated with condensation growth on the existing graphitic structures.

3.5 CONCLUSIONS

Increase in primary particle diameter in the complex recirculating flow is attributed to the secondary particle growth driven by repeated exposure to the growth region (i.e., fluid dynamics) rather than to τ_{res}, temperature, or precursor concentration. The secondary surface growth is initiated by PAH condensation during re-entrainment of single mature soot particles or their aggregates into the fuel-rich region of the flame. Additional work on the mechanism responsible for surface growth and carbonization is needed to better understand the complex interactions between the flame species and particles.

Chapter 4. NANOSTRUCTURE TRANSITION OF YOUNG SOOT AGGREGATES TO MATURE SOOT AGGREGATES IN DILUTED DIFFUSION FLAMES

ABSTRACT

In this study, the structural properties of soot produced in diffusion flames are analyzed to elucidate the formation of mature aggregates from large young particles. Soot samples are generated in a laminar diffusion inverted gravity flame reactor (IGFR) operated on methane, ethane, and ethylene with Ar dilution to reduce the flame temperature. Soot produced in temperature ranges from 1495K-1568K contains 100nm-300nm particles with (i) isotropic or (ii) multiple core structures, supporting a soot maturation pathway where one young soot particle evolves into a mature fractal aggregate via an internal nucleation route. During the process, these large amorphous particles can form internal voids as the particle loses mass due to pyrolysis or oxidation. Transmission electron microscopy (TEM) shows that young soot aggregates contain a higher fraction of shorter fringes and highly curved aromatics (11% vs. 23%), which agrees with their higher organic carbon content (3.3%-5.4% vs. 12.1%-28.8% wt.). Increasing the flame temperature reduces the curvature of polycyclic aromatic hydrocarbons (PAHs) and allows for more efficient layer stacking as indicated by a higher percent of stacked fringes. For these gaseous fuels, carbonization appears to be primarily a function of the flame temperature and independent of the fuel composition.

4.1 INTRODUCTION

Combustion-generated particulate matter (PM) containing black carbon (BC) and brown carbon is a major component of air pollution with known health risks [63] and adverse environmental impacts [64]. Several questions related to the formation and evolution of soot particles that dictate the physicochemical properties of PM remain a subject of scientific debate [65]. Particularly, insights into soot maturation and aggregation are needed to improve our understanding of the influence fuel composition and combustion conditions have on PM morphology and reactivity [66, 67]. These insights can be used in the optimization of combustion systems to minimize adverse health and environmental effects.

The planar nature and inherent stability of aromatic compounds are linked to the formation of soot particles [68, 69]. More than 100 polycyclic aromatic hydrocarbons (PAHs) cluster together to form liquid-like particles in flames with temperatures greater than 1350 K [70]. The size of PAHs in young soot has been approximated by molecular dynamics simulations to be between four rings (pyrene) and 19 rings (circumcoronene) [7, 31]; this range agrees with PAH sizes observed by atomic force microscopy [69]. Young soot particles appear to be transparent and isotropic. A recent report shows that smaller PAHs may reside near the surface and larger PAHs cluster near the core [71]. While typically only planar PAHs are used in soot models, curved aromatics may play a significant role in soot formation due to higher kinetic growth rates [72]. Curved aromatics have a permanent dipole that can increase rigidity [73].

After nucleation, young particles grow through surface growth and collisions with other young particles, leading to their coalescence and agglomeration. Coalescence is the merging of two particles into one, whereas during agglomeration the particles collide but keep their initial shape, creating a fractal structure. In computational models, particle critical diameter (5 nm to 35 nm)

[13] or characteristic times [74] are used to determine a threshold for the transition from coalescence to agglomeration. The computational thresholds are typically tuned to match experimental results; however, previous work has shown that multiple processes related to soot growth and maturation can occur at the same time [60]. Furthermore, until recently [2], computational models have not taken into account the internal organization of soot particles. Pyrolysis studies have shown that a graphitic shell forms on the periphery of mature soot particles in a range of temperatures between 1523 K and 1923 K [55]. Experimental studies using thermophoretic probing show that, in diffusion flames, the shell forms as particles travel through temperature regions > 1500 K [71, 75]. Identifying the exact transition temperature in sooting flame conditions is challenging and likely cannot be assigned to a single value. Understanding the maturation process is critical because it affects particle absorption, emissivity, reflection, and is directly involved in the coalescence kinetics.

Reilly et al. proposed an aggregate formation mechanism that is driven by the particle's internal structure [76]. The authors report the presence of large "PAH-containing" particles in laminar acetylene diffusion flames. These young soot particles, measured to be on the order of 0.5 microns to 1.0 micron, later evolved into mature soot aggregates. The mature soot aggregates were of similar size and largely depleted of PAH species. The authors concluded that young soot particles could form large unstructured aggregates and then transition to mature aggregates with multiple core-shell sites ~20 nm in diameter [76]. Other researchers have shown these large, liquid-like, particles without well-defined spherical primary particles exist inside the flame [75] and can be persist post-flame [77]. Further characterization of these large, unstructured particles and their transition to the multi-core soot aggregate can provide critical insight into the soot maturation process. The young soot can be produced in low-temperature flames below carbonization

temperatures, which can be readily achieved in an inverted gravity flame rector (IGFR) operated with diluted fuels. This type of reactor design was first reported by Stipe et al. [33] and has since been used to synthesize materials such as carbon and TiO_2 aerosol gels [35, 36].

This work aims to provide experimental data on the transition of young soot to mature aggregates through the analysis of soot chemical composition and structure at different stages of their maturity. The combustion conditions in the IGFR are varied to evaluate the effects of dilution and temperature by (i) introducing Ar to the fuel stream and (ii) reagent preheating. The laminar diffusion flame is operated on methane, ethylene, and ethane with up to 90% Ar dilution by volume. Low-temperature flames yield particles 100 nm – 300 nm, each with an isotropic structure and a high fraction of curved PAHs. High-temperature flames produce aggregates with similar overall dimensions, composed of smaller (~20 nm) core-shell structures. The reduction in curved PAHs during carbonization is hypothesized to be a significant contributor in forming the core-shell structure.

4.2 EXPERIMENTAL METHODS

4.2.1 *Operating conditions to produce diluted flames*

A fuel-Ar mixture, up to 90% by volume, is introduced through the inner inlet tube. Air is introduced through the outer anular section. Ethylene (Praxair 99.5%), ethane (Airgas 98.5%), and methane (Praxair 99.0%) are selected due to their different sooting propensities. The experimental conditions and flow rates are given in Table 4.1. Figure 4.1 shows ethane flame images with varied fuel dilution. Methane and ethylene flame images are shown in Figure 6.9. Flame images, taken at varied exposures to avoid image saturation, are used to find the location of the maximum soot radiation as described in 4.2.2. The highest dilution ratio is determined by our ability to collect sufficient particle sample for analysis.

Soot is collected on a fiberglass filter (SterliTech 934-AH) at the reactor exit to ensure the collection does not disturb the flame structure. For the highest dilutions, the orange flame tip indicates the formation of soot; however, the total soot yields are significantly lower at these conditions. The lower flame radiation in the red region indicates the lack of particles with a carbonized shell, which increases emissivity [67, 78]. For these low sooting conditions, a secondary collection method was used. An Inconel probe 3.175 mm in diameter was placed at the tip of the flame, ~2.0 mm from the tip of the flame for 30 seconds. The probing did not change the flame structure. To verify that the sampling procedure did not influence the particle structure, i.e., did not quench particle carbonization, samples from a 75% diluted ethane flame were collected on the probe. These samples show a mature nanostructure, similar to the other lower dilution cases, see Figure 6.10. Similar flame probing has been used in previous studies that concluded that a carbonized shell forms before soot reaches the oxidation region [71].

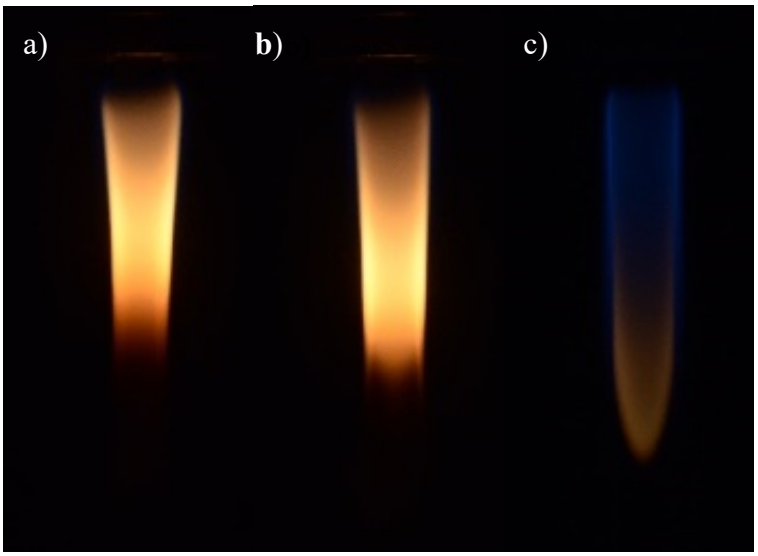

Figure 4.1. Ethane flames images with (a) Ar-0% vol, (b) Ar-50% vol, and (c) Ar-85% vol (captured with longer exposure). Dilution increases flame length and decreases luminosity due to a decrease in soot concentration. Higher dilution transitions the highest red luminosity point from the flame wing to the flame tip.

Table 4.1: Experimental flow rates for the IGFR for flames operated on fuels diluted with Ar.

	CH_4			C_2H_4			C_2H_6		
Flame	1	2	3	4	5	6	7	8	9
Fuel flow rate (slpm)	0.24	0.24	0.24	0.12	0.12	0.12	0.12	0.12	0.12
Air flow rate (slpm)	2.72	2.72	2.72	2.72	2.72	2.72	2.72	2.72	2.72
Ar Flow Rate (slpm)	0	0.24	0.48	0	0.12	1.08	0	0.12	0.68
Dilution Percentage	0.0	50.0	67.0	0.0	67.0	90.0	0.0	50.0	85.0
Max Flame Temperature (K), T_{max}	1957	1898	1816	1968	1934	1746	1946	1918	1749
Temperature at Max Radiation Location (K), T^*	1774	1734	1783	1901	1701	1508	1727	1672	1521
Flame Length (mm)	54	60	62	42	50	75	51	59	78
Open Tip	Yes	Yes	No	Yes	Yes	No	Yes	Yes	No

4.2.2 *Maximum soot luminosity region analysis - temperature estimation*

The downstream shift in the highest flame luminosity location, coupled with an elongated flame structure, shown in Figure 4.1, complicates temperature measurements for soot characterization. The maximum flame temperature is measured on the flame wing 10 mm to 20 mm (axially) from the inlet. However, in the high dilution flames, there is not red radiation in this location. Since luminosity in the red spectra depends on soot temperature and soot volume fraction (f_v), the maximum flame temperature does not correspond to the environment relevant to soot maturation. Here, we characterize soot maturation by T^* — the highest estimated soot temperature, i.e., the flame temperature at the location of the highest radiation. Images of each flame are captured, and the red layer of each image is processed to find the axial location with the highest luminosity, see Figure 6.9. Previous reports show that the maximum f_v is located in the fuel-rich region of the diffusion flame front and can have a lower temperature than the flame front by 150 K to 300 K [11, 79, 80]; thus, T^* characterizes the upper temperature limit of soot exposure. The 67% dilution methane also includes a radial temperature correction (T_{radial}) to account for shift in the visible soot radiation region away from the flame front, as discussed in section 4.3.1. This estimate is most accurate for the highest dilution cases as the highest luminosity is at the tip of the flame where path lines are orthogonal to the flame front and the soot particles must travel through that temperature region before exiting the flame. These low-temperature flames with a closed tip structure are of the most interest to this work as they produce soot with a disordered structure.

4.2.3 *Measuring the percent of stacked fringes*

Special consideration is given to calculate the PSF. PAHs stack due to the overlapping of π orbitals, aligning graphitic layers in parallel orientation [81]. In previous work, fringes have been selected by hand to extract the separation distance [15]. We found that this method introduces user

bias. To reduce uncertainties with measuring lattice spacing, we have automated the procedure. The algorithm labels a pair of fringes as stacked if they satisfy three conditions: the pair 1) forms a relative angle < 10 degrees, 2) are located within 0.80 nm, and 3) run parallel for a threshold distance set at 0.20 nm. The algorithm follows the following steps:

1. The script assigns each pixel on a given fringe an angle represented by the sum of the vector components for the five nearest pixels on the fringe. The use of vector components improves upon previous techniques where an angle was assigned to each pixel and then averaging the angles [37].
2. The algorithm searches 0.8 nm perpendicular to each given pixel. If a neighboring fringe is found, the script checks if the angle between the fringes is less than 10 degrees.
3. If both criteria are met, the fringe pair is stored.
4. After running the algorithm for the entire region of interest (ROI), as long as two fringes are paired over 0.20 nm of fringe length, the fringes are considered stacked. If the fringes do not satisfy the conditions, they are recorded as non-stacked.

The 0.20 nm threshold for stacked fringes is a free tuning parameter; a parameter test was performed where the 0.20 nm threshold is systematically reduced down to one pixel (~0.02 nm). Figure 4.2 and Figure 6.11 shows the effect of the threshold value on the PSF for ethylene for different fuel dilutions. Reducing the threshold from 0.20 nm to 0.02 nm increases the total PSF by 45% to 55%, though the overall trends in soot nanostructure remain similar for all threshold values. We choose to use the 0.20 nm threshold since the selectivity of erroneous stacked fringes decreases as the parallel threshold increases to 0.20 nm, see Figure 6.11. Reducing the parallel threshold to one pixel gives a PSF of 77% to 88%, similar to values for mature soot in previous reports that reported 70% to 75% PSF [71].

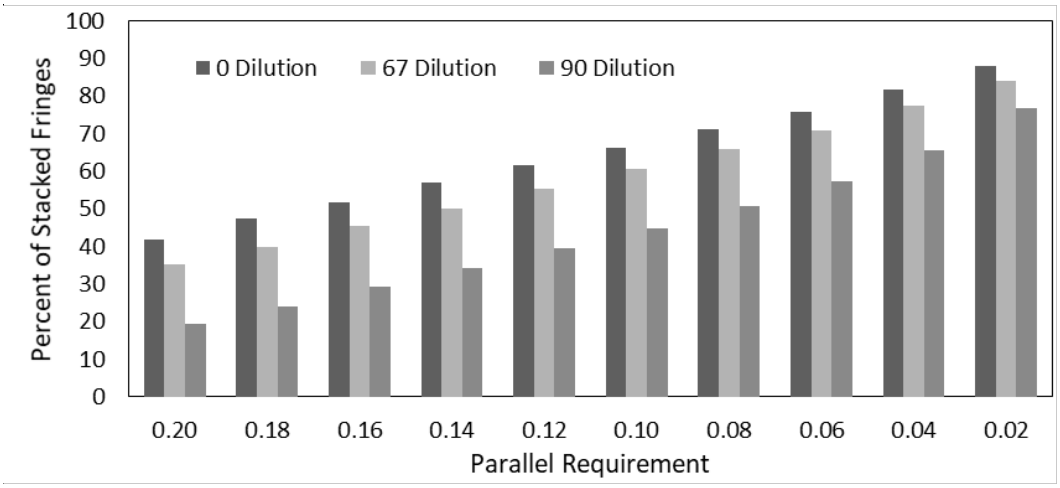

Figure 4.2. Parameter study to determine the effect of parallel threshold length on the PSF. Increasing the threshold from one pixel (0.02 nm) to 0.20 nm decreases the absolute PSF value linearly. Results are from 13 images of C_2H_4 soot from Figure 6.11.

The average separation distance between two stacked fringes is related to lattice spacing. For a graphitic crystal, lattice spacing is 0.335 nm [82], the spacing of coronene stacks in soot particles have been reported in the range of 0.35 nm to 0.40 nm [83]. In our initial analysis, the maximum lattice spacing was limited to 0.6 nm, similar to previous reports [15, 84]. However, as shown in Figure 4.3, a secondary peak exists beyond the 0.6nm threshold. This second peak skews the lattice spacing distribution to the right [83, 85]. The second peak is attributed to the stacking of multiple planes in the crystal structure. Fitting the lattice spacing histogram with two Gaussian PDFs reduces the influence of multiple stacked planes on the reported lattice spacing parameters. Here we report the lattice spacing at the center of the first peak.

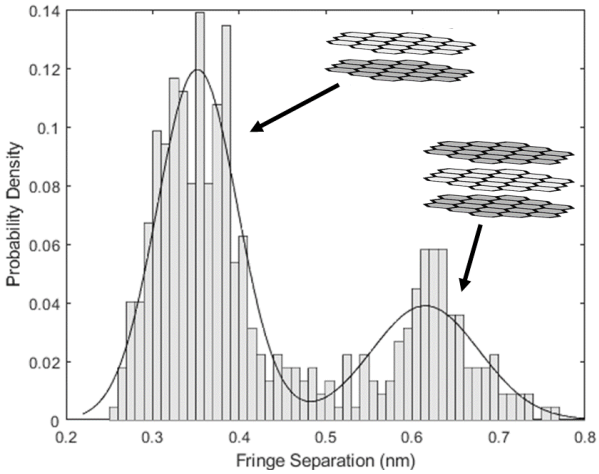

Figure 4.3. Fringe spacing distribution for the zero dilution ethane flame. A secondary peak indicated multiple stacked layers. When the stacking distance threshold is > 0.60 nm, a second peak appears within the set fringe separation measurements. The height of the second peak is 10% to 30% of the primary peak.

4.2.4 *Elemental and organic carbon analysis*

The C/H ratio of soot changes during carbonization [86], i.e., a higher elemental carbon (EC) fraction correlates with mature soot. To examine this behavior in the IGFR, the soot samples collected on the filter were analyzed for EC and organic carbon (OC) content for each fuel and multiple dilutions. The analysis was performed at Sunset Laboratory Inc. using a thermal, optical process (NIOSH 5040) [87].

4.3 RESULTS

4.3.1 *Flame temperature and soot composition*

Figure 4.4 shows the flame front temperature corresponding to the highest flame luminosity (T^*) for methane, ethylene, and ethane flames as a function of fuel dilution with Ar. As discussed in

section 4.2.2, T^* ranges for the zero and intermediate dilution flames are likely to be higher than the actual soot temperature due to the high-temperature gradient in the flame front. In the highest dilution ethylene and ethane flames, T^* is measured at the flame tip and is a good indicator of the maximum soot temperature. At the highest dilutions, T^* is measured as 1500K-15400 K for ethylene and 1495K-1568 K for ethane. The soot produced in the closed-tip flames travels through the tip instead of exiting from the wing as in the lower dilution cases. The temperature range presented here represents uncertainty in the axial flame location[88]. For nearly all flames, the maximum soot luminosity region was observed in close proximity to the temperature measurement location in the radial direction. However, for high dilution methane flames, the highest soot radiation region shifts away from the flame front. Among analyzed samples, the 67% dilution methane case is the only flame that exhibits a 1.8 mm wide blue sheath on the perimeter of the flame. Previous reports on methane-air diffusion flame also indicate that the temperature from the wing to the maximum soot volume fraction at a given height can decrease 150K–300K [79, 80]. In this work, the thermocouple measurements did not allow for accurate radial temperature resolution, thus we incorporated a 200K radial correction for the 67% diluted methane case yielding a T* = 1509K–1637K. The temperature at the tip of the 67% methane flame ranges from 1590K to 1489K (52mm to 61mm below the fuel nozzle), similar to the temperature range from the radial correction. Thus the maximum soot carbonization region temperature is in the 1509K-1637K, as shown in Figure 4.4. The radial correction for other flames is not required as they do not exhibit a blue sheath.

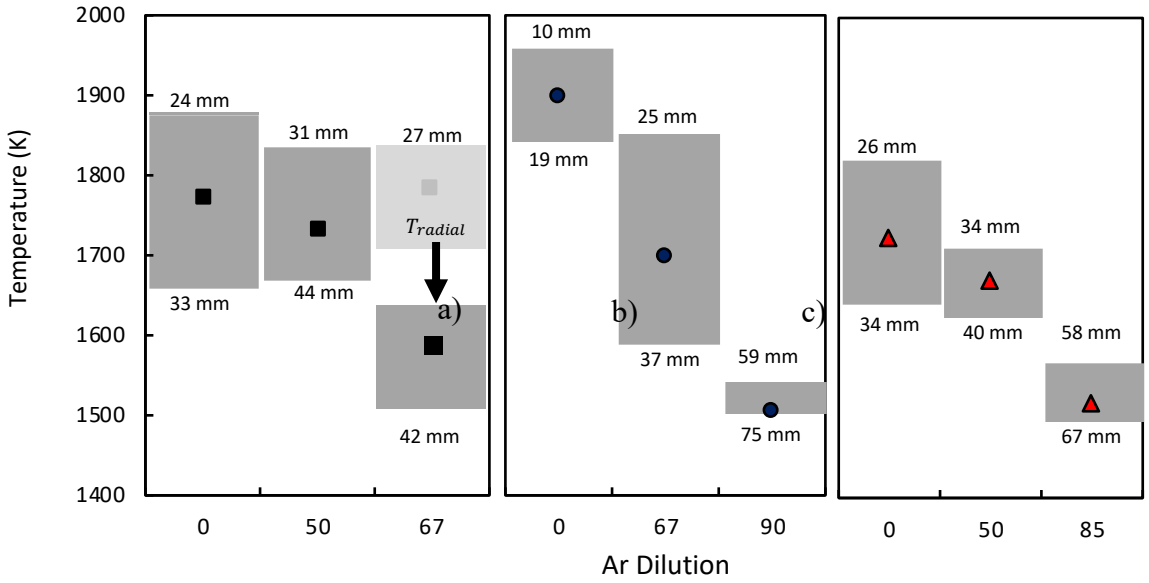

Figure 4.4. Highest soot luminosity flame temperature for a) methane, b) ethylene, and c) ethane for different fuel dilution ratios. The points correspond to the highest luminosity and the ranges correspond to the range of the axial location with the high flame radiation below the fuel nozzle. In the highest dilution methane flame, the T* requires a radial temperature correction due to the blue flame front.

Figure 4.5 shows the soot OC measurements as a function of fuel dilution. The total OC fraction for non-diluted flames is 3.3% to 5.4%. This low OC content is expected for the particles with a mature core-shell structure [89]. Dilution increases the OC content of the methane and ethane samples to 28.8% and 26.1%, respectively. For the ethylene flame at 90% dilution, the OC content is measured at 12.1% of the total sample mass. The gradual increase in OC with dilution means either (i) soot maturation does not have a well-defined threshold and occurs over a range of conditions, or (ii) a soot formation shifts to the colder region of the flame, i.e., a higher fraction of soot is produced along the axis, away from the high-temperature flame wing (seen with developing flame tip). To test the latter, it is possible to operate the IGFR at higher dilutions (lower temperatures). However, these conditions do not yield a sufficient soot sample for EC/OC analysis

even after eight hours of collection. These flames are entirely blue and do not emit in the red region, suggesting that no carbonized soot is present in the flame.

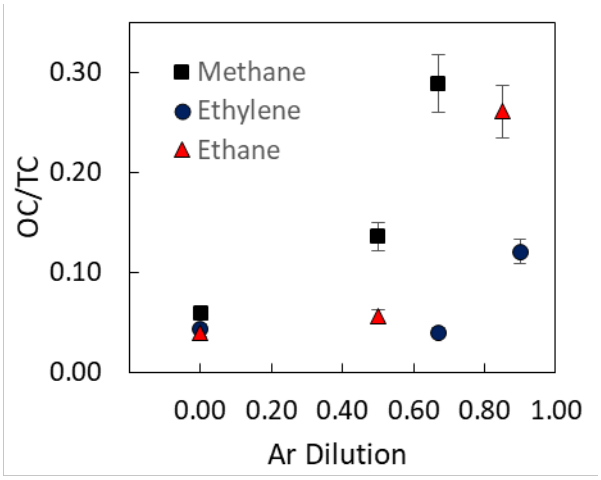

Figure 4.5. OC mass fraction in collected soot particles measured offsite shows an increase with dilution. The presence of OC indicates soot in the high dilution flames has not undergone carbonization.

4.3.2 *HRTEM- dilution influence on nanostructure*

Qualitative differences between soot from the low dilution and high dilution flames are apparent by the presence and absence of graphitic shells. Figure 4.6 shows that for all fuels, the flames without dilution produce soot aggregates with a structured shell surrounding cores ~5.0 nm in diameter. The core-shell structure is an indicator of a mature soot particle. Formation of these particles is associated with the IGFR flames that exhibit high radiation intensity on the flame wing, corresponding to the higher values of T^*.

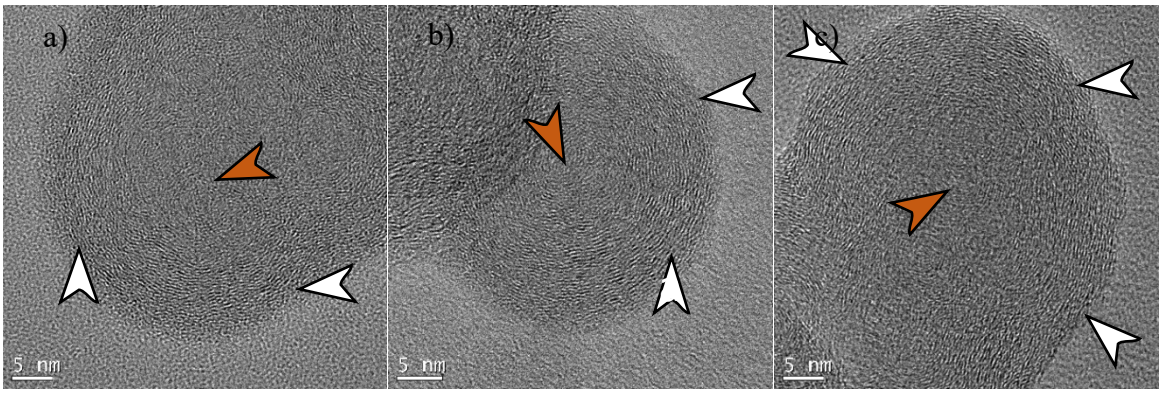

Figure 4.6. HRTEM images for no fuel dilution flames a) methane, b) ethylene, and c) ethane. All three fuels yield mature core-shell particle nanostructure. White arrows point to the shell on the periphery of the particles; colored arrows point to the unstructured core.

In the intermediate dilution flames, the graphitic shell is still present, see Figure 4.7. However, there are indications of reduced structure, such as larger core radii and the appearance of particles with multiple cores. These observations align with the OC measurements, showing that the soot at these intermediate dilutions has an increased OC fraction. In the intermediate dilution cases, T^* = 1624K-1851K. The GC-MS and EEM fluorescent analyses of the samples produced at these conditions do not show significantly different chemical composition from the zero dilution cases [90].

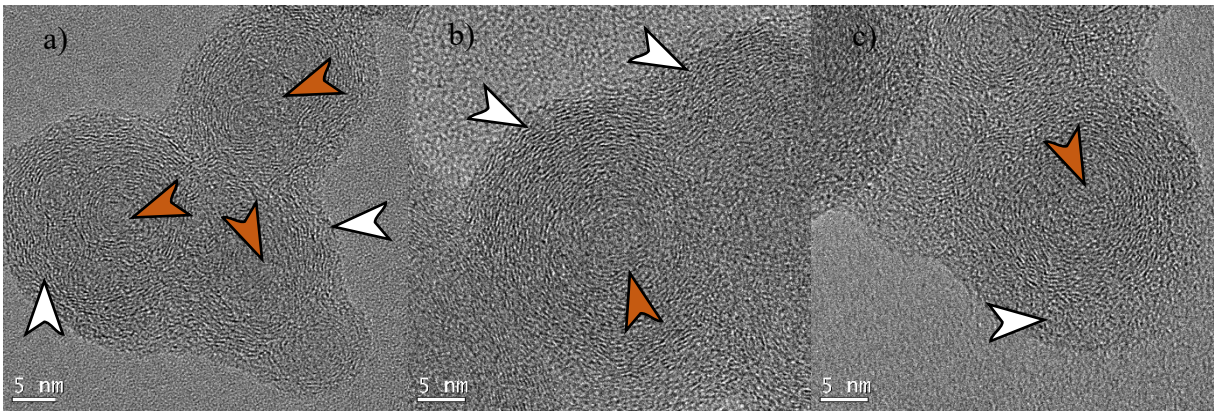

Figure 4.7. HRTEM images for intermediate dilution, a) methane – 50%, b) ethylene – 67%, and c) ethane – 50%. Particles have a structured graphitic shell. White arrows point to the shell on the periphery of the particles; colored arrows point to the unstructured core.

For the highest dilution flames, the core-shell structure is not present; the aggregates display two types of nanostructures. The first type is an isotropic particle shown in Figure 4.8 (a-c). These particles have a similar nanostructure to nascent soot particles before they reach the high-temperature flame front, i.e., prior to carbonization [91]. The observation also aligns with the aggregation formation mechanism proposed by Reilly et al. due to the presence of large young particles [76]. The second structure observed in the low-temperature ethylene and ethane flames show multiple internal cores ~5.0 nm in diameter, see Figure 4.8 (e, d). Similar structures have been observed in the high temperature, low residence time pyrolysis study in the absence of oxygen by Vander Wal and Tomasek, in which the structures were described as ‘curved’ nanostructures [55]. Reilly et al. have proposed that multiple nucleation sites form in the large “PAH-containing” particles [76]. In our experiments, the OC fraction of these samples is between 12% and 29% (see Figure 4.5). Additionally, the PAH analysis reported by Mahamuni et al. for the same set of samples shows that these low-temperature conditions yield soot particles with high concentrations of PAHs with molecular weights from 202-302 amu [90]. It is possible that the small spherical crystal sites represent an intermediate structure between the isotropic particle and the core-shell

structure aggregate. The spherical crystal sites nucleate inside a larger liquid-like particle (100 nm to 300 nm) and then facilitate the transition into the mature aggregates with core-shell particles that have an overall dimension similar to the parent particle, as shown later (see Figure 4.12). During the particle maturation, the amorphous particle shrinks, often forming internal voids (Figure 4.8e), due to the loss of the volatile species by pyrolysis. The remaining carbon organizes into the graphitic shells associated with mature core-shell structures.

Another possible explanation for the 5 nm domains is the oxidation of the young soot particles [92]. In our high dilution flames, the young soot aggregates reach the flame front, where they can be rapidly oxidized. Because the highest dilution flame has both a lower flame temperature and a closed tip, the young particles travel through an oxidative environment. The void shown in Figure 4.8e is similar to the proposed internal oxidation mechanism [93]. These smaller domains do not have an unstructured core pointing to the role of internal oxidation [94].

The T^* range that corresponds to the formation of these spherical crystal sites can be correlated to soot maturation thresholds. In our experiments, the T^* values associated with this transition are 1637K for methane, 1540K for ethylene, and 1568K for ethane. These temperatures agree with previously reported soot carbonization temperatures of 1495K [75] and >1523K [55]. However, the distinction of carbonization vs. formation of the initial crystal site in the parent aggregate is debatable as these samples contain up to 30% OC, indicating high amounts of bound hydrogen. Furthermore, in comparing these thresholds, one needs to recognize uncertainty in the thermocouple temperature measurements. As discussed above, the temperatures in this analysis correspond to the flame temperature in the vicinity of maximum radiation and not the soot temperature itself.

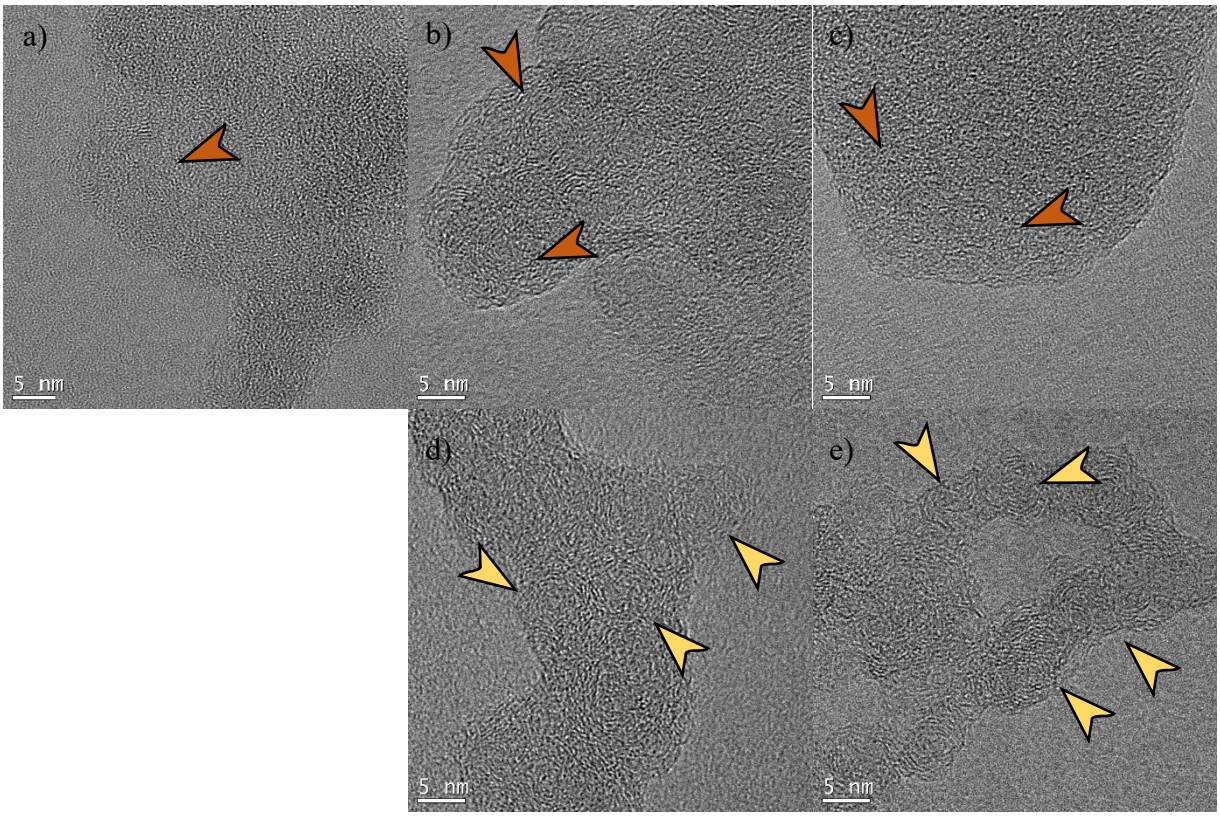

Figure 4.8. Highest dilution flames, a) methane – 67%, b) ethylene – 90%, and c) ethane flames – 85%, do not create a graphitic shell. Flame temperatures range from 1495 K to 1568 K. For ethane and ethylene, these flames also produce multi-core particles (core diameter ~5 nm) without shell structure for d) ethylene and e) ethane flames. Orange arrows point to the unstructured portions of the particles, the yellow arrows point to ~5 nm domains.

To verify that the shell formation is the result of temperature and not dilution, we performed limited experiments where the reagents entering the IGFR were preheated. The heating tape was wrapped around the inlet manifold and an inline thermocouple measured inlet air temperature. For the highest dilution condition for ethane (85%), the temperature of the fuel and air stream at the nozzle was measured at 498 K with an inline k type thermocouple [88]. The preheated ethane flame had higher radiation compared to the non-preheated flame at the same dilution. Figure 4.9 shows an HRTEM image; a core-shell structure is formed under the high dilution conditions, indicating the dominant role of T^* on soot maturation.

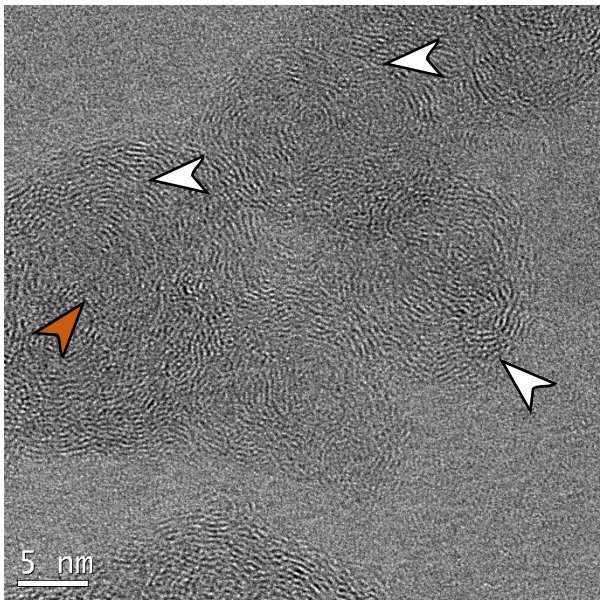

Figure 4.9. Ethane soot at 85% Ar dilution with 498 K inlet temperature. The preheat increases flame temperature, resulting in core-shell formation. White arrows point to the shell on the periphery of the particles; colored arrows point to the unstructured core.

Nanostructure measurements provide further insight into differences between the molecular components of the structured and unstructured soot particles. The complete set of HRTEM images used for analysis is given in Figure 6.12. Table 4.2. Average nanostructure measurements for nine flames from HRTEM image analysis. shows the mean nanostructure measurements for all dilutions; these follow the general trends. (1) For methane, ethylene, and ethane, at the highest dilution, the average fringe length decreases (compared to no-dilution cases) by 0.13 nm, 0.02 nm, and 0.11 nm, respectively. This decrease in fringe length agrees with reports that PAHs' conjugation length increases during carbonization [95]. (2) For methane, ethylene, and ethane, the mean tortuosity increases with dilution by 0.09, 0.04, and 0.05, respectively. Tortuosity is a representation of impurities in the graphene-like sheet, where five-membered rings or oxygen and

nitrogen interstitials increase the curvature of a molecule [81]. Higher temperature flames increase carbonization and produce PAHs with higher planarity. (3) For methane, ethylene, and ethane, the PSF decreases with dilution by 18.8%, 15.9%, and 16.5%, respectively. The gradual decrease in PSF and changes in OC fraction with dilution suggests that the soot maturation process does not occur instantaneously at a given threshold condition, but instead, carbonization is a complex process that occurs in the temperature range. In our experiment, the onset of carbonization temperature is ~1540 K for ethylene and ~1568K for ethane. Figure 4.10 shows that the OC content is well correlated with PSF measurements for all fuels tested.

Table 4.2. Average nanostructure measurements for nine flames from HRTEM image analysis.

	Methane No Dilution	Methane 50 Dilution	Methane 67 Dilution	Ethylene No Dilution	Ethylene 67 Dilution	Ethylene 90 Dilution	Ethane No Dilution	Ethane 50 Dilution	Ethane 85 Dilution
FL (nm)	0.98	0.90	0.85	0.91	0.90	0.89	0.99	0.89	0.88
Tortuosity	1.21	1.24	1.30	1.20	1.21	1.24	1.20	1.22	1.25
Highly Curved (%, T > 1.3)	14.8	20.1	32.9	13.3	13.8	19.7	10.8	16.3	22.7
Lattice Spacing (nm)	0.39	0.39	0.41	0.39	0.39	0.39	0.37	0.38	0.40
PSF (%)	37.2	26.3	18.4	41.7	34.0	25.8	40.6	31.0	24.1
Aromatic rings	25	21	17	22	21	21	29	22	19
Optical Band gap (eV)	1.70	1.80	1.94	1.79	1.80	1.81	1.63	1.78	1.86
Processed Images #	5	3	4	4	6	7	3	4	6

The lattice spacing is in the range of 0.37 nm and 0.41 nm, for both young and mature soot, which is similar to previous reports (range between 0.38 nm and 0.40 nm) [96]. Though some previous literature suggests that young soot particles have larger lattice spacing [78, 91, 97], in our analysis, we find only minor differences in the lattice spacing between the young and mature soot, i.e., for ethane combustion, the lattice spacing is 0.39 nm for mature soot and 0.41 nm for young soot, see Table 4.2. Note that in this study we have optimized the lattice spacing measurement technique by

including a larger parameter space and automating the process. The constant lattice spacing, regardless of flame temperature, suggests that graphitic layer assembly in the young and mature particles is similar.

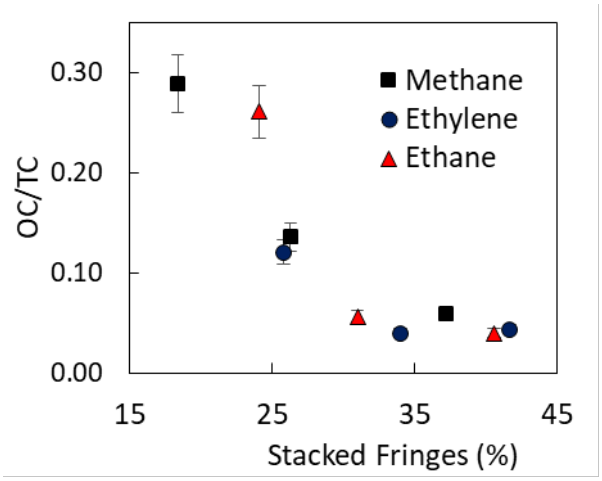

Figure 4.10. Organic carbon content as a function of the PSF in young and mature particles. Soot nanostructure is a good indicator of OC independent of fuel.

Figure 4.11 splits up the stacked portions of each sample and the non-stacked portions of each sample by fringe length and tortuosity. Regardless of flame temperature, structured fringes of particles are similar. For all fuels and dilutions, the stacked fringes are on average 0.3 nm longer and have a tortuosity value 0.05 lower, suggesting that an increase in planarity and a higher number of π orbitals are conducive to fringe stacking. The higher temperatures enable this transition via hydrogen atom abstraction as indicated by lower OC fraction.

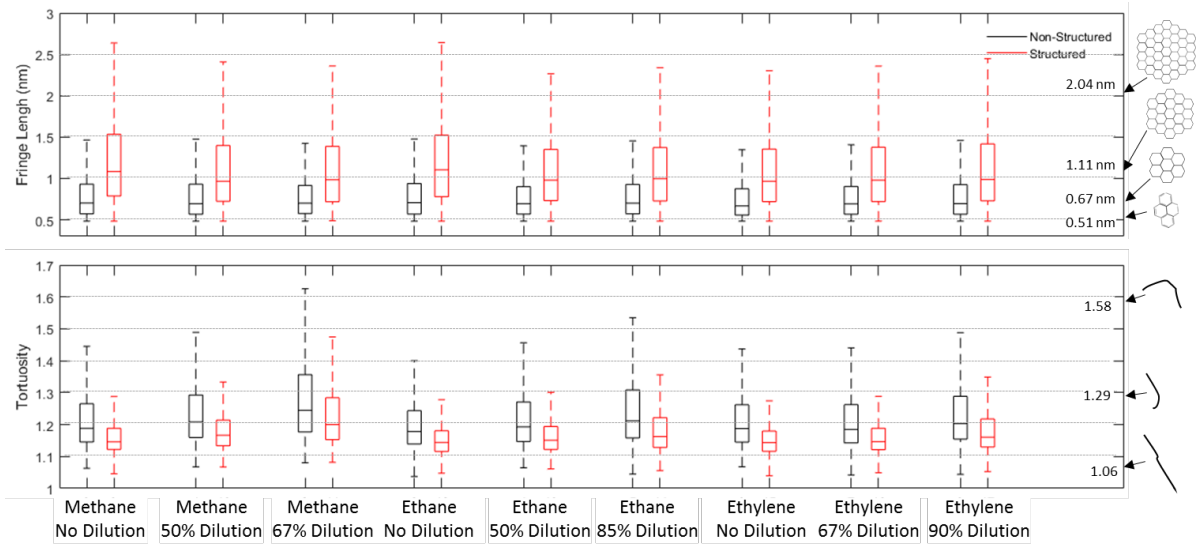

Figure 4.11. Fringe length and tortuosity for diluted methane, ethylene, and ethane flames. Red boxes represent stacked fringes and black boxes represent non-stacked fringes. Regardless of fuel, stacked fringes are longer and have a lower tortuosity in comparison to non-stacked fringes.

4.3.3 *Electron beam interactions*

For each fuel, the highest dilution case increased sample reactivity with the electron beam, likely due to beam-induced polymerization. Additional considerations in the analysis of high dilution samples were necessary, i.e., reducing the beam intensity avoided a foggy appearance of the image from sample-beam interaction. We conducted 20-minute tests, capturing an image every two minutes, for the highest dilution ethylene sample (isotropic particle). As seen in Figure 6.13, we observed discernable changes in the particle nanostructure, such as the formation of long fringes and stacking on the outer portion of the particles. The electron beam can induce a structural change that is only apparent in the high dilution cases that produce isotropic particles. To minimize electron beam influence, images are captured as soon as the particle is in-focus. All images are taken within the first 10 minutes of sample exposure to the electron beam. Here, three to seven HRTEM images for each sampling condition were analyzed to reduce uncertainty.

4.3.4 *Optical gap analysis*

HRTEM measurements are used to approximate the optical band gap (E_g^{opt}). A greater conjugation length of organic materials decreases the energy difference between the HOMO and LUMO bands; therefore, larger aromatics have a smaller E_g^{opt} [54]. Previous work has approximated the E_g^{opt} of soot particles using Tauc analysis of PAHs between 4-24 rings [54, 98] using the linear relationship:

$$\mathrm{E_g^{opt}} = \frac{5.8076}{\sqrt{\mathrm{M}}} + 0.5413 \tag{4.2}$$

where M is the number of aromatic rings approximated as $\frac{\sqrt{M}}{5.8076} \approx \frac{FL}{1.4787}$. The E_g^{opt} given in Table 4.2 is larger for less structured particles by 0.24 eV to 0.02 eV. This preliminary result needs further investigation, given that computational modeling suggests that E_g^{opt} varies significantly for similar-sized PAHs that comprise soot particles [99].

4.4 SOOT MATURITY AND SHELL FORMATION DISCUSSION

Reilly et al. observed that large young soot particles (~500 nm) exist in the fuel-rich regions of the flame [76]. Their overall dimensions of carbonized aggregates were also in the same size range. The authors proposed that during carbonization, small crystal sites formed inside of young soot particles. These sites increase the fractal character of the soot particles and form the aggregate structure with multiple core-shell sites where the overall dimensions of the mature fractal aggregates are similar to the parent particle [75, 76]. Evidence for this transition was based on particle size and PAH composition; the nanostructures of these particles were not reported. In this study, we analyze the internal particle structure transition over the range of flame temperatures.

The analysis includes measurements of tortuosity, fringe length, PSF, and OC fraction to characterize the soot maturation mechanism.

Figure 4.12 illustrates the different stages of particle maturity before and after carbonization. The young soot particle at 50kx magnification has dimensions of ~300 nm. The aggregate structure differs from the young soot particles described by Kholghy et al. [75], where a liquid particle with solid nuclei can spread on the surface due to impaction with the TEM grid and appear transparent compared to the solid nuclei. Young aggregates collected in our experiments are similar to young, irregularly shaped aggregates from post flame that have undergone some degree of carbonization, as reported by Blevins et al. [77] Unlike the mature aggregate with well-defined core-shell sites, the young particle does not have well-defined spherical primary particles [61, 75]. Furthermore, the 490kx magnification images of the young and mature soot reveal that the mature particle contains a core-shell structure while the young particle does not. These young particles exhibit two different structures: (i) large isotropic regions and (ii) large particles with multiple 5 nm domains. In the authors' opinion, these 5 nm domains are the developing crystal sites that indicate the incipient transition from non-structured (liquid-like particles) to mature soot aggregates by the internal nucleation route.

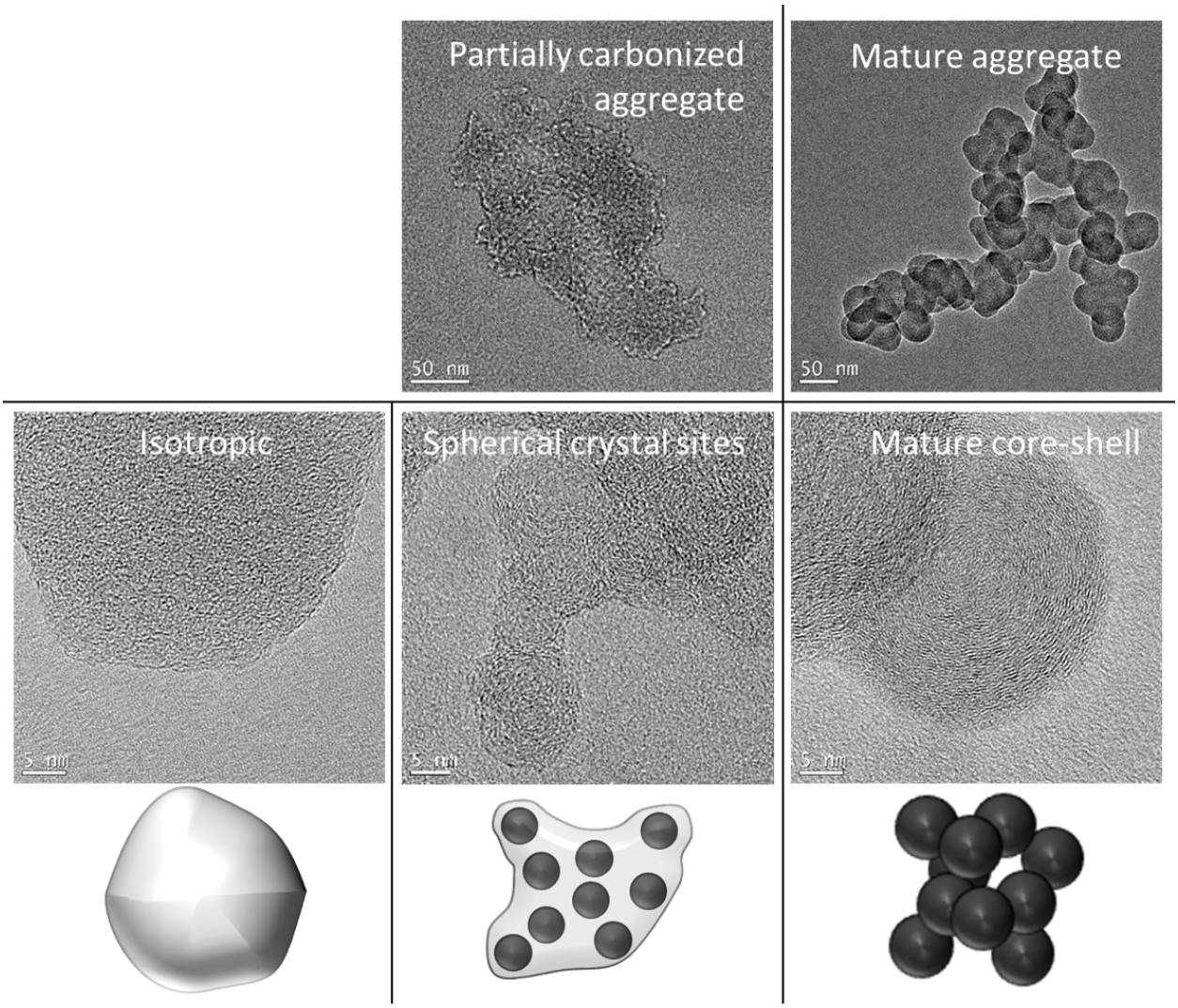

Figure 4.12. Evidence for the soot carbonization mechanism based on internal nucleation. The high dilution and lower temperature flames produce soot particles without a well-defined core-shell structure, shown at 50 kx magnification, similar to PAH-containing particles described by Reilly et al[76]. The soot particle exposed to high temperatures (right column) exhibits a mature soot aggregate structure. HRTEM images at 490kx magnification (middle row center) show the presence of 5 nm crystal nuclei inside of these low-temperature particles.

The most important factor in soot carbonization is the outgassing of hydrogen and other volatile species driven by pyrolysis or oxidation. Low-temperature combustion produces particles with high OC content [89]. The C/H ratio increases for higher flame temperatures. Reduction in the hydrogen content plays two key roles: (i) increases the number of π-π bonds and (ii) reduces PAH

curvature. Both effects increase PAH stacking by making the PAHs more polarizable and geometrically uniform; two PAHs with similar geometries are more likely to fit together than PAHs with dissimilar geometries. We observed lower stacking of curved PAHs for all fuels and dilutions, despite their higher dipole moment and the potential for the increased stacking of similarly-curved PAHs, see Figure 4.11 [81]. The higher planarity reduces steric hindrance and allows the PAHs to stack [100]. The range of transition temperature is measured to be at 1500K-1540K for ethylene and 1495K-1568K for ethane. In the methane experiments, the range of temperature is harder to determine due to the radial correction of the highest soot luminosity region; it was estimated to be 1509K-1637K, after a 200K radial correction. This radial correction can be 150K-300K [79, 80], which would change the estimate. The temperature range for all three fuels is in agreement with previous reports that have measured the transition temperature to be ~1495 K for liquid fuels [75] and >1523 K for unsaturated and aromatic fuels [55]. Higher temperatures or longer τ_{res} likely provides the energy required for the small domains to develop into the graphitic shells.

4.5 CONCLUSIONS

IGFR flames operated on three fuels with Ar dilution were used to generate combustion samples in flame temperatures from 1495K-1968K. At the highest dilution (lowest temperature) conditions, large young particles were observed exiting the flame for all three fuels. The nanostructure analysis using HRTEM images measured the graphitic fringe curvature, length, percent of stacked fringes, lattice spacing, and optical bandgap to characterize the soot maturation process. Along with a lower OC fraction, soot from higher temperature flames exhibit a mature fractal structure. Differences between flame conditions and soot properties are summarized as follows:

- Low-temperature flames: T_{max} ~1746K–1816 K, (T*~1495K–1637K), produce large amorphous particles with OC content 12.0 % to 29.0% wt., short fringe length ~0.85 nm to 0.89 nm, high fringe tortuosity 1.24 to 1.30, and low PSF 18.0 % to 25.8%.
- High-temperature flames: T_{max}~1946K-1968K (T*~1727 K-1960K), produce structured aggregates with OC content 2.8 % to 6.0% wt., long fringe length ~0.91 nm to 0.99 nm, low fringe tortuosity 1.20 to 1.21, and high PSF 37.2% to 41.7%.

The observation of crystal sites inside of young soot aggregates provides evidence for a single young soot particle maturating to a final fractal aggregate via the internal nucleation route. A decrease in PAH curvature and increase in PAH conjugation length at high T* allow PAHs to stack more efficiently to form graphitic structures, whereas highly curved PAHs need to find a similar geometric fringe to initiate stacking. The layer spacing in samples remained in the range of 0.37 nm - 0.41 nm, independent of flame conditions. The aggregate structure during the maturation process changes due to the outgassing or oxidation of hydrogen and/or volatile hydrogen-rich species indicated by an increase of the C/H ratio at the higher flame temperatures. The large young aggregate carbonizes by forming multiple structured 5 nm cores that grow into individual primary particles in the aggregate with core-shell structure. During the process, the unstructured particle reduces in volume, often forming the internal voids, as the particle loses mass due to pyrolysis or oxidation.

Though this work characterizes the temperature effect in simple laminar diffusion flames, generally, in any flame, the curved PAHs that form young soot particles will transition to graphitic structures forming mature soot aggregates, i.e., black carbon. In our experiment, the lower temperature samples also exhibit a brown color, which is characterized by high OC fraction, often found in low-temperature flames, such as biomass combustion due to the lower heating value of

the fuel (high moisture content) and the complex (endothermic) surface chemistry reaction. The increase in particle structure is the key to a reduction in particle reactivity, changes in particle optical properties, and reduction in the active sites on the soot surface. The current work can aid modeling efforts in soot formation, guide the design of combustion systems, and estimate environmental and health effects based on the reactivity of combustion generated particulate matter.

Chapter 5. ALTERNATIVE ANALYSIS OF SOOT GENERATED IN DILUTED FLAMES

5.1 OVERVIEW

To further characterize the soot produced in the Ar diluted diffusion flames presented in Chapter 4, several other analysis techniques have been explored as well. All analysis techniques use analogous samples to those described in Table 4.1. These analysis techniques include UV-Vis absorption measurements, Raman spectroscopy, and particle ROS activity. The work shows some interesting results. First, the low-temperature particles absorb stronger in the UV range, similar to BrC. However, the absorption is less than 300 nm whereas BrC absorption is commonly measured between 300 nm and 350 nm. Second, Raman analysis using a standard five-band deconvolution suggested by Sadezky et al. [101] is explored with non-definitive results. Instead, our work shows too much uncertainty to confirm an increase in amorphous carbon. The analysis is more reproducible using a four-band deconvolution. Third, the particulates produced in the low-temperature flames exhibit higher ROS generation and may be important in understanding the health effects of ambient PM.

Furthermore, we analyze the formation of a graphitic shell based on a theory developed from first principles. Hurt et al. [1] laid the foundation for the formation of a liquid crystal to mark soot maturity, and Kholghy et al. implemented this technique computationally [2]. However, HRTEM measurements do not align with the liquid crystal phase and, while the computational work is impressive and robust, our analyses suggest this theory needs to be further developed.

5.2 UV-VIS SPECTROSCOPY

5.2.1 *UV-Vis background*

To improve the understanding of carbonaceous aerosols' effect on human health and environment, the scientific community characterizes the PM emission by “color” of combustion generated aerosols; i.e., black carbon (BC) and brown carbon (BrC). Note that carbon produced for use in the industrial processes it referred as Carbon Black. The primary source of BC is combustion in the high-temperature environments, while BrC forms in low-temperature combustion as well from secondary organic aerosols (SOA) [102]. BrC is comprised of networks of hexanol carbon rings, along with aliphatic chains, five-membered rings, and oxygen and nitrogen interstitials [103]. These impurities increase particle reactivity and also changes UV absorption of PM [104]. Understanding the physicochemical properties of BrC and how they influence refractive index is critical to improving climate models [6]. The refractive index contains an imaginary component that characterizes light attenuation while the real component characterizes scattering.

5.2.2 *MeOH extract absorption and total EC/OC*

Soot samples are collected on PTFE filters with a 1.0 um pore size. Filters are weighted before and after collection using a microbalance to measure total PM mass, as shown in Figure 5.1. Filters are then submerged in 10 mL methanol (Sigma Aldrich, HPLC grade) and sonicated for 60 minutes. 3 mL of solution is pushed through a 0.2 μm syringe filter into a 4 ml cuvette. Extracts are measured using an Evolution 220 UV-Vis spectrophotometer from 200 nm to 750 nm. The baseline absorption is set using a cuvette containing pure solvent. Methanol is chosen as the solvent

because it extracts up 90% of OC from aerosols compared to water that only extracts down to 20% [105].

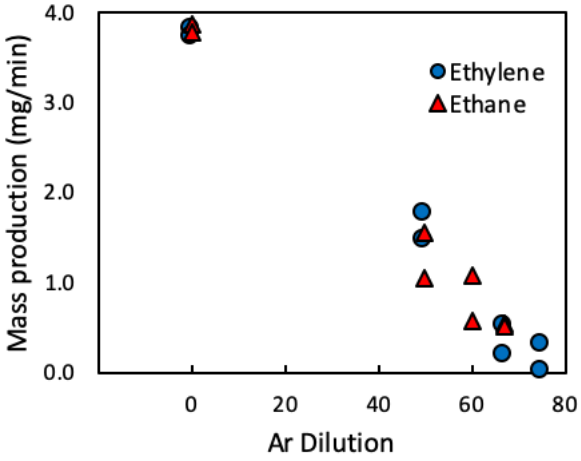

Figure 5.1. Mass production of soot for ethane and ethylene at different dilutions.

5.2.3 *UV-Vis spectroscopy*

The absorption of samples is defined as $A_\lambda = \log\left(\frac{I}{I_o}\right)$ where I_o is the incident intensity and I is the attenuated intensity. Previous reports have shown a stronger wavelength dependence on light attenuation in the UV region for BrC samples compared to BC [106]. The decrease in the UV attenuation is caused by a $\pi \rightarrow \pi^*$ transitions common in aromatics [107]. Figure 5.2 a, b show that the extract from lower temperature flames absorb stronger in the UV spectrum. Previous reports has measured BrC absorption in the 300-550 nm range [108].

The absorption coefficient (Abs_λ) at a given wavelength [109] is also analyzed as follows:

$$Abs_\lambda = (A_\lambda - A_{700})\frac{V_l}{l} \ln(10)$$

where V_l is the extract volume (3 ml), l is the cuvette depth, and A_{700} is a reference absorption at 700 nm. The higher dilutions show higher Abs_λ values compared to the lower dilution flames, as shown in Figure 5.2 c,d. However, the negative Abs_λ values due to an increase A_{700} is of concern. This increase suggests a possible contaminant in the sample or drift in the spectrophotometer. More analysis is needed to verify an increase in BrC for the high dilution flames.

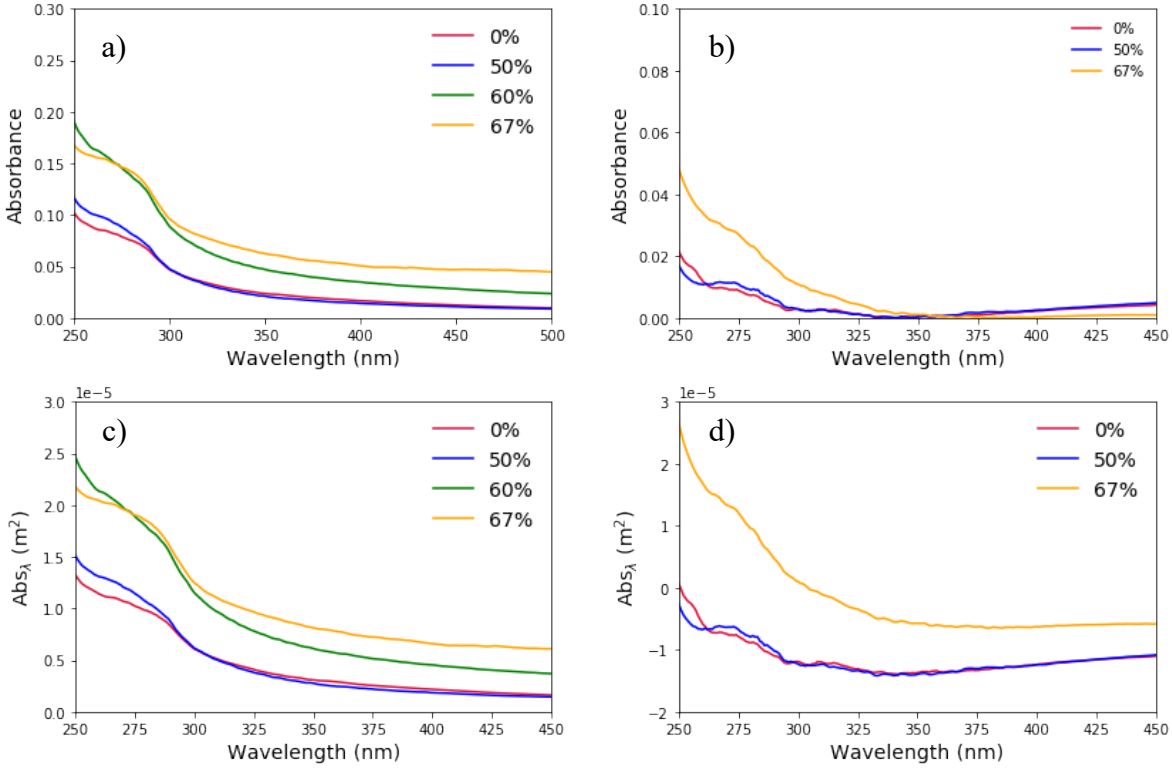

Figure 5.2. UV-Vis absorbance of methanol soluble extracts from the soot samples. Lower temperature flames absorb more in the UV region.

5.3 RAMAN SPECTROSCOPY ANALYSIS

5.3.1 *Raman background*

Raman spectroscopy is an inelastic scattering technique that is able to measure low frequency molecular transitions. Raman has been used to characterize amorphous carbon materials due to its sensitivity for both crystal and molecular structures [101].

5.3.2 *Experimental techniques*

Raman Spectra is collected using a 514 nm laser at 10% power (0.8 mW). Acquisition time was set at 30 seconds and three measurements were taken consecutively. The sum of three measurements was used to reach intensity counts over 1000. The laser did not visually degrade the samples and there is no observable difference between Raman spectra for the three consecutive acquisitions. Spectra are collected from three different positions for each sample to ensure reproducibility. Blank filter spectra were collected to ensure no signal from the filter overlaps with the sample spectra. Because the soot is black and absorbs the incident laser, a sample depth of a few microns on the filter is adequate to avoid filter signal contamination. For the highest dilution scenarios, only a small amount of soot is deposited on the filter, increasing fluorescence. The background signal is removed using a linear baseline subtraction.

5.3.3 *Raman deconvolution*

Raman spectra of all samples indicate two main bands, the D peak (1350 cm^{-1}) and G peak (1600 cm^{-1}), characteristic of black carbon [101]. These two bands are first deconvoluted using a five-band fit [101]. The location and significance of the five bands are given in Table 5.2, and a sample deconvolution is given in Figure 5.4a. The D3 band location was not reproducible using the five-band fit, which interfered with the spectra interpretation. Increasing the location of the D3 band increases overlap between the D3 peak and the G peak. Therefore, to improve D3 peak location reproducibility and measure the D3 peak signal, the G and the D2 were combined into a single G peak at 1600 cm^{-1} to create a four-band deconvolution method for the BC samples. Since the G peak and the D2 peak are due to graphitic and graphene edge effects, this method is deemed appropriate for measuring the amorphous content. An example of the four-band deconvolution is given in Figure 5.3b.

The deconvolution method uses the following protocols to reduce user influence on the fitting procedure. First, the raw spectra are fit as the position of each band is fixed. Second, the position of each band is allowed to float, and the raw spectra are fit again. Failure to initially fix the location of each peak cause significant changes in the D3 peak for a number of samples, where the D3 band can move to the center of the D1 peak around 1350 cm^{-1}.

Table 5.1. Raman spectra parameters for the five-band deconvolution method. The four-band deconvolution method combines the D2 and the G peak into one 'G' peak at 1600 cm^{-1}.

Band	**Raman Shift (cm^{-1})**	**Shape**	**Vibration Mode**
D1	1350	Lorentzian	Breathing of graphene rings, A_{1g} symmetry
D2	1620	Lorentzian	Graphene edge effects, E_{2g} symmetry
D3	1500	Gaussian	Amorphous
D4	1200	Lorentzian	sp2/sp3 carbon, polyene, A_{1g} symmetry
G	1580	Lorentzian	Ideal graphitic breathing modes, E_{2g} symmetry

a)

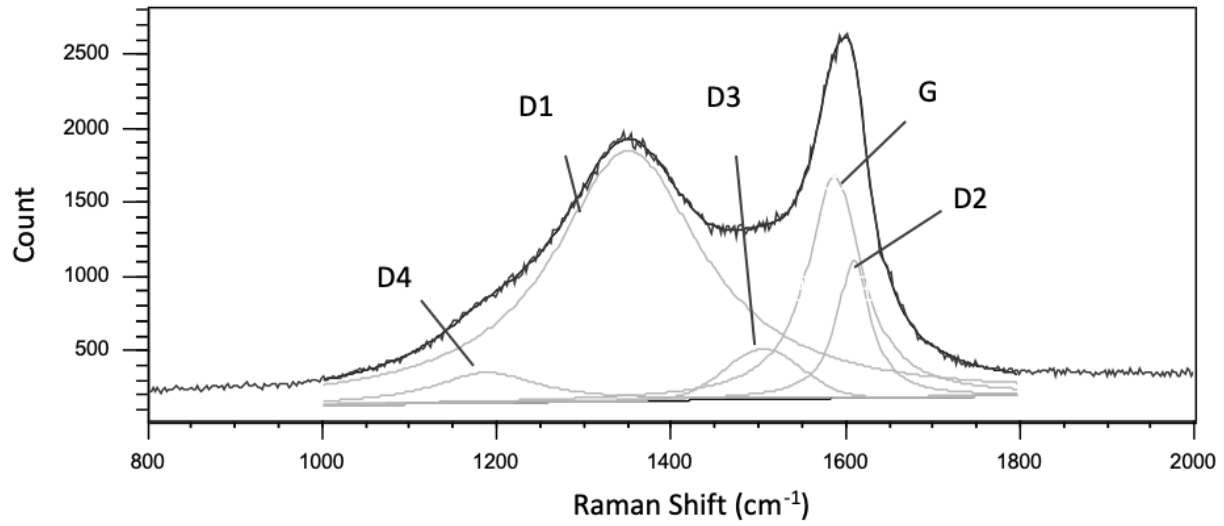

b)

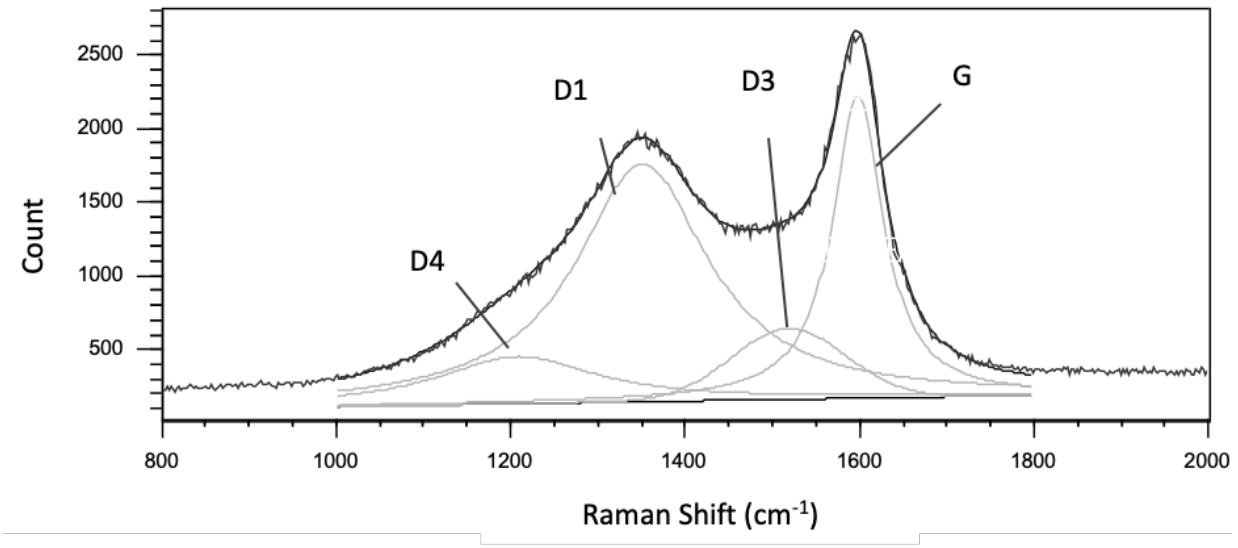

Figure 5.3. Raman spectra of soot produced from the zero dilution ethane flame a) The five-band deconvolution fits raw data from 1000:1800 cm^{-1} with a $\chi^2 = 0.879$ b) The four-band deconvolution fits raw data from 1000:1800 cm^{-1} with a $\chi^2 = 1.595$

Raman spectra for all cases give two peaks at 1350 cm^{-1} and 1600 cm^{-1}. These peaks correspond to the disorder content and the graphitic content of the soot particles. Several parameters are extracted from the Raman spectra deconvolution. R2 describes that amount of non-stacked graphene sheets in a given sample, previously reported to range between 0.5:0.8 [101] where:

$$R2 = \frac{ID_1}{ID_1+ID_2+I_G} \tag{5.3}$$

No standard in using area or intensity of the deconvolution methods are in the literature, but this analysis uses the area. For the four-band fit, ID_2 is not measured and R2 reduces to:

Table 5.2. Common signal interpretations from Raman spectra using the deconvolution methods. Three or more spectra are measured for each condition

	C2H4			C2H6		
Dilution	0.0	67.0	90	0.0	50.0	85
La (nm) five-band fit	5.94±2.52	4.81±0.99	5.31±0.75	4.49±1.86	2.63±1.65	9.90±2.21
La (nm) four-band fit	8.15±0.64	8.83±0.77	9.90±0.29	7.77±1.12	7.43±1.15	10.8±1.82
R2 five-band fit	0.65±0.03	0.67±0.02	0.66±0.01	0.69±0.02	0.74±0.01	0.57±0.03
R2 four-band fit	0.67±0.02	0.66±0.02	0.63±0.01	0.68±0.03	0.69±0.03	0.61±0.04

$$R2 = \frac{ID_1}{ID_1+I_G} \tag{5.4}$$

R2 values are in good agreement for both the five-band and the four-band deconvolution and within the commonly reported range. For the ethylene flame, there is no connection between dilution and R2 value. For the ethane flames, R2 increases at a medium dilution and then decreases at the highest dilution. There is no relationship to the gradual progression seen in HRTEM analysis.

Another indicator of the material structure is the ID_3 peak, commonly attributed to the amorphous content of soot particles. The area ratio of ID_3/IG is hypothesized to represents the overall graphitic content of the soot particles. However, for the five-band fit, the location of the D3 band is the primary indicator of D3 peak intensity, shown in Figure 5.4, regardless of flame temperature. The four-band deconvolution plays less of a role in Raman spectra shown in Figure 5.5. For both the five-band and the four-band deconvolution, ID3/IG decreases at the highest dilution (lowest temperature). Assuming amorphous content is proportional to the organic content and the percent of fringes that are not stacked, this result contradicts HRTEM analysis and EC/OC measurements. Because others have reported problems with characterizing amorphous content based on the ID3 peak as well [101], we assume the Raman Spectra is not an adequate technique to measure the amorphous content of black carbon.

A final interpretation of Raman spectra is approximating the graphitic crystallite size using the following [110] relationship:

$$L_a(nm) = 2.4x10^{-10}\lambda^4 \frac{A_G}{A_D} \quad (5.5)$$

The crystallite size values are given in Table 5.2. Crystalline size is approximated an order of magnitude larger than measured using HRTEM and show no relationship to flame temperature.

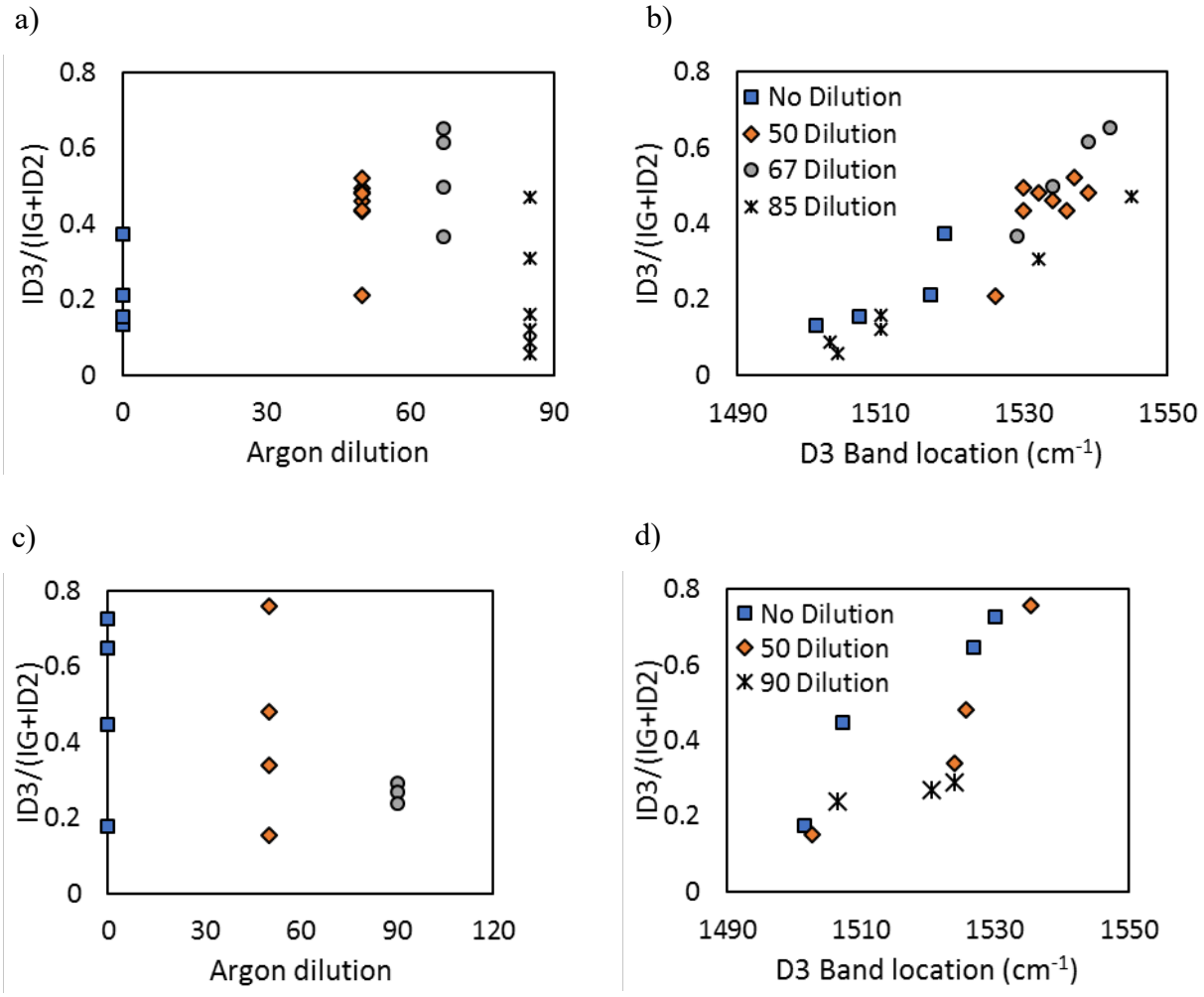

Figure 5.4. Standard five-band deconvolution of Raman spectra from ethane (a,b) and ethylene (c,d) flames. Shown in (a) and (c), dilution does not influence the D3 peak area. Shown in (b) and (d) the D3 band location is the major indicator of D3 band area.

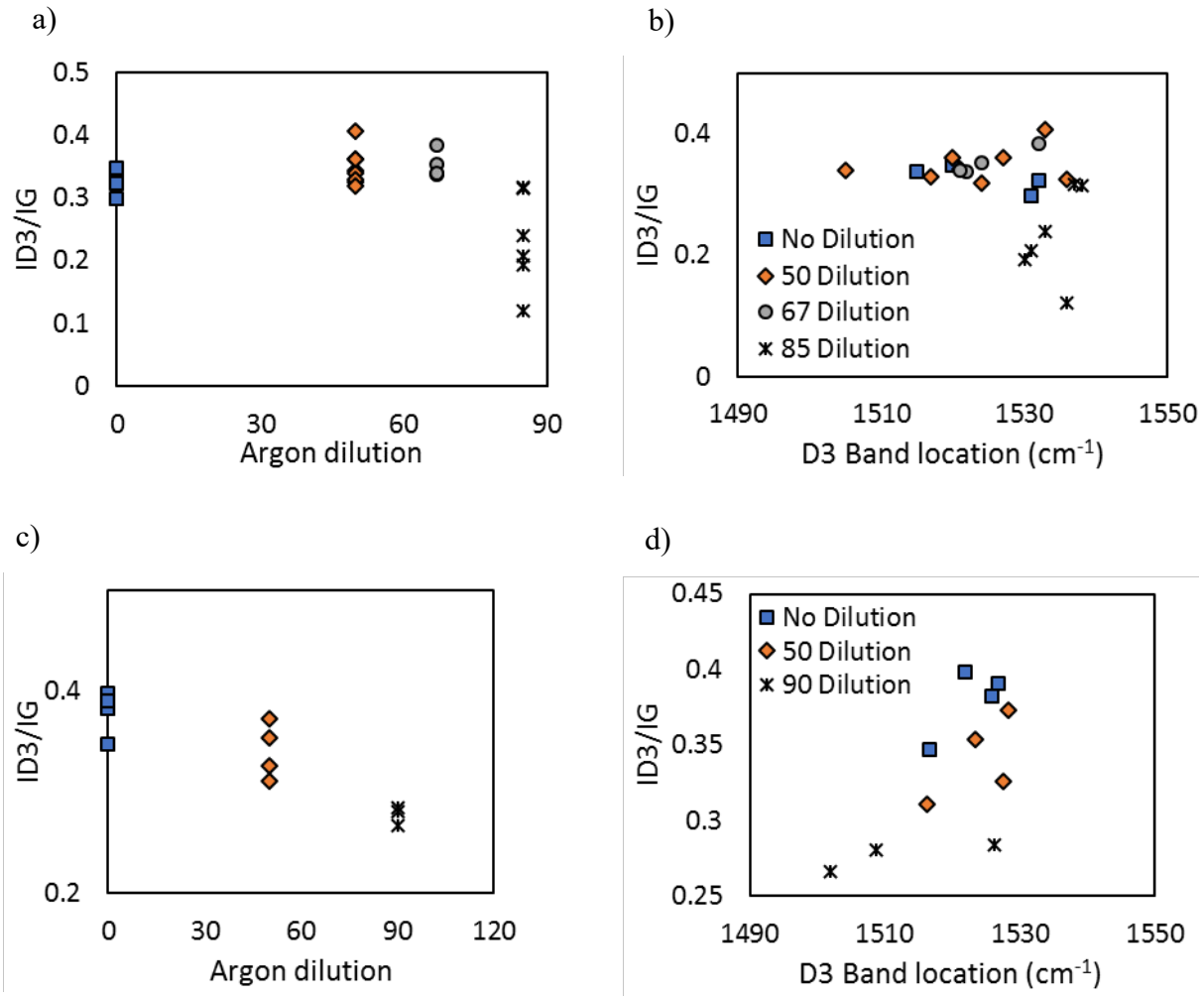

Figure 5.5. Four-band deconvolution of Raman spectra from ethane (a,b) and ethylene (c,d) flames. Combining the D2 and G band increases the reproducibility of the spectral analysis (a) and (c) The highest dilution decreases D3 area relative to the graphitic peak. (b) and (d) show the D3 band intensity is not strictly dependent on D3 band location.

5.3.4 *Raman conclusions*

Both a five-band and a four-band deconvolution are employed on soot samples produced in flames with various dilution ratios to lower flame temperature. From previous analysis on the diluted samples presented in this thesis, we expect the lower temperature flames to contain a higher fraction of amorphous carbon. However, the amorphous peak in the Raman peak is not

reproducible using the five band deconvolution due to a shift in location for the different peaks. Instead, the amorphous peak is more reproducible by combing the D2 and G peak and using a four-band deconvolution.

5.4 ROS GENERATION OF SOOT PRODUCED IN AR DILUTED ETHANE AND ETHYLENE FLAMES

5.4.1 *ROS background*

Health impacts of combustion generated particles can be assessed by characterizing the generation of reactive oxygen species (ROS) from PM [111]. Dithiothreitol (DTT) assays serve as a chemical marker in a controlled environment to predict biological toxicity. DTT assays effectively measure the production of ROS species from aromatics and transition metals, specifically Cu and Mn, and have been correlated with several biological endpoints. Humans use natural ROS in homeostatic functions, so either a depleted or increased level of ROS can be detrimental to human health. While proposed pathways behind oxidative stress have not been verified, aromatics and quinones are typically highlighted as ROS generating compounds.

5.4.2 *Experimental methods and reactive oxygen species*

The dithiothreitol (DTT) assay measures the presence or formation of ROS via formation of the DTT-disulfide [112]. Unreacted DTT is detected calorimetrically after reaction with 5,5'-dithiobis-(2-nitrobenzoic acid) (DTNB), producing 5-mercapto-2-nitrobenzoic acid. The rate of disappearance of DTT is proportional to the oxidant activity. The assay uses 1,8-phenanthraquinone as a positive control and methanol extracts of blank filters as a negative control.

We adapted the procedure of Li et al. [112] for use with a microplate reader to improve sample throughput, sensitivity and precision. PM samples on filters were extracted by ultrasonication in

methanol (7 mL) for 60 minutes. Following sonication, the filters were removed from the extracts and discarded. The samples were well mixed and 150 μL aliquots were removed for analysis. The extracts were concentrated to 2 mL under a flow of nitrogen at 50°C in a Turbovap evaporative concentrator and another 150 μL aliquot was removed for possible analysis if the unconcentrated extract showed low activity. The 2 mL extracts were then filtered through 0.2 μm PTFE syringe filters into new Turbovap tubes. The filtered extracts were reduced to dryness and reconstituted in 150 μL of methanol. After vortexing, water and phosphate buffer were also added to the samples. To measure DTT reactivity, the extracts were then incubated in the presence of DTT in a 96 well plate. At designated time points (0, 10, 20, 30, 40, 50 minutes) aliquots of the reaction mixture were withdrawn and added to microplate wells containing tris HCl in 20 mM EDTA and DTNB (5,5'-dithiobis-(2-nitrobenzoic acid)). Absorption at 412 nm was recorded. The rate of DTT consumption is calculated from a plot of absorbance vs. time, and this value is corrected for atmospheric oxidation of DTT calculated from a blank filter extract time series run with each microplate.

5.4.3 *ROS results*

BrC and OC have a higher DTT consumption rate compared to EC [112]. There appears to be elevated levels of ROS generation in the lower temperature flames for both the methanol soluble extracts and PM samples, as shown in Figure 5.6. For all fuels and dilutions, the non-filtered samples with the PM is more reactive. The particles themselves may be more reactive than any species condensed or adsorbed to the particle surface, or there are species that are not soluble in MeOH that generate ROS.

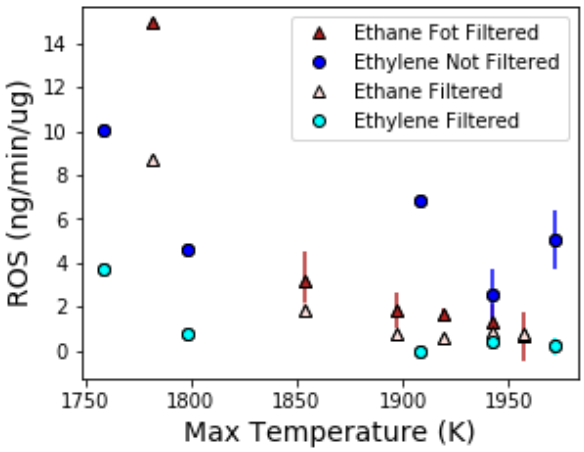

Figure 5.6. Decreasing maximum flame temperature increases ROS. The lower temperature flames produce particles with lower EC content.

The C/H ratio of soot changes during carbonization [86], i.e., a higher elemental carbon (EC) fraction correlates with mature soot. For each fuel, an increased ROS response is seen in elevated OC for both extract and non-extracted samples, as seen in Figure 5.7.

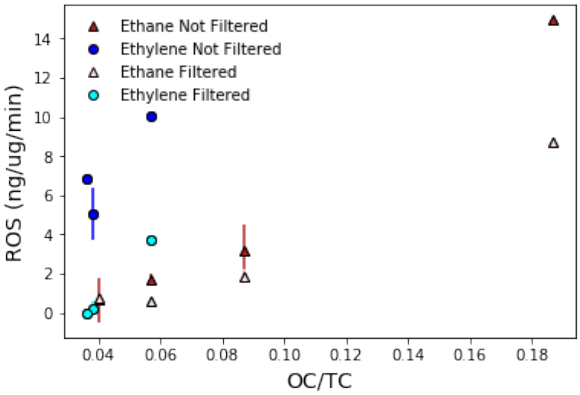

Figure 5.7. Comparison between organic carbon composition and a particle's propensity to generate ROS.

Samples were analyzed for PAH composition using GC/MS [113]. The results were used to estimate sample toxicity equivalency factor (TEF) which is a toxicity measurement normalized to

benzo[a]pyrene [114]. There appears to be a slight trend, where increasing ROS aligns with an increase in TEF.

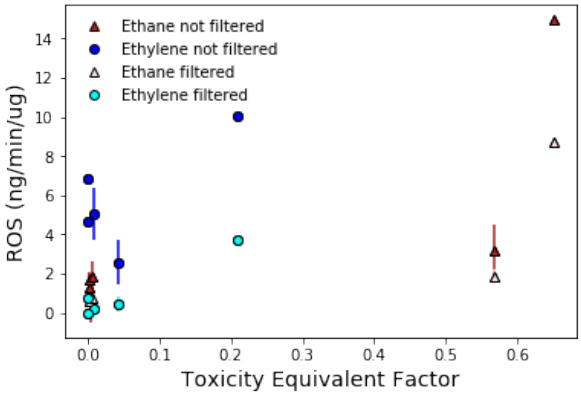

Figure 5.8. Comparison between TEF and ROS generation. Increasing ROS appears to have a slight impact on TEF measurements.

5.4.4 *ROS conclusions*

Soot particles produced in diluted laboratory flames have previously been shown to contain different structural properties. Here, the particles with different structural properties are analyzed to see how they influence particle reactivity and ROS generation. Soot produced in lower temperature flames can cause a more severe response by generating more ROS.

5.5 SOOT SHELL FORMATION

One possible explanation of soot particle shell formation is a transition from a physical to a chemical equilibrium [2]. As young soot particles evolve, the average MW of their PAHs increases [50]. It was proposed that the MW is roughly proportional to clearing temperature (T_C), the temperature at which a liquid crystal forms [1]. Once the particle's T_C is above the flame temperature, a nematic phase forms, which is itself the ordered graphitic shell. Further growth would then occur from agglomeration or by secondary growth via PAH condensation [37].

One benefit of the liquid crystal approach is it includes the physical confinements at the nanoscale. Splay forces lead to thermodynamic deviations from the bulk properties. The splay forces that can be modeled by the Frank elastic theory counteract the ordered phase that can be modeled by the second Legendre polynomial in the Maier-Saupe mean-field theory. The core radius, at the center of the mature soot particles, exists at a point where splay overcomes order Gibbs minimization, given as $r_{core} = \sqrt{\frac{2K_{11}}{\left(\frac{\rho}{MW}\right)\Delta G_{N/I}}}$ where K_{11} is an elastic crystal constant, ρ is the density, and $G_{N/I}$ is the molar free energy of the non-equilibrium phase transition from the unstrained ordered phase to the isotropic phase[1]. The core-shell structure of soot particles is commonly observed in HRTEM images, supporting this theory. Fringe length measurements in this study show that mature soot is comprised of PAHs that have a T_C below the flame temperature. For example, an upper limit for T_C is circumcircumcoronene that would measure a fringe length ~2.04 nm, twice the average fringe length of stacked fringes in this study. The T_C of circumcircumcoronene is estimated to be 1236 K. Based on experimental measurements, PAHs in the soot particles are not subcooled and cannot form crystal phase.

Chapter 6. SUPPLEMENTAL INFORMATION

6.1 METHANE SEM ANALYSIS AND RECIRCULATION VIDEO

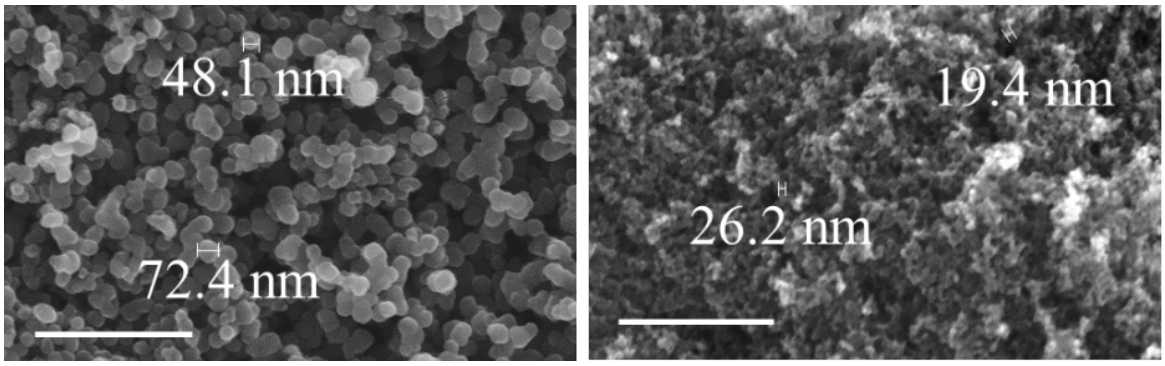

Figure 6.1. SEM images of soot produced in methane/air a) recirculating IGFR diffusion flames b) non-recirculating IGFR flames. The non-recirculating IGFR produces significantly smaller primary particles compared to the recirculating flame. The scale bar is 500 nm.

IMG-0926.MOV

Figure 6.2. Video of IGFR with recirculation. Particles are observed oscillating in the fuel rich region for an extended period of time.

6.2 NUMERICAL SIMULATIONS OF THE RECIRCULATING METHANE FLAME

The CFD simulations are performed in a 2D axisymmetric domain, as shown in Figure 6.3 (blue plane). The axisymmetric assumption is justified based on geometry on the burner and by the experimental observations of the flame. For all conditions, the flow is well behaved and only minor 3D instabilities in the recirculation zone were observed. The mesh is shown in Figure 6.4. The mesh is constructed of quadrilateral elements. The typical grid cell size is in the 0.1-0.2 micron range, the maximum aspect ratio of the cell is 4, the maximum cell size in the flame region is 0.2

micron. The flame front (region CO mole fraction >0.01) is resolved by at least 10 cells which was found to be sufficient in modeling laboratory and industrial combustion systems, e.g., [35, 115, 116].

The wall temperature is calculated based on the local heat transfer coefficient; the model includes conduction through the wall, free convection/radiation heat transfer is set for the outside wall. The walls are modeled as non-slip boundaries with scalable wall function [117]. The boundary layer is constrained so that the first grid point is located at a distance of $y^+ = 1$. Several combustion kinetic modeling options have been considered. A 3-step global mechanism [46] was used in the preliminary simulations to estimate the flow patterns and temperatures due to the fast convergence time, the mechanism limited to only the major combustion species and are, thus, not well suited for this study. A skeletal chemical mechanism of Karalus et al. [118] is used as a compromise between computational efficiency and the ability to provide detailed species concentration. The chemical mechanism contains 22 species and 122 reactions; it predicts similar flame characteristics as GRI 3.0 in premixed laboratory flames. However, when compared with a simulation using the full GRI 3.0, the skeletal mechanism predicted shorter flame length; likely due to a limited number of free radical species. The other benefit for using the detailed mechanism is its ability to directly compute the concentration of C2H2 that are used as a precursor for soot formation. In the CFD simulation, heat capacity, mass diffusivity, and viscosity are calculated using the mixing law approach. The species diffusion is modeled by multicomponent diffusion, and the thermal diffusion is modeled using kinetic theory. Table 6.1 and Table 6.2 summarize the boundary conditions and the numerical algorithm used in this study.

Table 6.1 CFD boundary condition summary.

Boundary	Type	Parameter
Fuel Inlet	Mass Flow	As in experiment, T=298K
Air Inlet	Mass Flow	As in experiment T=298K
Outlet	Pressure outlet	0 Pa gauge, flow direction – negative Y
Wall Quartz Tube	Heat transfer	Semitransparent media, emissivity=0.5. Convection, radiation, conduction modeled
Wall Quartz Tube	Flow	No-slip enhanced wall-function
Wall Fuel Tube	Heat transfer	*Fixed T=350K, as measured*
Wall Fuel Tube	Flow	No-slip enhanced wall-function

Table 6.2: Numerical methods.

Grid	2D axisymmetric
Number of cells	102 609, quadrilateral
Solver	Steady-state
Near-wall treatment	Scalable wall function
Buoyancy effects	Included,
Reaction model	Volumetric, stiff solver
Soot model	Formation precursors– C_2H_2, C_2H_4 Surface growth – HACA Coagulation - Smoluchowski's equation Aggregation - Method of moments based on bivariate PSD Oxidation – O_2 and OH Condensation – none
Diffusion model	Multicomponent
Gas Chemical Kinetics	GRI3.0 – NO_X chemistry is removed
Soot radiation model	Polydispersed particle-size distribution (PSD) with population balance equations (PBE) solved by the method of moments
Gas radiation model	Discrete Ordinates
Density	Ideal gas
Mass diffusivity	Kinetic theory
Thermal diffusivity	Kinetic theory
P-V Coupling	Coupled
Pressure	2nd order
Momentum	2nd order
Density	2nd order
Turbulence	2nd order
Species	2nd order
Energy	2nd order

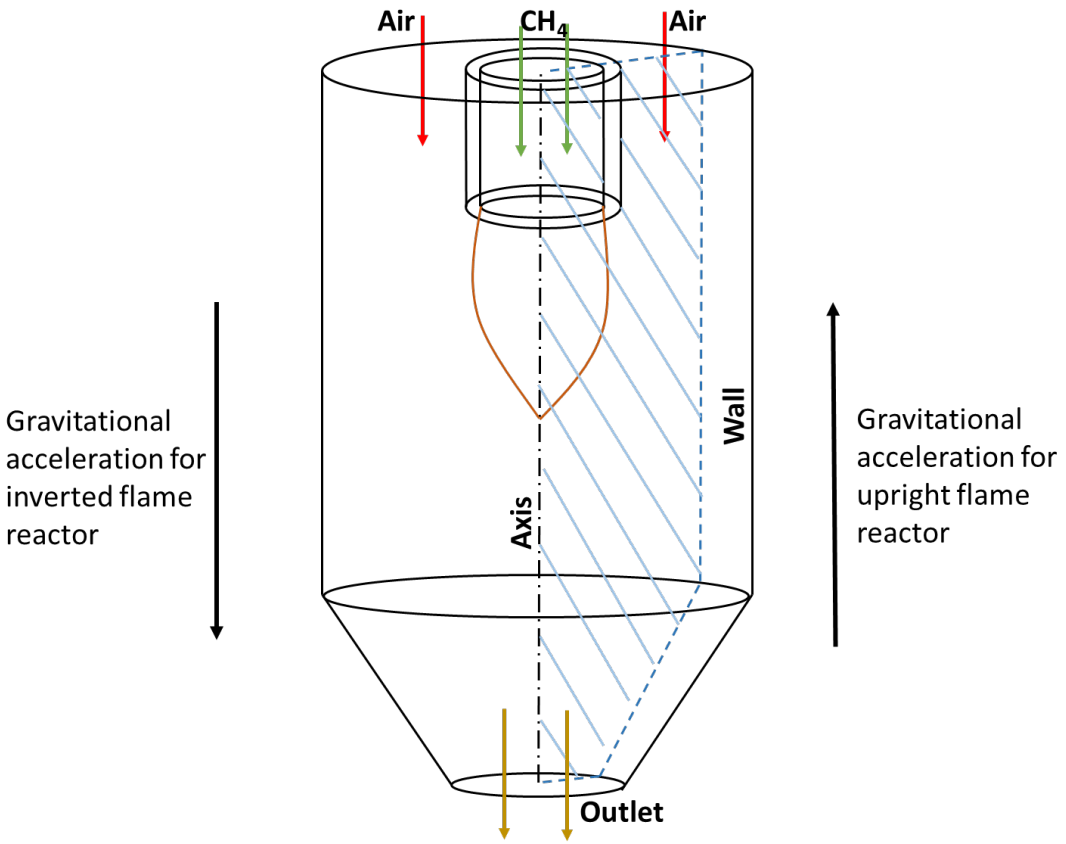

Figure 6.3. Geometry and boundary conditions. The 2D axis-symmetric domain is shown in blue.

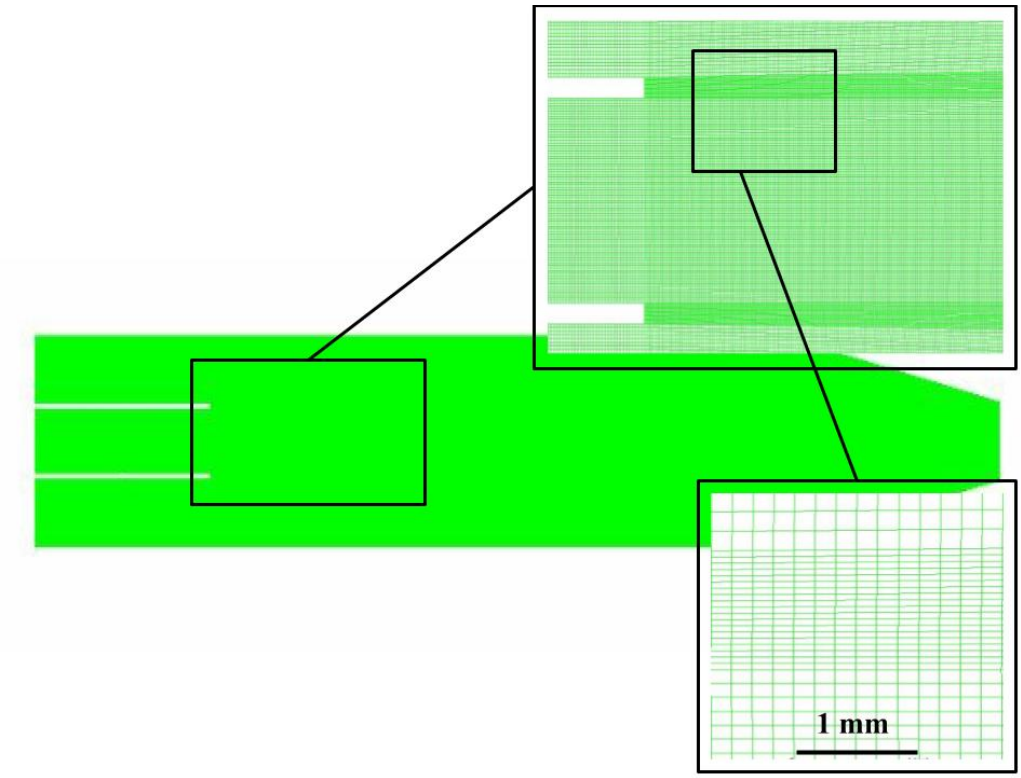

Figure 6.4. The computational mesh used in CFD. The mesh is reflected upon the axis.

Figure 6.5 shows H_2O, CO, and CO_2 mole fractions. The solid black line sorresponds to the stoichiometric conditions.

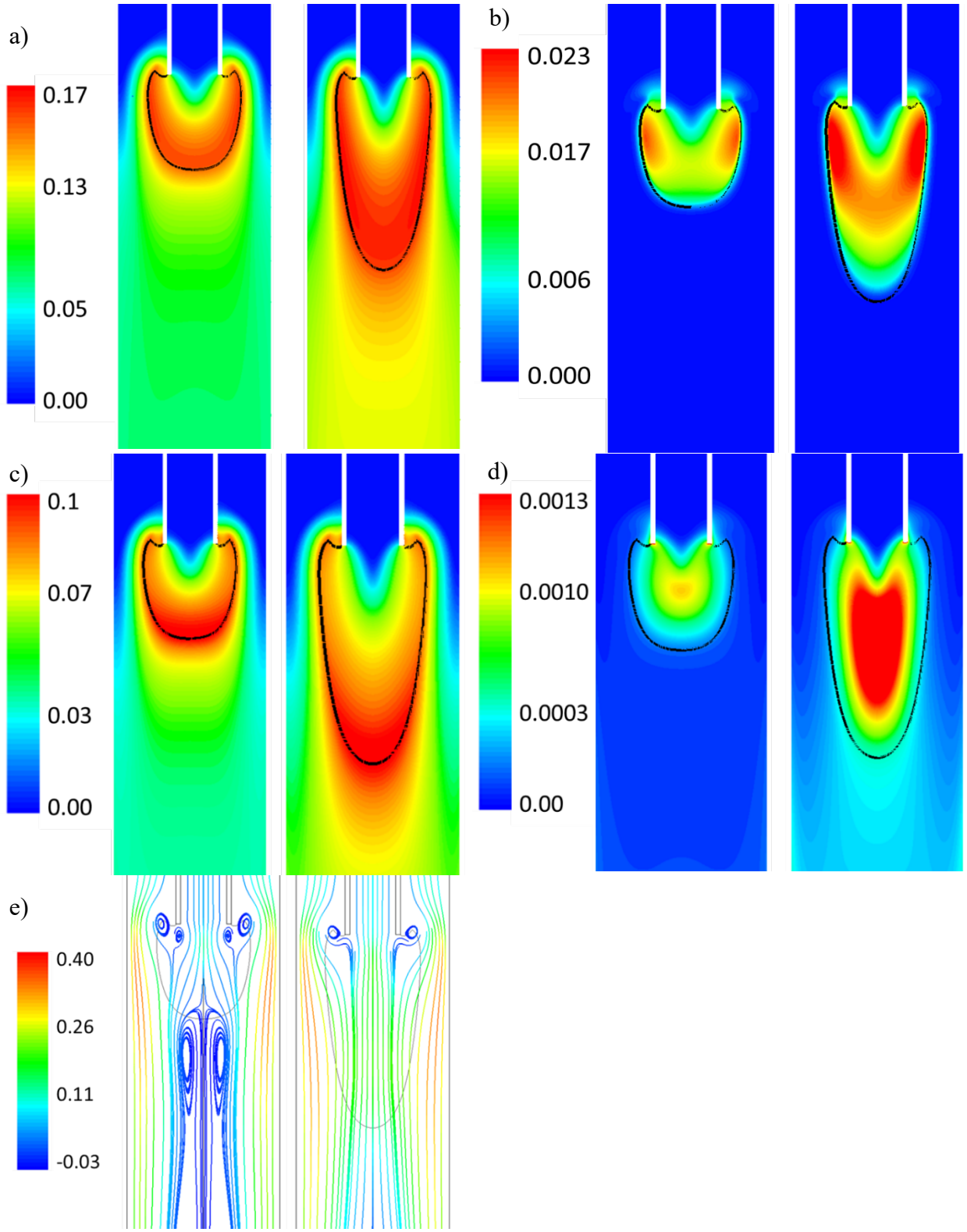

Figure 6.5. Contours and pathlines for IGFR simulations. A) H_2O mole fraction b) CO mole fraction c) CO_2 mole fraction d) soot density e) axial velocity (m/s)

6.3 CHEMICAL REACTOR NETWORK

Table 6.4 compares CFD and CRN in the flame front. Without changing operating conditions, the volume, temperature, and nitrogen align well for all three chemical mechanisms. This furthers the accuracy of the CRN.

Table 6.3: Computational results for CFD and CRN models for IGFR flames. Also, resulting soot growth species given by two chemical mechanisms.

	IGFR Recirculating Solution				IGFR Non- Recirculating Solution			
	CFD	CRN, mech [50]	CRN, mech [27]	CRN, mech (Wang et al. 2007)	CFD	CRN, mech [50]	CRN, mech [27]	CRN, mech (Wang et al. 2007)
Volume Flame Front (cm^3)	8.2	8.3	8.3	8.3	10.5	10.2	10.2	10.2
Temperature Growth Region (K)	1609	1603	1610	1608	1653	1664	1667	1664
τ_{res} (sec)		63	63	63		80	80	80
X_{C2H2}		2.6E-7	1.3E-5	4.4E-7		6.7E-8	1.1E-6	6.6E-8
X_{N2}	0.73	0.71	0.71	0.71	0.73	0.73	0.73	0.73
X_{CH4}		3.1E-5	3.7E-5	3.4E-5		1.7E-5	2.0E-5	1.6E-5
X_{OH}		9.6E-4	9.0E-4	9.4E-4		1.2E-3	1.1E-3	1.3E-3
X_{CO}		4.7E-3	4.E-3	4.4E-3		6.7E-4	5.6E-4	7.2E-4

6.4 ETHYLENE FLAME EXPERIMENTS TO MEASURE PRIMARY PARTICLE DIAMETER

In addition to methane, ethylene experiments are performed to determine the primary particle size distribution in the recirculating flame. The experimental setup uses the same IGFR as the methane flame. However, for the non-recirculating case, the reactor is oriented in the +g direction. Experimental flow rates are given in Table 6.4. Previously, C_2H_4 soot has been reported to have a maximum d_p of 38 nm [56, 119, 120]. We measure d_p from the upright flame to be 33 ± 4 nm, in agreement with previous work. In the recirculating IGFR C_2H_4 flame, the primary particle diameter is 54 ± 8 nm, comparable to the recirculating methane flame. Size distributions are given in Figure

6.6. The recirculating d_p distribution appears to have similar bimodal distribution as the methane particles measured with TEM.

Table 6.4. Experimental setup and flow rates for ethylene diffusion flames.

	Non-Recirculating	Recirculating
C_2H_4 flow rate (slpm)	0.10	0.10
Air flow rate (slpm)	3.7	3.7
Reactor orientation	Upright	Inverted

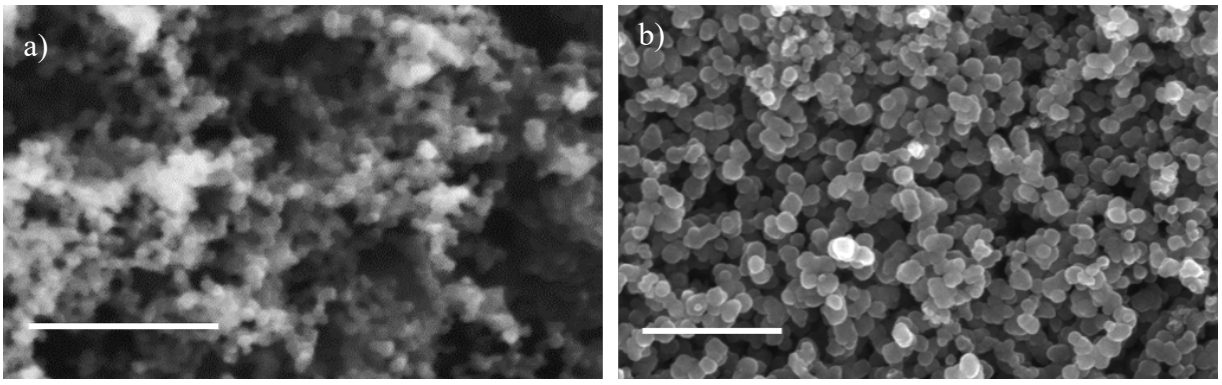

Figure 6.6. SEM images of soot produced in ethylene/air a) upright and b) recirculating IGFR diffusion flames. The scale bar is 500 nm.

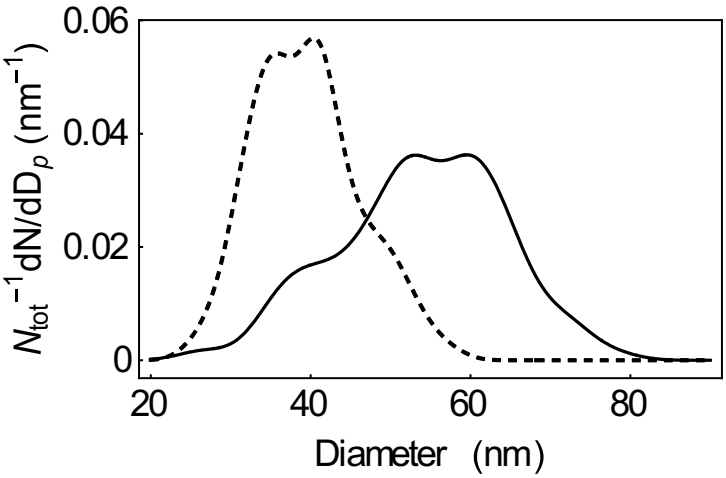

Figure 6.7. Primary particle size distribution for C_2H_4/air diffusion flames. The dashed line represents the upright flame; the solid line represents the recirculating IGFR. The recirculating flame has a larger diameter than the upright flame, following the same trend as CH_4/air diffusion flames. The presence of two peaks in the recirculating size distribution is likely to come from particles outside of the recirculating pattern due to the high sooting propensity of ethylene.

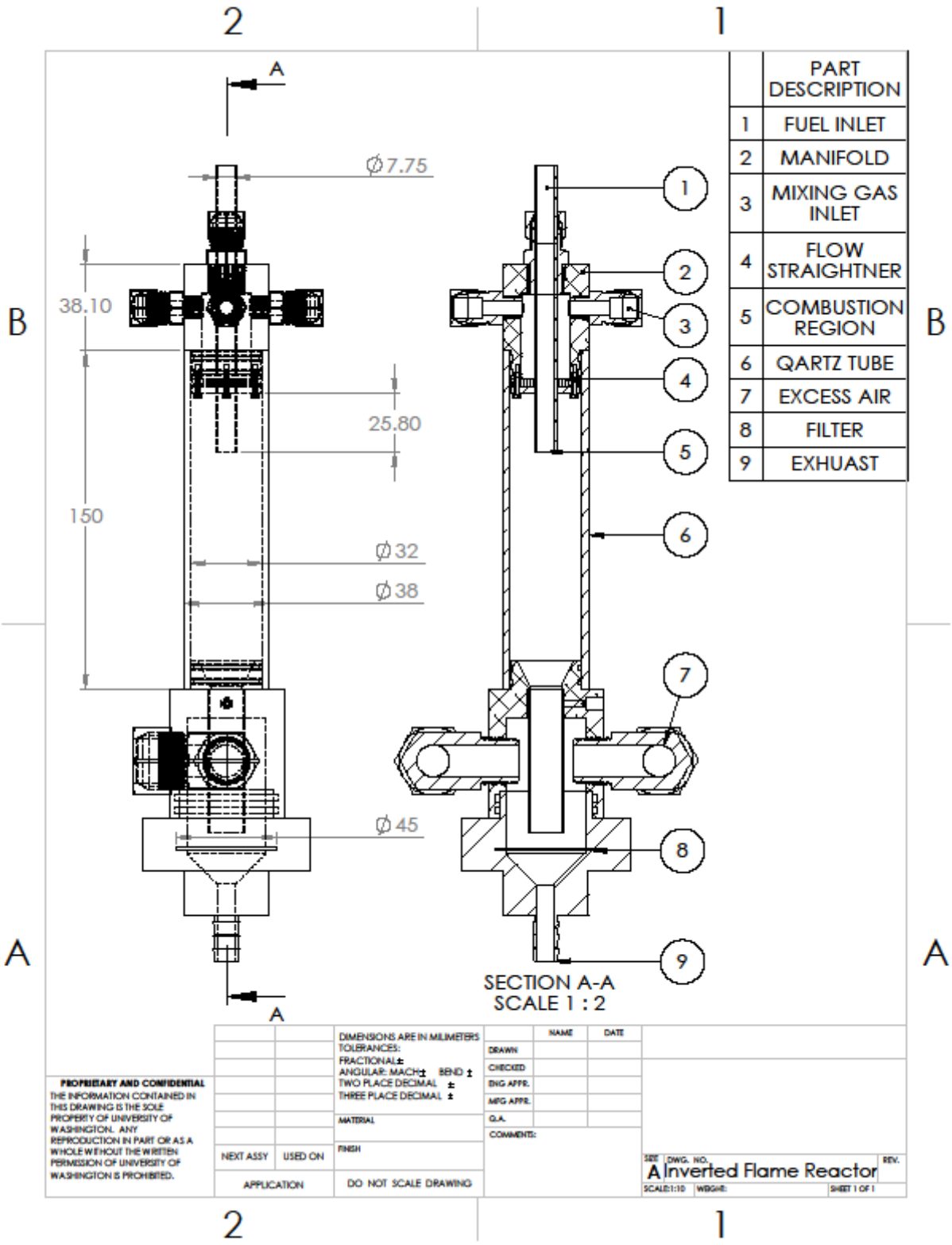

Figure 6.8. Engineering drawings of the IGFR

6.5 EXPERIMENTAL DILUTED FLAME PICTURES

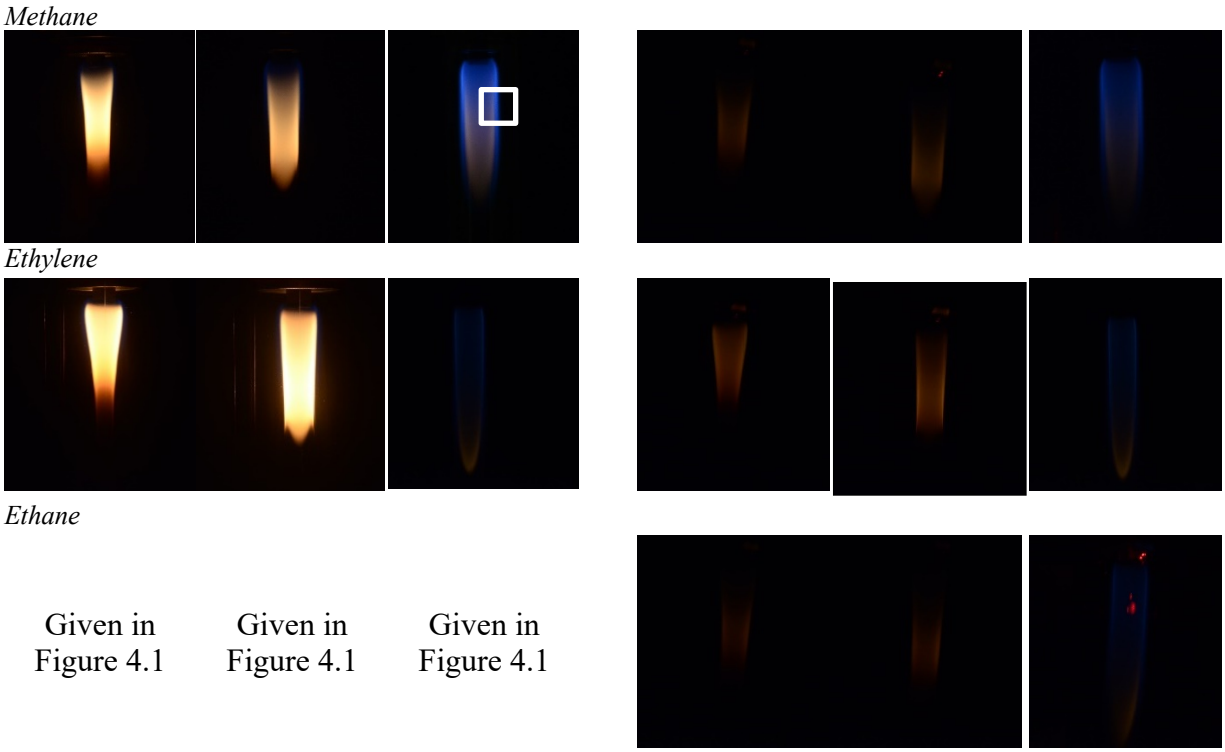

Figure 6.9. LEFT: Images taken from the flames at oversaturated camera conditions. RIGHT: Low exposure experimental flame pictures used to find the highest soot volume fraction location. The laser seen in the 85% dilution ethane flame is used to set pixel resolution.

6.6 INCONEL PROBE SOOT COLLECTION

Soot from a 75% dilution ethylene flame is collected using the Inconel probe is given in Figure 6.10. HRTEM imaging ensures the soot produces the shell-core structure.

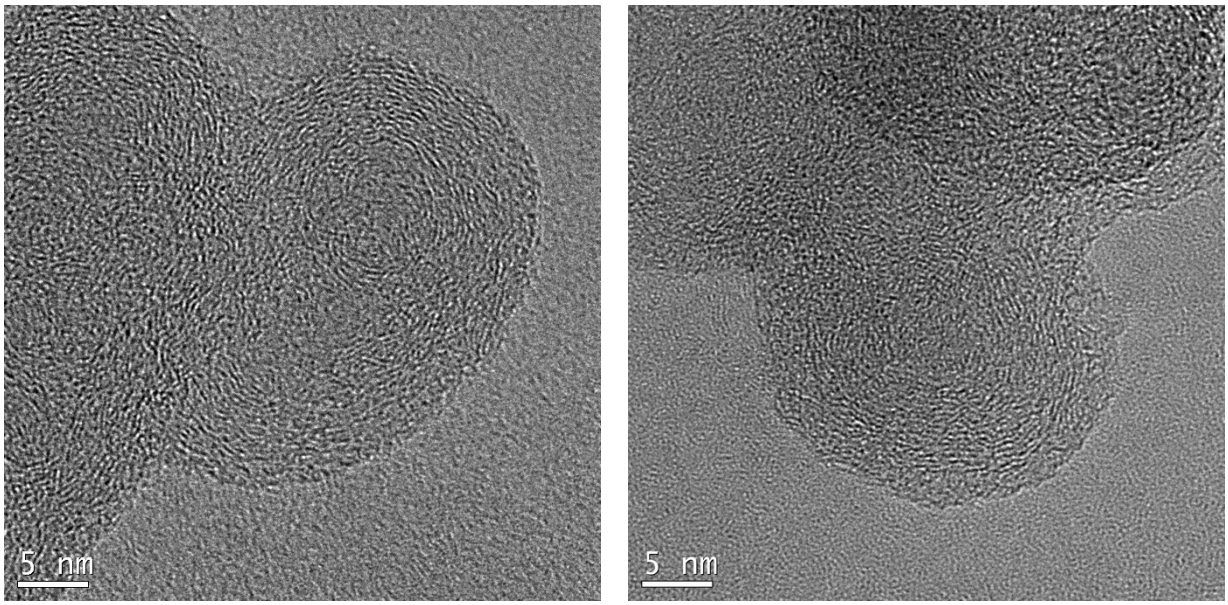

Figure 6.10. Ethane soot collected with the Inconel probe at 75% dilution. All locations viewed displayed the core shell structure.

6.7 HRTEM- THRESHOLD PARAMETER

Threshold limit effect on the stacked fringes, shown in Figure 6.11.

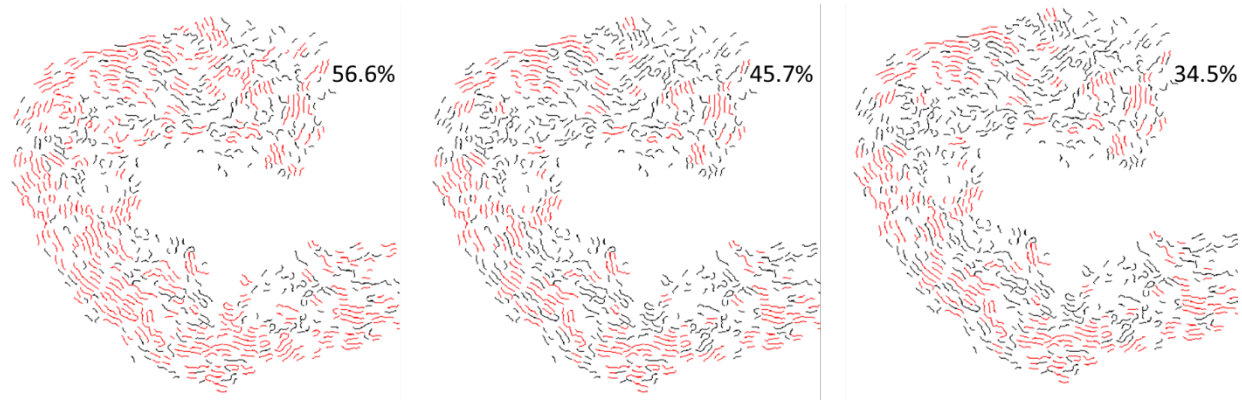

Figure 6.11. Changing the parallel threshold set at a) 0.12 nm b) 0.16 nm, and c) 0.20 nm. Red fringes are considered stacked.

6.8 HRTEM IMAGES FOR NANOSTRUCTURE ANALYSIS

The pictures used in HRTEM nanostructure analysis are given in Figure 6.12.

Methane No Dilution

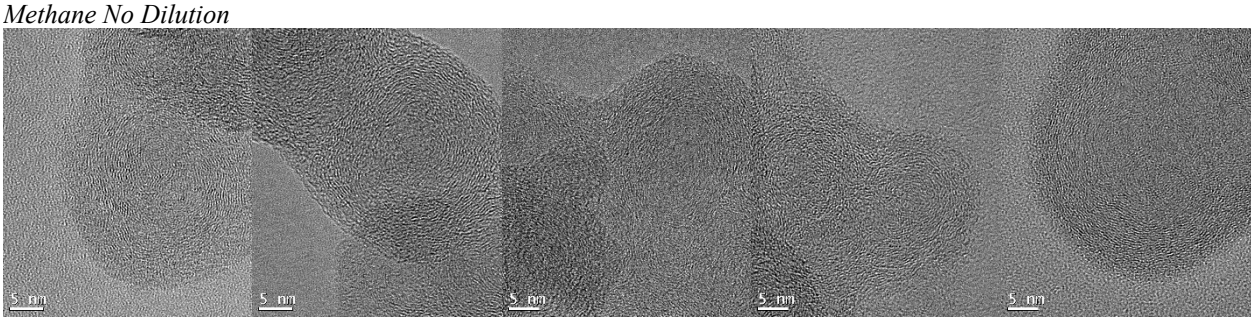

Methane 50% Dilution

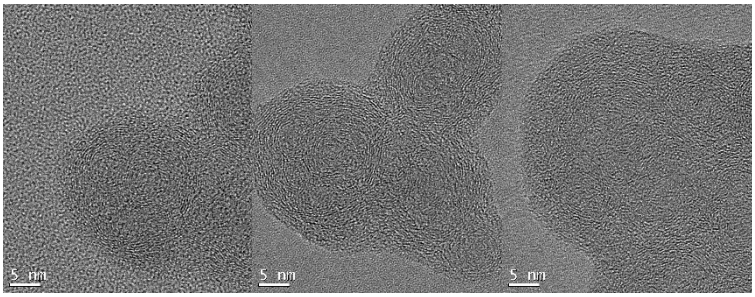

Methane 67% Dilution

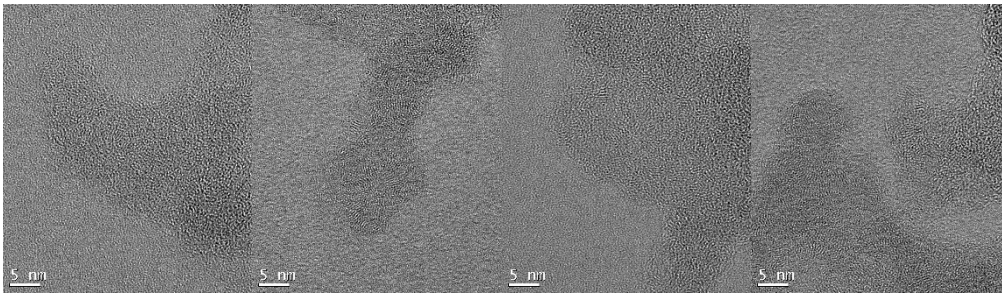

Ethane No Dilution

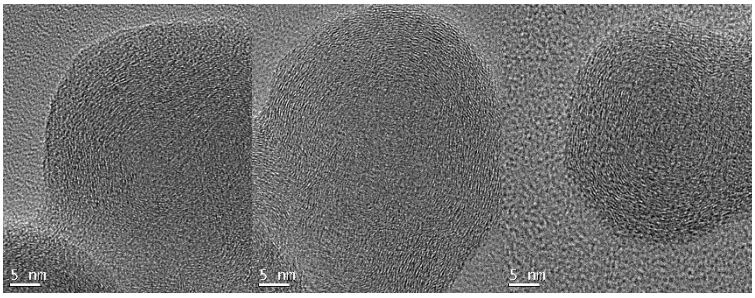

Ethane 50% Dilution

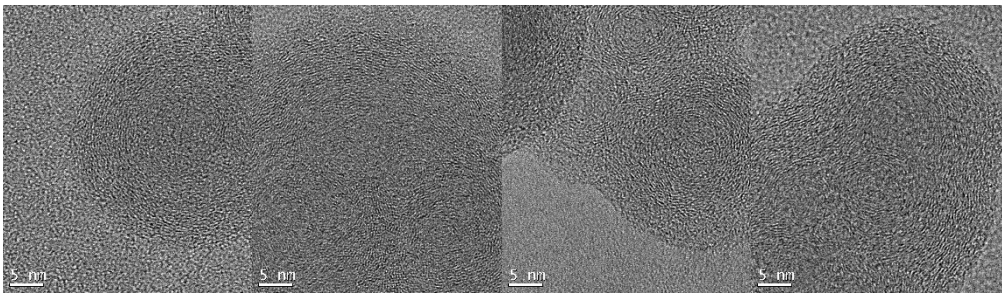

Ethane 85% Dilution

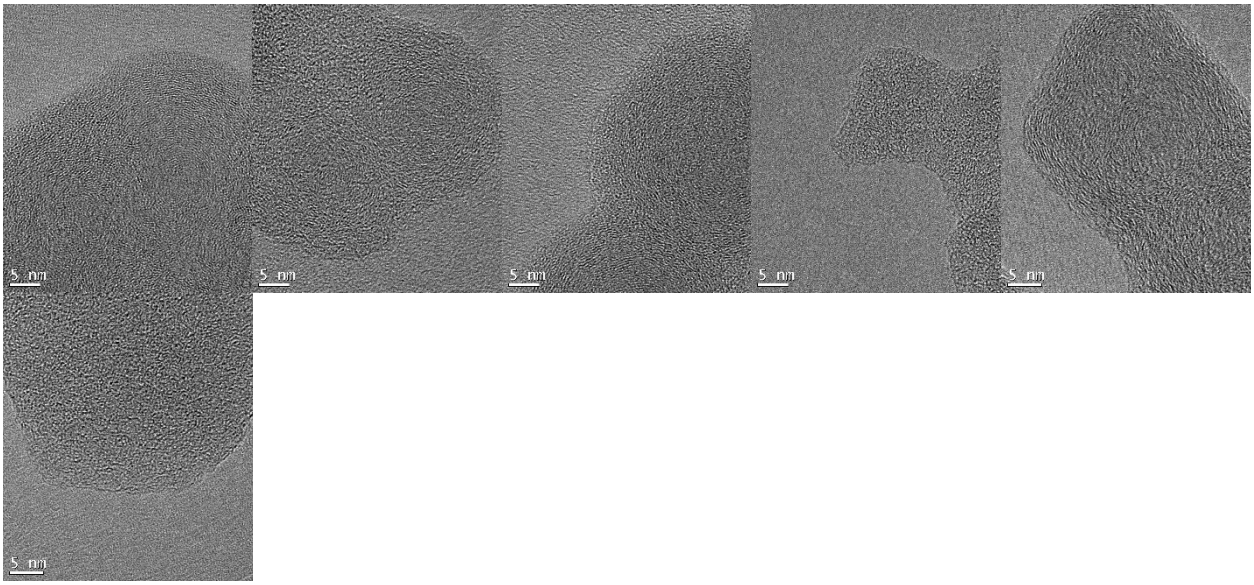

Ethylene No Dilution

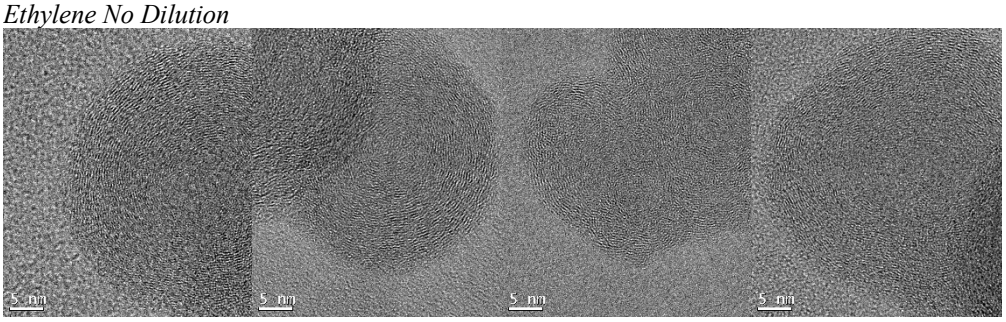

Ethylene 67% Dilution

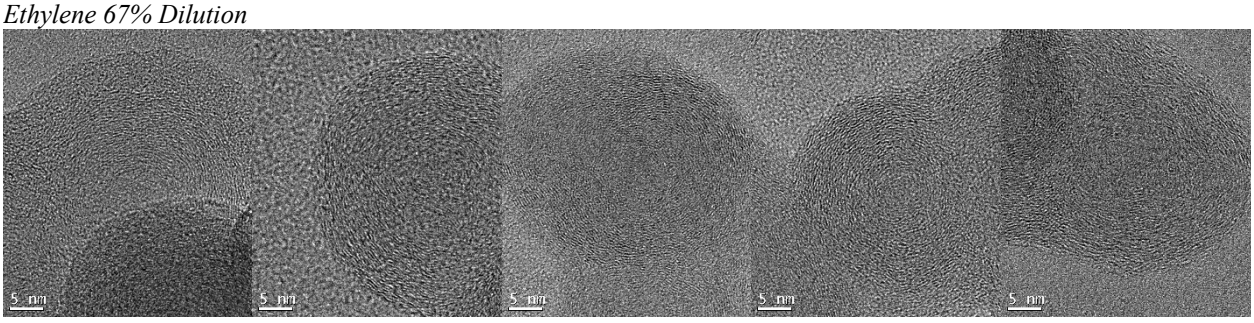

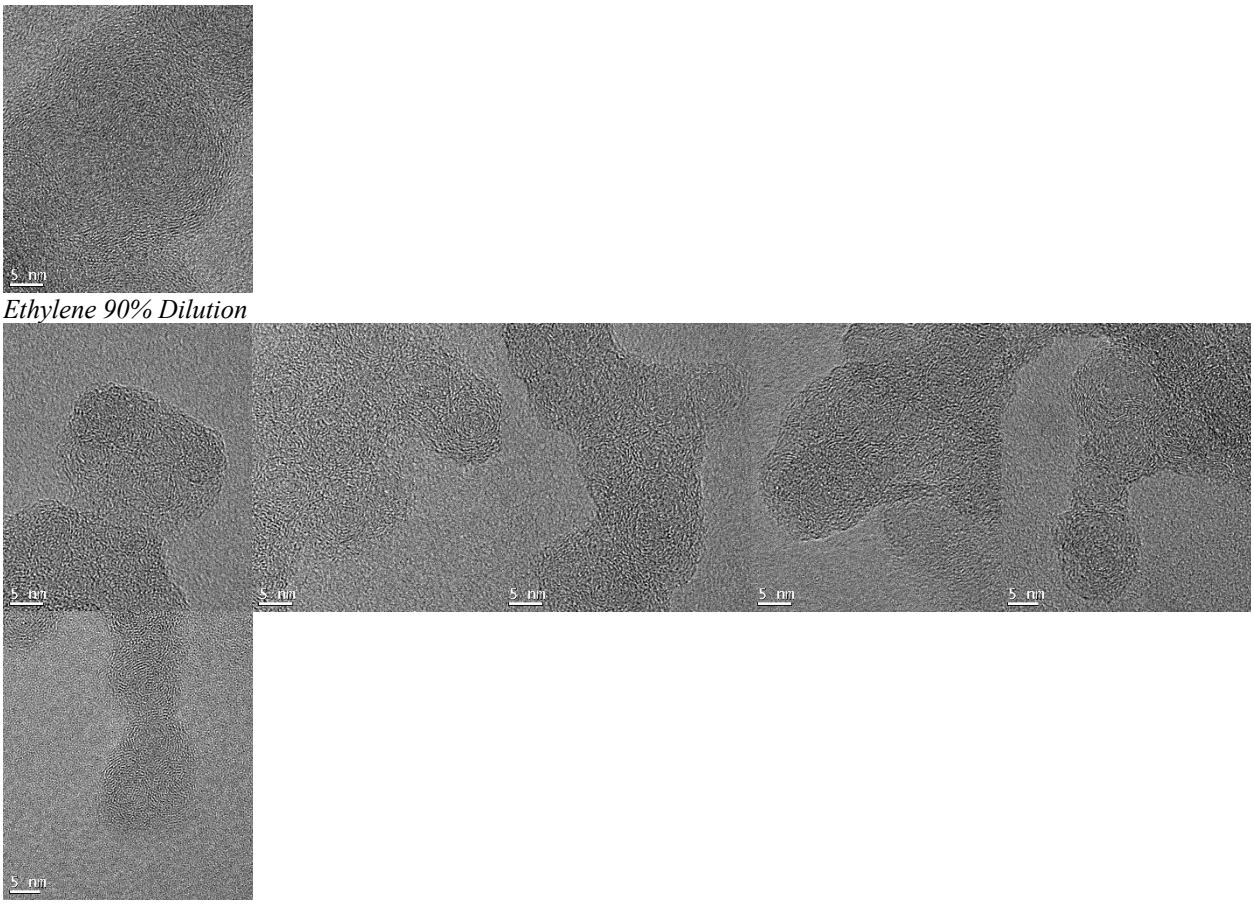

Ethylene 90% Dilution

Figure 6.12. All HRTEM images used for nanostructure analysis

6.9 ELECTRON BEAM INDUCED STRUCTURAL CHANGES

To observe if the electron beam increased structural order of unstructured soot particles, an image of a young soot particle was captured every two minutes for 22 minutes. Due to sample drift, the images are not all in focus to allow for a quantitative analysis. The electron beam does seem to generate longer and stacked fringes on the periphery of the soot particle after 22 minutes, shown in Figure 6.13.

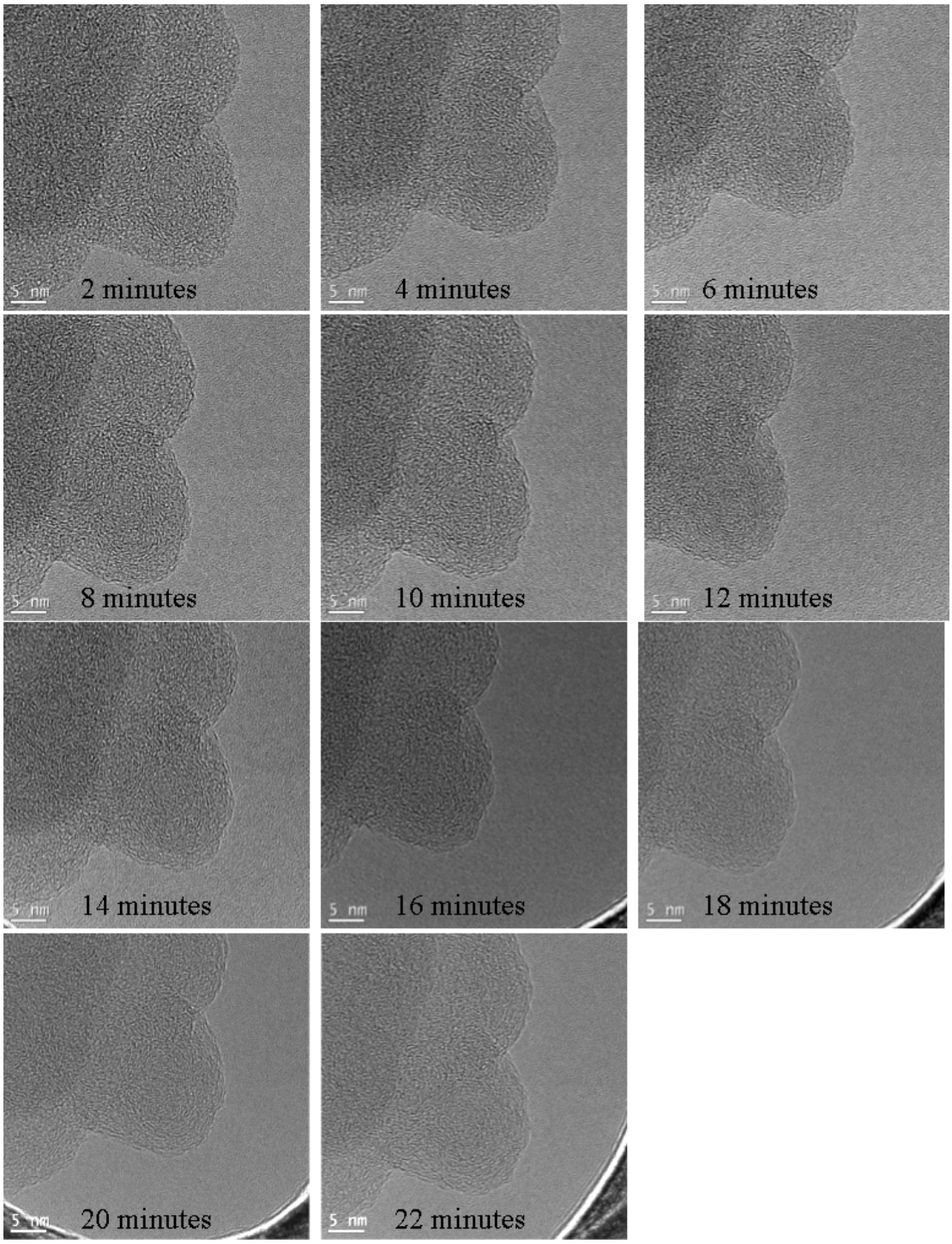

Figure 6.13. Time dependence for a young soot particle. There seems to be negligible changes over a 22 minute time frame. All HRTEM images were captured within 10 minutes of exposure, so the images are a good representation of the young soot particles

6.10 IMAGE ANALYSIS FOR TEMPERATURE MEASUREMENTS

As mentioned in 4.2.2, maximum flame temperature does not adequately describe the temperature soot is exposed to for the series of diluted flames, and instead the point of highest luminescence is extracted for characterization from the different flames. This section will describe the process used to find the highest luminescence point.

First, a camera is situated even with the IGFR fuel injection nozzle on a tripod. Two lasers were pointed 80.0 cm apart from each other parallel to the reactor axis in order to calibrate location and pixel resolution for the captured images. Next multiple images for each flame are captured. The images had varying shutter speeds and exposure times in order to avoid image saturation. Once pictures for the entire flame set were captured, Matlab was used to find the point of highest luminosity.

The Matlab script only used the red layer of each image. This red layer was deemed adequate due to the blackbody radiation of the soot particles emitting more strongly in the red region. Next, the images were calibrated based on the position of the two lasers. Finally, an image threshold was used to find the height of maximum pixel intensity. This location was used along with an interpolation of the axial temperature measurements as the T* value. A 5-10% threshold value was used to find a range of temperature measurements that the soot particles could be exposed to. Overall, this process worked well for the highest dilution ethane and ethylene flames. These two flames produced flames that radiated red in the flame tip and the maximum intensity location was close to the point of temperature measurement. The highest dilution methane flame, along with the lower dilution flames did not produce the radiating flame tip and the temperature measurements are less accurate. The temperature measurement is less accurate especially due to uncertainties

between the location of maximum soot volume fraction and maximum temperature at a given height. This uncertainty can lead to deviations in temperature in excess of 300 K.

6.11 MATLAB SCRIPT FOR IMAGE PROCESSING

The following script is used to process HRTEM images at 490k x magnification. The script can also be found at the following repository:

https://github.com/justid3/HRTEM-Image-Processing

```
% %%% Load the image that needs to be processed
% clear all
pic = 'TEM_1058.tif';
A = imread(pic);
resolution = .0261;    %nm/pixel   .0208   .0231   0.0261

%% 1)Define a region of interest (ROI) to analyze the particle. Draw freehand,
%double click or exit out of image after drawing to continue script
imshow(A)
roi = createMask(imfreehand);
position = wait(imfreehand);

for i = 1: size(A,1)
   for j = 1: length(A)
      if roi(i,j)==0
         A(i,j)=0;
      end
   end
end

%% 2) Adjust the pictures contrast with a histogram equalization.
% B = histeq(A);            %Increase Contrast
B = adapthisteq(A);       %Increase Contrast

%% 3)Remove Noise with a low pass Gaussian filter. Botero uses a 7 pixel
%%filter size and 3 pixel deviation
Gaus = fspecial('gaussian',[11 11],5);
C = imfilter(B,Gaus);
% P = imgaussfilt(B ,  5,'FilterSize',[11 11]);

%% 4) Bottom Hat transformation. Botero uses a 2x2 disk element
se = strel('disk',4);
D = imbothat(C,se);
```

```
%% 5) Sets a threshold and binarizes the image using Otsu's method
level = graythresh(D);
E = imbinarize(D,level);

%% 6) skeletonization of the image
F = bwmorph(E,'skel',Inf);
F = bwmorph(F,'fill');
F = bwmorph (F,'skel');

%% 7) Further morphological operations of cleaning isolated pixels and breaking fringes in the h
form
G = bwmorph (F,'clean');
G = bwmorph ( F,'hbreak',8);


%% 8) breaks apart fringes with >3 connections
I=G;
% I( (conv2(I,[1 1 1;1 0 1;1 1 1],'same') .* I) > 2 ) = 0;

pts = bwlookup(G,makelut(@(x) sum(x(:))>=4 & x(5)==1,3)); %branch points?
I = G&~pts;
I = bwmorph(I,'clean');
I = I+pts/2;


%% do it again
i = 1;
for i=1:3
I(I>0)=1;
pts2 = bwlookup(I,makelut(@(x) sum(x(:))>=4 & x(5)==1,3)); %branch points?
I = I&~pts2;
I = bwmorph(I,'clean');
I = I+pts2/2;
end

I(I > 0) = 1;
% imshowpair(G,A,'montage')

   %% Measure the length of fringes in path walked start to end
% measurements = regionprops(G,'area');    % counts the total number of pixels
[l, k] = find(bwmorph(I,'endpoints'));
fringemeasurement=zeros(1,length(l));
H = I;
for a = 1: length(l)
    i = l(a);
```

```
    j = k(a);
    fringemeasurement(a) = 1;
    while H(i, j) == 1
        if bwarea(H(i + 1, j)) == 1            %% if the location TTR is true, then add 1
            fringemeasurement(a) = fringemeasurement(a) + 1;
            H(i,j)=0;
            i=i+1;                             % Follow that path
        elseif bwarea(H(i,j+1))==1          %%% if the location Above is true, then add 1
            fringemeasurement(a)= fringemeasurement(a) +1;
            H(i,j)=0;
            j=j+1;
        elseif bwarea(H(i-1,j))==1          %% if the location TTL is true, then add 1
            fringemeasurement(a)= fringemeasurement(a) +1;
            H(i,j)=0;
            i=i-1;
        elseif bwarea(H(i,j-1))==1          %%% if the location Below is true, then add 1
            fringemeasurement(a)= fringemeasurement(a) +1;
            H(i,j)=0;
            j=j-1;
        elseif bwarea(H(i+1,j+1))==1          %%% if the location TTR and Above is true, then add 1
            fringemeasurement(a)= fringemeasurement(a) + sqrt(2);
            H(i,j)=0;
            i=i+1;
            j=j+1;
        elseif bwarea(H(i+1,j-1))==1          %%% if the location TTR and Below is true, then add 1
            fringemeasurement(a)= fringemeasurement(a) +sqrt(2);
            H(i,j)=0;
            i=i+1;
            j=j-1;
         elseif bwarea(H(i-1,j-1))==1          %%% if the location TTL and Below is true, then add 1
            fringemeasurement(a)= fringemeasurement(a) +sqrt(2);
             H(i,j)=0;
              i=i-1;
              j=j-1;
         elseif bwarea(H(i-1,j+1))==1          %%% if the location TTL and above is true, then add 1
            fringemeasurement(a)= fringemeasurement(a) +sqrt(2);
            H(i,j)=0;
            j=j+1;
            i=i-1;
        else
            H(i,j)=0;
        end
    end
end

%% Measure the distance between fringe endpoints
```

```
[l,k] = find(bwmorph(I,'endpoints'));
euclength=zeros(1,length(l));
H=I;
for a = 1:length(l)
   i = l(a);
   j = k(a);
   while H(i,j)== 1
      if bwarea(H(i+1,j)) == 1          %% if the location TTR is true, then add 1
         H(i,j)=0;
         i=i+1;                         % Follow that path
      elseif bwarea(H(i,j+1))==1        %%% if the location Above is true, then add 1
         H(i,j)=0;
         j=j+1;
      elseif bwarea(H(i-1,j))==1        %% if the location TTL is true, then add 1
         H(i,j)=0;
         i=i-1;
      elseif bwarea(H(i,j-1))==1        %%% if the location Below is true, then add 1
         H(i,j)=0;
         j=j-1;
      elseif bwarea(H(i+1,j+1))==1      %%% if the location TTR and Above is true, then add 1
         H(i,j)=0;
         i=i+1;
         j=j+1;
      elseif bwarea(H(i+1,j-1))==1      %%% if the location TTR and Below is true, then add 1
         H(i,j)=0;
         i=i+1;
         j=j-1;
       elseif bwarea(H(i-1,j-1))==1     %%% if the location TTL and Below is true, then add 1
          H(i,j)=0;
          i=i-1;
          j=j-1;
       elseif bwarea(H(i-1,j+1))==1     %%% if the location TTL and above is true, then add 1
         H(i,j)=0;
         j=j+1;
         i=i-1;
      else
         H(i,j)=0;
      end
      euclength(a)=sqrt((i-l(a))^2+(j-k(a))^2);%i and j are then the end points. So sqrt((i-
l(a))^2+(j-k(a))^2)
   end
end

%% Remove the uneeded ones, and measure the tortuosity
indices = fringemeasurement < .483/resolution;    % < 17.9 pixels (.483 nm) deemed unrealistic
becasue size of two rings
```

```
fringemeasurement(indices) = [];
euclength(indices) = [];
tortuosity= fringemeasurement./euclength;
fringelength=fringemeasurement*resolution;

%% Calculate the angle of each point
[l,k] = find(bwmorph(I,'endpoints'));
l(indices)=[];          %removing the ones that are shorter than the required distance
k(indices)=[];          %removing the ones that are shorter than the required distance
H=double(I);
angle=zeros(2048:2048);
for a = 1:length(l)
   i = l(a);
   j = k(a);
   while H(i,j)== 1
      if bwarea(H(i+1,j)) == 1          %% if the location above is true, then angle is 90 degrees
         angle(i,j)=270;
         H(i,j)=0;
         i=i+1;                         % Follow that path
      elseif bwarea(H(i,j+1))==1        %%% if the location Above is true, then add 1
         angle(i,j)=360;
         H(i,j)=0;
         j=j+1;
      elseif bwarea(H(i-1,j))==1        %% if the location TTL is true, then add 1
         angle(i,j)=90;
         H(i,j)=0;
         i=i-1;
      elseif bwarea(H(i,j-1))==1        %%% if the location Below is true, then add 1
         angle(i,j)=180;
         H(i,j)=0;
         j=j-1;
      elseif bwarea(H(i+1,j+1))==1      %%% if the location TTR and Above is true, then add 1
         angle(i,j)=315;
         H(i,j)=0;
         i=i+1;
         j=j+1;
      elseif bwarea(H(i+1,j-1))==1      %%% if the location TTR and Below is true, then add 1
         angle(i,j)=225;
         H(i,j)=0;
         i=i+1;
         j=j-1;
       elseif bwarea(H(i-1,j-1))==1     %%% if the location TTL and Below is true, then add 1
          angle(i,j)=135;
          H(i,j)=0;
           i=i-1;
           j=j-1;
```

```
      elseif bwarea(H(i-1,j+1))==1          %%% if the location TTL and above is true, then add 1
         angle(i,j)=45;
         H(i,j)=0;
         j=j+1;
         i=i-1;
      else
         H(i,j)=0;
         angle(i,j)=sum(sum(angle(i-1:i+1,j-1:j+1)));
      end
   end
end

%% Label each fringe with a unique number
[l,k] = find(bwmorph(I,'endpoints'));
l(indices)=[];          %removing the ones that are shorter than the required distance
k(indices)=[];          %removing the ones that are shorter than the required distance
Unique = double(I);
for a = 1:length(l)
   i = l(a);
   j = k(a);
   while Unique(i,j)== 1
      Unique(i,j)= a+1;
      if sum(sum(roi((i-1:i+1),(j-1:j+1))))~=9
         Unique(i,j)=0;
      elseif Unique(i+1,j) == 1           %% if the location below is true, then add 1
         i=i+1;
      elseif Unique(i,j+1)== 1          %%% if the location Above is true, then add 1
         j=j+1;
      elseif Unique(i-1,j)==1          %% if the location TTL is true, then add 1
         i=i-1;
      elseif Unique(i,j-1)==1          %%% if the location Below is true, then add 1
         j=j-1;
      elseif Unique(i+1,j+1)==1         %%% if the location TTR and Above is true, then add 1
         i=i+1;
         j=j+1;
      elseif Unique(i+1,j-1)==1         %%% if the location TTR and Below is true, then add 1
         i=i+1;
         j=j-1;
       elseif Unique(i-1,j-1)==1         %%% if the location TTL and Below is true, then add 1
          i=i-1;
          j=j-1;
       elseif Unique(i-1,j+1)==1         %%% if the location TTL and above is true, then add 1
         j=j+1;
         i=i-1;
      end
   end
```

```
end
%% Remove all points for short fringes
for i=1:2048
   for j=1:2048
      if Unique(i,j)==1
         Unique(i,j)=0;
      end
   end
end

%% 5 nearest neighbors average angle
[m,n]=find(angle);
angleave=zeros(2048,2048);
x=zeros(2048,2048);
y=zeros(2048,2048);

for i=1:length(m)
   x(m(i),n(i))=cosd(angle(m(i),n(i)));
   y(m(i),n(i))=sind(angle(m(i),n(i)));
end
for i=1:length(m)
   a = sum(sum(x(m(i)-2:m(i)+2,n(i)-2:n(i)+2)));
   b = sum(sum(y(m(i)-2:m(i)+2,n(i)-2:n(i)+2)));
   angleave(m(i),n(i))= atan2d(b,a);
end

for i=1:2048
   for j=1:2048
      if Unique(i,j)==0
         angleave(i,j)=0;
      end
   end
end
[m,n]=find(bwmorph(Unique,'endpoints'));

for i=1:length(m)
   a = sum(sum(x(m(i)-1:m(i)+1,n(i)-1:n(i)+1)));
   b = sum(sum(y(m(i)-1:m(i)+1,n(i)-1:n(i)+1)));
   angleave(m(i),n(i))= atan2d(b,a);
end
%% then need to say if there are any other fringes with the same vertical position and log if they
are
% [l,n] = find(Unique);   %points of G that are on the fringes greater than a certain distance
verticali1=zeros(length(l),length(l));
verticali2=zeros(length(l),length(l));
verticalj=zeros(length(l),length(l));
```

```
stackedfringesi=[0];
stackedfringesj=[0];%zeros(length(l),length(l));
StackedDist =  0.8;   %(in nanometers)
UniqueFringes=length(unique(Unique));
angldev=10;
separation=0;
for iter = 1 : UniqueFringes
    [i,j] = find(Unique==iter);       %      i = l(iter);      %points on Unique matrix
      for q=1:length(i)     %      j = n(iter);       %points on Unique matrix
            if angleave(i(q),j(q))>0
            theta=(angleave(i(q),j(q)))-90;
            else
            theta=(angleave(i(q),j(q)))+90;
            end
          mi = i(q) + round(StackedDist/resolution*sind(theta));
          mj = j(q) - round(StackedDist/resolution*cosd(theta));
          for z=1:round(2*StackedDist/resolution)  %while i < 2048 if the fringe numbers are
equal do nothing, else log fringe
          if resolution*((i(q)-(mi-round(z*sind(theta))))^2+(j(q)-(mj+ round(z*cosd(theta))))^2)^.5
> StackedDist+.1
              meta
          elseif  Unique(i(q),j(q)) == Unique (mi-round(z*sind(theta)),mj+ round(z*cosd(theta)))
%if on same fringe, NEXT
          elseif Unique(mi-round(z*sind(theta)),mj+ round(z*cosd(theta))) > 1  &
angleave(i(q),j(q))-angldev <= angleave(mi-round(z*sind(theta)),mj+ round(z*cosd(theta))) &
angleave(i(q),j(q))+angldev>=angleave(mi-round(z*sind(theta)),mj+ round(z*cosd(theta)))
           stackedfringesi=[stackedfringesi; Unique(i(q),j(q))];
           stackedfringesj=[stackedfringesj;Unique(mi-round(z*sind(theta)),mj+
round(z*cosd(theta)))]; %log the two fringe numbers  (iter,j)
           separation=[separation;((i(q)-(mi-round(z*sind(theta))))^2+(j(q)-(mj+
round(z*cosd(theta)))))^2)^.5];
          else
          end
         end
    end
end
separation(separation<.00001)=[];
stackedfringesi(stackedfringesi<1)=[];
stackedfringesj(stackedfringesj<1)=[];
separation=separation*resolution;
stackedfringe=[stackedfringesi stackedfringesj];
stackedfringe = unique(stackedfringe);
% length(stackedfringe)/max(Unique(:))
% [mean(fringelength) mean(tortuosity) length(stackedfringesfin)/max(Unique(:))
max(Unique(:))]
```

```
%% Need to change script in order to account for the distance between pixels. Record the
distance, then if they are 'stacked', add to the separation array. If not, delete the array
%Is there a way to index which specific pixels are stacked? The current
%process goes 1) find alll the stacked pixels, and label them by saying
%that fringe number 2) see how many repitions there are for that given
%pair, say fringe1 and fringe2. So this strategy is no bueno. I can log the
%distance as script finds the ones close to each other, then delete the
%inputs that are removed?
stackedfringes=[0 0];
stckdpxl=0.20/resolution;     %The number is nm
separationtot=0;
separationmean=0;
for i=1: length (stackedfringe)
   repititions=0;
   points = find(stackedfringesi == stackedfringe(i));
   sep=0;
   for j = 1:length (points)
      if stackedfringesj(points(1)) == stackedfringesj(points(j))
         if stackedfringe(i) == stackedfringesi(points(j)) & stackedfringesj(points(1)) ==
stackedfringesj(points(j))
         repititions = repititions + 1;
         sep=[sep;separation(points(j))];
         end
         if repititions > stckdpxl
         stackedfringes = [stackedfringes; stackedfringesi(points(j)) stackedfringesj(points(j))];
         separationtot=[separationtot;sep];
         separationmean=[mean(sep);separationmean];
         repititions=0;
         end
      elseif stackedfringesj(points(1)) ~= stackedfringesj(points(j))
         if stackedfringe(i) == stackedfringesi(points(j)) & stackedfringesj(points(1)) ==
stackedfringesj(points(j))
         repititions = repititions + 1;
         sep=[sep;separation(points(j))];
         end
         if repititions > stckdpxl
         stackedfringes = [stackedfringes; stackedfringesi(points(j)) stackedfringesj(points(j))];
         separationtot=[separationtot;sep];
         separationmean=[mean(sep);separationmean];
         end
      end
   end
end
separationtot(separationtot < .0001)=[];
separationmean(separationmean < .00001)=[];
separationtot(separationtot > 0.6) = []; %0.6)=[];
```

```
separationmean(separationmean > 0.6) = [];     %2*min(separationtot)
stackedfringesfin= [stackedfringes(:, 1) ; stackedfringes(:, 2)];
stackedfringesfin(stackedfringesfin < 1) = [];
stackedfringesfin = unique(stackedfringesfin);
% length(stackedfringesfin)/length(unique(Unique))
%% Plot Stuff Plot fringe length and tortuosity for each individual trial
% plot1=histogram(fringelength,50,'binlimits',[0.4,6],'Normalization','probability');
% plot2=histogram(tortuosity,50,'binlimits',[1,5],'Normalization','probability');
%
% subplot(1,2,1);
plot1=histogram(fringelength,50,'binlimits',[0.4,4],'Normalization','probability');
% subplot(1,2,2); plot2=histogram(tortuosity,50,'binlimits',[1,2],'Normalization','probability');
% subplot(2,2,3); plot1=histogram(dishor,20,'binlimits',[0.3,0.9],'Normalization','probability');
% subplot(2,2,4); plot2=histogram(disvert,20,'binlimits',[0.3,0.9],'Normalization','probability');

% HighTor= sum(tortuosity > 1.5)/sum(tortuosity>0);  %HighTor is the percent of fringes with
tortuosity>1.5
c = unique(stackedfringe);
%% Plot it
% yyaxis left
% plot(distance.*resolution,results(:,3),distance.*resolution,results(:,2))
% xlabel('Distance From Center (nm)')
% ylabel('Length (nm)                    Ratio')
% yyaxis right
% plot(distance.*resolution,results(:,4))
% ylabel('Percent Stacked')
% legend('Fringe Length','Tortuosity','Percent of Stacked Layers','Location','southeast')
% legend('boxoff')

%% After Loading the excel file in that contains Standard Deviation of: Tortuosity, Fringe
Length, Percent stacked as 'results.mat'
% errtor = (results(:,1));
% errFL=(results(:,2));
% errstacked=results(:,3);
%%
ColorMap= zeros(2048: 2048);
stackedfringesfin(stackedfringesfin < 1) = [];
for i = 1: length(Unique)
   for j = 1: length(Unique)
      if Unique(i,j) ~= 0
         ColorMap(i, j) = 10;
      end
   end
end

for i=1:length(stackedfringesfin)
```

```
    [l,m] = find(Unique == stackedfringesfin(i));
    for k=1:length(l)
        ColorMap(l(k),m(k))=500;
    end
end
image(ColorMap)
% imagesc(ColorMap)
%% Plot it
% yyaxis left
% errorbar(distance.*resolution,results(:,2),errFL)
% hold on
% errorbar(distance.*resolution,results(:,1),errtor)
% xlabel('Distance From Center (nm)')
% ylabel('Length (nm)                    Ratio')
% yyaxis right
% yyaxis right
% errorbar(distance.*resolution,results(:,3),errstacked)
% ylabel('Percent Stacked')
% legend('Fringe Length','Tortuosity','Percent of Stacked Layers','Location','southeast')
% legend('boxoff')
% hold off
Results = ["FL" "T" "PSL" "Separation" "Fringes"; mean(fringelength) mean(tortuosity)
length(stackedfringesfin)/length(unique(Unique)) mean(separationmean)
length(unique(stackedfringe))]
```

ACKNOWLEDGMENTS

This work was partially supported by the National Institutes of Health (grant numbers: NIBIB U01 EB021923, NIBIB R42ES026532 subcontract to UW). Part of this work was conducted at the Molecular Analysis Facility, a National Nanotechnology Coordinated Infrastructure site at the University of Washington which is supported in part by the National Science Foundation (grant ECC-1542101), the University of Washington, the Molecular Engineering & Sciences Institute, the Clean Energy Institute, and the National Institutes of Health. CFD calculations were facilitated through the use of advanced computational, storage, and networking infrastructure provided by the Hyak supercomputer system and funded by the STF at the University of Washington

BIBLIOGRAPHY

[1] R. H. Hurt, G. P. Crawford, and H.-S. Shim, "Equilibrium nanostructure of primary soot particles," *Proceedings of the Combustion Institute,* vol. 28, pp. 2539-2546, 2000.

[2] M. R. Kholghy, A. Veshkini, and M. J. Thomson, "The core–shell internal nanostructure of soot–A criterion to model soot maturity," *Carbon,* vol. 100, pp. 508-536, 2016.

[3] A. Karakatsani, A. Analitis, D. Perifanou, J. Ayres, R. Harrison, A. Kotronarou*, et al.*, "Particulate matter air pollution and respiratory symptoms in individuals having either asthma or chronic obstructive pulmonary disease: a European multicentre panel study," *Environmental Health,* vol. 11, p. 75, 2012.

[4] A. Zanobetti and J. Schwartz, "The effect of fine and coarse particulate air pollution on mortality: a national analysis.(Research)," *Environmental Health Perspectives,* vol. 117, p. 898, 2009.

[5] J. Liu, E. Scheuer, J. Dibb, L. D. Ziemba, K. L. Thornhill, B. E. Anderson*, et al.*, "Brown carbon in the continental troposphere," *Geophysical Research Letters,* vol. 41, pp. 2191-2195, 2014.

[6] X. Wang, C. L. Heald, D. A. Ridley, J. P. Schwarz, J. R. Spackman, A. E. Perring*, et al.*, "Exploiting simultaneous observational constraints on mass and absorption to estimate the global direct radiative forcing of black carbon and brown carbon," *Atmospheric Chemistry and Physics Discussions,* vol. 14, pp. 17527-17583, 2014.

[7] D. Chen, J. Akroyd, S. Mosbach, D. Opalka, and M. Kraft, "Solid–liquid transitions in homogenous ovalene, hexabenzocoronene and circumcoronene clusters: A molecular dynamics study," *Combustion and Flame,* vol. 162, pp. 486-495, 2015.

[8] K. Bowal, J. W. Martin, and M. Kraft, "Partitioning of polycyclic aromatic hydrocarbons in heterogeneous clusters," *Carbon,* vol. 143, pp. 247-256, 2019.

[9] V. Hindasageri, R. Vedula, and S. Prabhu, "Thermocouple error correction for measuring the flame temperature with determination of emissivity and heat transfer coefficient," *Review of Scientific Instruments,* vol. 84, p. 024902, 2013.

[10] C. R. Shaddix, "Correcting thermocouple measurements for radiation loss: a critical review," Sandia National Labs., Livermore, CA (US)1999.

[11] M. R. Kholghy, Y. Afarin, A. D. Sediako, J. Barba, M. Lapuerta, C. Chu*, et al.*, "Comparison of multiple diagnostic techniques to study soot formation and morphology in a diffusion flame," *Combustion and Flame,* vol. 176, pp. 567-583, 2017.

[12] G.-B. Kim, S.-W. Cho, J.-H. Lee, D.-S. Jeong, Y.-J. Chang, and C.-H. Jeon, "Study on Soot Primary Particle Size Measurement in Ethylene Diffusion Flame by Time-Resolved Laser-Induced Incandescence," *Transactions of the Korean Society of Mechanical Engineers B,* vol. 30, pp. 973-981, 2006.

[13] M. Saffaripour, A. Veshkini, M. Kholghy, and M. J. Thomson, "Experimental investigation and detailed modeling of soot aggregate formation and size distribution in laminar coflow diffusion flames of Jet A-1, a synthetic kerosene, and n-decane," *Combustion and Flame,* vol. 161, pp. 848-863, 2014.

[14] J. Schindelin, I. Arganda-Carreras, E. Frise, V. Kaynig, M. Longair, T. Pietzsch*, et al.*, "Fiji: an open-source platform for biological-image analysis," *Nature methods,* vol. 9, pp. 676-682, 2012.

[15] K. Yehliu, R. L. Vander Wal, and A. L. Boehman, "Development of an HRTEM image analysis method to quantify carbon nanostructure," *Combustion and Flame,* vol. 158, pp. 1837-1851, 2011.

[16] M. L. Botero, E. M. Adkins, S. González-Calera, H. Miller, and M. Kraft, "PAH structure analysis of soot in a non-premixed flame using high-resolution transmission electron microscopy and optical band gap analysis," *Combustion and Flame,* vol. 164, pp. 250-258, 2016.

[17] N. Otsu, "A threshold selection method from gray-level histograms," *IEEE transactions on systems, man, and cybernetics,* vol. 9, pp. 62-66, 1979.

[18] Q. Zhang, H. Guo, F. Liu, G. Smallwood, and M. Thomson, "Modeling of soot aggregate formation and size distribution in a laminar ethylene/air coflow diffusion flame with detailed PAH chemistry and an advanced sectional aerosol dynamics model," *Proceedings of the Combustion Institute,* vol. 32, pp. 761-768, 2009.

[19] Ü. Ö. Köylü, C. S. McEnally, D. E. Rosner, and L. D. Pfefferle, "Simultaneous measurements of soot volume fraction and particle size/microstructure in flames using a thermophoretic sampling technique," *Combustion and Flame,* vol. 110, pp. 494-507, 1997.

[20] N. J. Kempema and M. B. Long, "Combined optical and TEM investigations for a detailed characterization of soot aggregate properties in a laminar coflow diffusion flame," *Combustion and Flame,* vol. 164, pp. 373-385, 2016.

[21] B. Hu, B. Yang, and U. O. Koylu, "Soot measurements at the axis of an ethylene/air non-premixed turbulent jet flame," *Combustion and flame,* vol. 134, pp. 93-106, 2003.
[22] O. Popovicheva, M. Kistler, E. Kireeva, N. Persiantseva, M. Timofeev, V. Kopeikin*, et al.*, "Physicochemical characterization of smoke aerosol during large-scale wildfires: Extreme event of August 2010 in Moscow," *Atmospheric environment,* vol. 96, pp. 405-414, 2014.
[23] M. Frenklach, "Reaction mechanism of soot formation in flames," *Physical Chemistry Chemical Physics,* vol. 4, pp. 2028-2037, 2002.
[24] R. K. Chakrabarty, N. D. Beres, H. Moosmüller, S. China, C. Mazzoleni, M. K. Dubey*, et al.*, "Soot superaggregates from flaming wildfires and their direct radiative forcing," *Scientific reports,* vol. 4, 2014.
[25] F. Goodarzi, "Morphology and chemistry of fine particles emitted from a Canadian coal-fired power plant," *Fuel,* vol. 85, pp. 273-280, 2006/02/01/ 2006.
[26] Ü. Ö. Köylü and G. M. Faeth, "Structure of overfire soot in buoyant turbulent diffusion flames at long residence times," *Combustion and Flame,* vol. 89, pp. 140-156, 1992.
[27] V. Chernov, M. J. Thomson, S. B. Dworkin, N. A. Slavinskaya, and U. Riedel, "Soot formation with C 1 and C 2 fuels using an improved chemical mechanism for PAH growth," *Combustion and Flame,* vol. 161, pp. 592-601, 2014.
[28] H. Wang, X. You, A. V. Joshi, S. G. Davis, A. Laskin, F. Egolfopoulos*, et al.*, "USC Mech Version II. High-Temperature Combustion Reaction Model of H2/CO/C1-C4 Compounds," *http://ignis.usc.edu/USC_Mech_II.htm,* May 2007 2007.
[29] M. Luo, Y. Ying, and D. Liu, "Soot in flame-wall interactions: Views from nanostructure and reactivity," *Fuel,* vol. 212, pp. 117-131, 2018.
[30] M. Frenklach, "Method of moments with interpolative closure," *Chemical Engineering Science,* vol. 57, pp. 2229-2239, 2002.
[31] D. Aubagnac-Karkar, A. El Bakali, and P. Desgroux, "Soot particles inception and PAH condensation modelling applied in a soot model utilizing a sectional method," *COMBUSTION AND FLAME,* vol. 189, pp. 190-206, 2018.
[32] J. Z. Wen, M. Thomson, S. Park, S. Rogak, and M. Lightstone, "Study of soot growth in a plug flow reactor using a moving sectional model," *Proceedings of the Combustion Institute,* vol. 30, pp. 1477-1484, 2005.
[33] C. B. Stipe, B. S. Higgins, D. Lucas, C. P. Koshland, and R. F. Sawyer, "Inverted co-flow diffusion flame for producing soot," *Review of scientific instruments,* vol. 76, p. 023908, 2005.
[34] R. Ghazi, H. Tjong, A. Soewono, S. N. Rogak, and J. S. Olfert, "Mass, mobility, volatility, and morphology of soot particles generated by a McKenna and inverted burner," *Aerosol Science and Technology,* vol. 47, pp. 395-405, 2013.
[35] R. K. Chakrabarty, I. V. Novosselov, N. D. Beres, H. Moosmüller, C. M. Sorensen, and C. B. Stipe, "Trapping and aerogelation of nanoparticles in negative gravity hydrocarbon flames," *Applied Physics Letters,* vol. 104, p. 243103, 2014.
[36] P. Liu, I. J. Arnold, Y. Wang, Y. Yu, J. Fang, P. Biswas*, et al.*, "Synthesis of titanium dioxide aerosol gels in a buoyancy-opposed flame reactor," *Aerosol Science and Technology,* vol. 49, pp. 1232-1241, 2015.
[37] J. Davis, K. Tiwari, and I. Novosselov, "Soot morphology and nanostructure in complex flame flow patterns via secondary particle surface growth," *Fuel,* vol. 245, pp. 447-457, 2019/06/01/ 2019.
[38] S. L. Bragg, "Application of Reaction Rate Theory to Combustion Chamber Analysis Aeronautical Research Council Pub," *London, UK,* 1953.
[39] S. Lyra and R. S. Cant, "Analysis of high pressure premixed flames using Equivalent Reactor Networks for predicting NOx emissions," *Fuel,* vol. 107, pp. 261-268, 5// 2013.
[40] I. V. Novosselov, *Eight-step global kinetic mechanism on methane oxidation with nitric oxide formation for lean-premixed combustion turbines*: Thesis (M.S.M.E.)--University of Washington., 2002.
[41] P. M. Rubins and D. T. Pratt, "Zone Combustion Model Development and Use: Application to Emissions Control," *American Society of Mechanical Engineers, 91-JPGC-FACT-25,* vol. 91-JPGC-FACT-25, 1991.
[42] T. Rutar and P. C. Malte, "NOx Formation in High-Pressure Jet-Stirred Reactors with Significance to Lean-Premixed Combustion Turbines," *ASME Journal of Engineering for Gas Turbines and Power,* vol. 124, pp. 776-783, 2002.
[43] K. B. Fackler, M. Karalus, I. Novosselov, J. Kramlich, P. Malte, and S. Vijlee, "NOx Behavior for Lean-Premixed Combustion of Alternative Gaseous Fuels," *Journal of Engineering for Gas Turbines and Power,* vol. 138, p. 041504, 2016.
[44] V. Fichet, M. Kanniche, P. Plion, and O. Gicquel, "A reactor network model for predicting NOx emissions in gas turbines," *Fuel,* vol. 89, pp. 2202-2210, 9// 2010.

[45] A. Innocenti, A. Andreini, D. Bertini, B. Facchini, and M. Motta, "Turbulent flow-field effects in a hybrid CFD-CRN model for the prediction of NOx and CO emissions in aero-engine combustors," *Fuel,* vol. 215, pp. 853-864, 2018.

[46] I. V. Novosselov and P. C. Malte, "Development and application of an eight-step global mechanism for CFD and CRN simulations of lean-premixed combustors," *Journal of Engineering for Gas Turbines and Power,* vol. 130, p. 021502, 2008.

[47] I. V. Novosselov, P. C. Malte, S. Yuan, R. Srinivasan, and J. C. Y. Lee, "Chemical Reactor Network Application to Emissions Prediction for Industrial DLE Gas Turbine," presented at the ASME Turbo Expo 2006: Power for Land, Sea, and Air, Barcelona, Spain, 2006.

[48] S. Gupta, P. Malte, S. L. Brunton, and I. Novosselov, "Prevention of lean flame blowout using a predictive chemical reactor network control," *Fuel,* vol. 236, pp. 583-588, 2019.

[49] A. Kaluri, P. Malte, and I. Novosselov, "Real-time prediction of lean blowout using chemical reactor network," *Fuel,* vol. 234, pp. 797-808, 2018/12/15/ 2018.

[50] J. Appel, H. Bockhorn, and M. Frenklach, "Kinetic modeling of soot formation with detailed chemistry and physics: laminar premixed flames of C 2 hydrocarbons," *Combustion and Flame,* vol. 121, pp. 122-136, 2000.

[51] A. C. 17.0, "ANSYS Reaction Design: San Diego, 2016."

[52] A. Trubetskaya, A. Brown, G. A. Tompsett, M. T. Timko, J. Kling, M. Broström*, et al.*, "Characterization and reactivity of soot from fast pyrolysis of lignocellulosic compounds and monolignols," *Applied Energy,* vol. 212, pp. 1489-1500, 2018.

[53] A. Liati, P. D. Eggenschwiler, D. Schreiber, V. Zelenay, and M. Ammann, "Variations in diesel soot reactivity along the exhaust after-treatment system, based on the morphology and nanostructure of primary soot particles," *Combustion and flame,* vol. 160, pp. 671-681, 2013.

[54] E. M. Adkins and J. H. Miller, "Extinction measurements for optical band gap determination of soot in a series of nitrogen-diluted ethylene/air non-premixed flames," *Physical Chemistry Chemical Physics,* vol. 17, pp. 2686-2695, 2015.

[55] R. L. Vander Wal and A. J. Tomasek, "Soot nanostructure: dependence upon synthesis conditions," *Combustion and Flame,* vol. 136, pp. 129-140, 2004.

[56] A. Veshkini, S. B. Dworkin, and M. J. Thomson, "Understanding soot particle size evolution in laminar ethylene/air diffusion flames using novel soot coalescence models," *Combustion Theory and Modelling,* vol. 20, pp. 707-734, 2016.

[57] N. Eaves, S. Dworkin, and M. Thomson, "The importance of reversibility in modeling soot nucleation and condensation processes," *Proceedings of the Combustion Institute,* vol. 35, pp. 1787-1794, 2015.

[58] W. Pejpichestakul, A. Frassoldati, A. Parente, and T. Faravelli, "Kinetic modeling of soot formation in premixed burner-stabilized stagnation ethylene flames at heavily sooting condition," *Fuel,* vol. 234, pp. 199-206, 2018.

[59] A. Guilloteau, Y. Bedjanian, M. L. Nguyen, and A. Tomas, "Desorption of polycyclic aromatic hydrocarbons from a soot surface: three-to five-ring PAHs," *The Journal of Physical Chemistry A,* vol. 114, pp. 942-948, 2009.

[60] P. Mitchell and M. Frenklach, "Monte Carlo simulation of soot aggregation with simultaneous surface growth-why primary particles appear spherical," in *Symposium (International) on Combustion*, 1998, pp. 1507-1514.

[61] B. Apicella, A. Ciajolo, A. Tregrossi, J. Abrahamson, R. Vander Wal, and C. Russo, "HRTEM and EELS investigations of flame-formed soot nanostructure," *Fuel,* vol. 225, pp. 218-224, 2018.

[62] J. Soussi, R. Demarco, J. Consalvi, F. Liu, and A. Fuentes, "Influence of soot aging on soot production for laminar propane diffusion flames," *Fuel,* vol. 210, pp. 472-481, 2017.

[63] A. Peters, B. Veronesi, L. Calderón-Garcidueñas, P. Gehr, L. C. Chen, M. Geiser*, et al.*, "Translocation and potential neurological effects of fine and ultrafine particles a critical update," *Particle and fibre toxicology,* vol. 3, p. 13, 2006.

[64] S. Fuzzi, U. Baltensperger, K. Carslaw, S. Decesari, H. Denier Van Der Gon, M. Facchini*, et al.*, "Particulate matter, air quality and climate: lessons learned and future needs," *Atmospheric chemistry and physics,* vol. 15, pp. 8217-8299, 2015.

[65] Y. Jung and C. Bae, "Immaturity of soot particles in exhaust gas for low temperature diesel combustion in a direct injection compression ignition engine," *Fuel,* vol. 161, pp. 312-322, 2015.

[66] K. Yehliu, R. L. Vander Wal, O. Armas, and A. L. Boehman, "Impact of fuel formulation on the nanostructure and reactivity of diesel soot," *Combustion and Flame,* vol. 159, pp. 3597-3606, 2012.

[67] M. Alfè, B. Apicella, R. Barbella, J.-N. Rouzaud, A. Tregrossi, and A. Ciajolo, "Structure–property relationship in nanostructures of young and mature soot in premixed flames," *Proceedings of the Combustion Institute,* vol. 32, pp. 697-704, 2009.

[68] S. E. Stein and A. Fahr, "High-temperature stabilities of hydrocarbons," *The Journal of Physical Chemistry,* vol. 89, pp. 3714-3725, 1985.

[69] M. Commodo, K. Kaiser, G. De Falco, P. Minutolo, F. Schulz, A. D'Anna*, et al.*, "On the early stages of soot formation: Molecular structure elucidation by high-resolution atomic force microscopy," *Combustion and Flame,* vol. 205, pp. 154-164, 2019.

[70] R. A. Dobbins, "Soot inception temperature and the carbonization rate of precursor particles," *Combustion and Flame,* vol. 130, pp. 204-214, 2002.

[71] M. L. Botero, Y. Sheng, J. Akroyd, J. Martin, J. A. Dreyer, W. Yang*, et al.*, "Internal structure of soot particles in a diffusion flame," *Carbon,* vol. 141, pp. 635-642, 2019.

[72] A. Raj, "Structural effects on the growth of large polycyclic aromatic hydrocarbons by C2H2," *Combustion and Flame,* vol. 204, pp. 331-340, 2019.

[73] J. W. Martin, A. Menon, C. T. Lao, J. Akroyd, and M. Kraft, "Dynamic polarity of curved aromatic soot precursors," *Combustion and Flame,* vol. 206, pp. 150-157, 2019.

[74] M. Sirignano, J. Kent, and A. D'Anna, "Modeling formation and oxidation of soot in nonpremixed flames," *Energy & Fuels,* vol. 27, pp. 2303-2315, 2013.

[75] M. Kholghy, M. Saffaripour, C. Yip, and M. J. Thomson, "The evolution of soot morphology in a laminar coflow diffusion flame of a surrogate for Jet A-1," *Combustion and Flame,* vol. 160, pp. 2119-2130, 2013.

[76] P. Reilly, R. Gieray, W. Whitten, and J. Ramsey, "Direct observation of the evolution of the soot carbonization process in an acetylene diffusion flame via real-time aerosol mass spectrometry," *Combustion and flame,* vol. 122, pp. 90-104, 2000.

[77] L. G. Blevins, R. A. Fletcher, B. A. Benner, E. B. Steel, and G. W. Mulholland, "The existence of young soot in the exhaust of inverse diffusion flames," *Proceedings of the Combustion Institute,* vol. 29, pp. 2325-2333, 2002.

[78] P. Toth, D. Jacobsson, M. Ek, and H. Wiinikka, "Real-time, in situ, atomic scale observation of soot oxidation," *Carbon,* vol. 145, pp. 149-160, 2019.

[79] F. Liu, H. Guo, and G. J. Smallwood, "Effects of radiation model on the modeling of a laminar coflow methane/air diffusion flame," *Combustion and Flame,* vol. 138, pp. 136-154, 2004.

[80] M. Smooke, C. McEnally, L. Pfefferle, R. Hall, and M. Colket, "Computational and experimental study of soot formation in a coflow, laminar diffusion flame," *Combustion and Flame,* vol. 117, pp. 117-139, 1999.

[81] A. Sygula and S. Saebø, "π-π Stacking of curved carbon networks: The corannulene dimer," *International Journal of Quantum Chemistry,* vol. 109, pp. 65-72, 2009.

[82] R. L. Vander Wal, V. M. Bryg, and M. D. Hays, "Fingerprinting soot (towards source identification): Physical structure and chemical composition," *Journal of Aerosol Science,* vol. 41, pp. 108-117, 2010.

[83] C. S. Wang, N. C. Bartelt, R. Ragan, and K. Thürmer, "Revealing the molecular structure of soot precursors," *Carbon,* vol. 129, pp. 537-542, 2018.

[84] K. Wan, D. Chen, and H. Wang, "On imaging nascent soot by transmission electron microscopy," *Combustion and Flame,* vol. 198, pp. 260-266, 2018.

[85] L. Pascazio, M. Sirignano, and A. D'Anna, "Simulating the morphology of clusters of polycyclic aromatic hydrocarbons: The influence of the intermolecular potential," *Combustion and Flame,* vol. 185, pp. 53-62, 2017.

[86] C. Russo, B. Apicella, J. Lighty, A. Ciajolo, and A. Tregrossi, "Optical properties of organic carbon and soot produced in an inverse diffusion flame," *Carbon,* vol. 124, pp. 372-379, 2017.

[87] M. Birch and R. Cary, "Elemental carbon-based method for monitoring occupational exposures to particulate diesel exhaust," *Aerosol Science and Technology,* vol. 25, pp. 221-241, 1996.

[88] E. Molnar, "Effects of Temperature and Fuel Dilution on Soot Yields in an Inverted Gravity Flame Reactor," Master of Science in Engineering Master of Science in Engineering, Mechnical Engineering, Univiersity of Washington, Seattle, WA, 2019.

[89] C. Russo, B. Apicella, J. S. Lighty, A. Ciajolo, and A. Tregrossi, "Optical properties of organic carbon and soot produced in an inverse diffusion flame," *Carbon,* vol. 124, pp. 372-379, 2017.

[90] G. M. Mahamuni, Gaurav; Rutherford, Jay; Davis, Justin; Molnar, Eric; Posner, Jonathan D.; Seto, Edmund, "Excitation-Emission Matrix Spectroscopy for Analysis of Chemical Composition of Combustion Generated Particulate Matter," *ChemRxiv,* 2019.

[91] B. Apicella, P. Pré, J. Rouzaud, J. Abrahamson, R. Vander Wal, A. Ciajolo*, et al.*, "Laser-induced structural modifications of differently aged soot investigated by HRTEM," *Combustion and Flame,* vol. 204, pp. 13-22, 2019.

[92] H. Ghiassi, P. Toth, I. C. Jaramillo, and J. S. Lighty, "Soot oxidation-induced fragmentation: Part 1: The relationship between soot nanostructure and oxidation-induced fragmentation," *Combustion and Flame,* vol. 163, pp. 179-187, 2016.

[93] I. C. Jaramillo, C. K. Gaddam, R. L. Vander Wal, and J. S. Lighty, "Effect of nanostructure, oxidative pressure and extent of oxidation on model carbon reactivity," *Combustion and Flame,* vol. 162, pp. 1848-1856, 2015.

[94] M. L. Botero, N. Eaves, J. A. H. Dreyer, Y. Sheng, J. Akroyd, W. Yang*, et al.*, "Experimental and numerical study of the evolution of soot primary particles in a diffusion flame," *Proceedings of the Combustion Institute,* vol. 37, pp. 2047-2055, 2019.

[95] J. D. Herdman, B. C. Connelly, M. D. Smooke, M. B. Long, and J. H. Miller, "A comparison of Raman signatures and laser-induced incandescence with direct numerical simulation of soot growth in non-premixed ethylene/air flames," *Carbon,* vol. 49, pp. 5298-5311, 2011.

[96] M. Alfè, B. Apicella, J.-N. Rouzaud, A. Tregrossi, and A. Ciajolo, "The effect of temperature on soot properties in premixed methane flames," *Combustion and Flame,* vol. 157, pp. 1959-1965, 2010.

[97] P. Toth, A. B. Palotas, E. G. Eddings, R. T. Whitaker, and J. S. Lighty, "A novel framework for the quantitative analysis of high resolution transmission electron micrographs of soot I. Improved measurement of interlayer spacing," *Combustion and Flame,* vol. 160, pp. 909-919, 2013.

[98] A. Ferrari and J. Robertson, "Resonant Raman spectroscopy of disordered, amorphous, and diamondlike carbon," *Physical Review B,* vol. 64, p. 075414, 2001.

[99] D. Chen and H. Wang, "HOMO-LUMO energy splitting in polycyclic aromatic hydrocarbons and their derivatives," *Proceedings of the Combustion Institute,* vol. 37, pp. 953-959, 2019.

[100] J. W. Martin, K. Bowal, A. Menon, R. I. Slavchov, J. Akroyd, S. Mosbach*, et al.*, "Polar curved polycyclic aromatic hydrocarbons in soot formation," *Proceedings of the Combustion Institute,* vol. 37, pp. 1117-1123, 2019.

[101] A. Sadezky, H. Muckenhuber, H. Grothe, R. Niessner, and U. Pöschl, "Raman microspectroscopy of soot and related carbonaceous materials: spectral analysis and structural information," *Carbon,* vol. 43, pp. 1731-1742, 2005.

[102] K. M. Updyke, T. B. Nguyen, and S. A. Nizkorodov, "Formation of brown carbon via reactions of ammonia with secondary organic aerosols from biogenic and anthropogenic precursors," *Atmospheric environment,* vol. 63, pp. 22-31, 2012.

[103] P. Lin, L. T. Fleming, S. A. Nizkorodov, J. Laskin, and A. Laskin, "Comprehensive Molecular Characterization of Atmospheric Brown Carbon by High Resolution Mass Spectrometry with Electrospray and Atmospheric Pressure Photoionization," *Analytical Chemistry,* vol. 90, pp. 12493-12502, Nov 2018.

[104] H. Sun, L. Biedermann, and T. C. Bond, "Color of brown carbon: A model for ultraviolet and visible light absorption by organic carbon aerosol," *Geophysical Research Letters,* vol. 34, pp. n/a-n/a, 2007.

[105] Y. Cheng, K.-B. He, G. Engling, R. Weber, J.-M. Liu, Z.-Y. Du*, et al.*, "Brown and black carbon in Beijing aerosol: Implications for the effects of brown coating on light absorption by black carbon," *Science of the Total Environment,* vol. 599-600, pp. 1047-1055, 2017.

[106] S. M. Phillips and G. D. Smith, "Spectroscopic comparison of water- and methanol-soluble brown carbon particulate matter," *Aerosol Science and Technology,* vol. 51, pp. 1113-1121, 2017.

[107] M. Jacobson, "Isolating nitrated and aromatic aerosols and nitrated aromatic gases as sources of ultraviolet light absorption," *Journal of Geophysical Research: Atmospheres,* vol. 104, pp. 3527-3542, 1999.

[108] Y. Chen and T. C. Bond, "Light absorption by organic carbon from wood combustion," *Atmospheric Chemistry and Physics,* vol. 10, pp. 1773-1787, 2010.

[109] A. Hecobian, X. Zhang, M. Zheng, N. Frank, E. S. Edgerton, and R. J. Weber, "Water-Soluble Organic Aerosol material and the light-absorption characteristics of aqueous extracts measured over the Southeastern United States," *Atmospheric Chemistry and Physics,* vol. 10, pp. 5965-5977, 2010.

[110] A. V. Sosa, "Association of the Type of Toy Used During Play With the Quantity and Quality of Parent-Infant Communication," *JAMA Pediatrics,* vol. 170, pp. 132-137, 2016.

[111] N. Li, M. I. Venkatesan, A. Miguel, R. Kaplan, C. Gujuluva, J. Alam*, et al.*, "Induction of heme oxygenase-1 expression in macrophages by diesel exhaust particle chemicals and quinones via the antioxidant-responsive element," *Journal of immunology (Baltimore, Md. : 1950),* vol. 165, p. 3393, 2000.

[112] N. Li, C. Sioutas, A. Cho, D. Schmitz, C. Misra, J. Sempf*, et al.*, "Ultrafine particulate pollutants induce oxidative stress and mitochondrial damage," *Environmental health perspectives,* vol. 111, pp. 455-460, 2003.

[113] G. Mahamuni, J. Rutherford, J. Davis, E. Molnar, J. D. Posner, and E. Seto, "Excitation-Emission Matrix Spectroscopy for Analysis of Chemical Composition of Combustion Generated Particulate Matter," *ChemRxiv,* 2019.

[114] I. C. T. Nisbet and P. K. Lagoy, "Toxic equivalency factors (TEFs) for polycyclic aromatic hydrocarbons (PAHs)," *Regulatory Toxicology and Pharmacology,* vol. 16, pp. 290-300, 1992.

[115] M. F. Karalus, K. B. Fackler, I. V. Novosselov, J. C. Kramlich, and P. C. Malte, "Characterizing the mechanism of lean blowout for a recirculation-stablized premixed hydrogen flame," presented at the Turbine Technical Conference and Exposition, Copenhagen, Denmark, 2012.

[116] Y. Guan, R. S. Vaddi, A. Aliseda, and I. Novosselov, "Experimental and numerical investigation of electrohydrodynamic flow in a point-to-ring corona discharge," *Physical Review Fluids,* vol. 3, p. 043701, 04/20/ 2018.

[117] G. Kalitzin, G. Medic, G. Laccarino, and P. Durbin, "Near-wall behavior of RANS turbulence models and implications for wall functions," *Journal of Computational Physics,* vol. 204, pp. 265-291, 2005.

[118] K. B. Fackler, M. F. Karalus, I. V. Novosselov, J. C. Kramlich, P. C. Malte, and S. Vijlee, "NOx behavior for lean-premixed combustion of alternative gaseous fuels," *Journal of Engineering for Gas Turbines and Power,* vol. 138, p. 041504, 2016.

[119] M. M. CONSTANTINE and A. D. Richard, "Comparison of soot growth and oxidation in smoking and non–smoking ethylene diffusion flames," *Combustion Science and Technology,* vol. 66, pp. 1-16, 1989.

[120] P. Akridis and S. Rigopoulos, "Modelling of soot formation in laminar diffusion flames using a comprehensive CFD-PBE model with detailed gas-phase chemistry," *Combustion Theory and Modelling,* vol. 21, pp. 35-48, 2017.

VITA

Justin Davis is from Sherwood Oregon where he grew up with parents John and Cindy Davis. He attended Linfield College in McMinnville, Oregon where he graduated with a double major in Math and Physics. During his time at Linfield, he conducted two years of research under the direction of Dr. Jennifer Heath. The project looked at characterizing thin film solar cells and provided a great introduction to working in a lab. He also played baseball at Linfield, lettering twice.

After graduation, Justin enrolled in the second cohort of the Molecular Engineering Ph.D. program at the University of Washington. He immediately started working in Dr. Igor Novosselov's lab. During his time at UW, his research consisted of two main projects (i) exploring the formation of combustion generated particles from first principles and (ii) designing and fabricating a supercritical CO_2 reactor to process thermally labile compounds.